Exhibit A

Publications

Exhibit Number	Bibliography
Exhibit A-1	**L. Le Guehennec et. al. Surface Treatments of Titanium Dental Implants for Rapid Osseointegration. Dental Materials 2007 23(7): 844-854.**
Exhibit A-2	**Sergey V. Dorozhkin and Matthias Epple. Biological and Medical Significance of Calcium Phosphates. Angewandte Chemie International Edition. 2002 41(17): 3130-3146.**
Exhibit A-3	**Chung-Wei Yang and Truan-Sheng Lui. Biological and Biomedical Coatings Handbook: Processing and Characterization. Chapter 6: Hydrothermal Crystallization with Microstructural Self-Healing Effect on Mechanical and Failure Behaviors of Plasma-Sprayed Hydroxyapatite Coatings. 2011: 240-253.**
Exhibit A-4	**Wang Yongsheng. Biological and Biomedical Coatings Handbook: Applications. Chapter 1: Sol-Gel Derived Hydroxyapatite Coatings on Metallic Implants: Characterization, In Vitro and In Vivo Analysis. 2017: 1-33.**
Exhibit A-5	**Carine Viornery et. al. Surface Modification of Titanium with Phosphonic Acid To Improve Bone Bonding: Characterization by XPS and ToF-SIMS. Langmuir. 2002 18(7): 2582-2589.**
Exhibit A-6	**NBMolecules®. Determination of SurfLink® Surface Treatment Thickness on Sterile SurfLink® Dental Implants by X-ray Photoelectron Spectroscopy (XPS). 2012.**
Exhibit A-7	**NBMolecules®. Optimization of the Surflink® Surface Treatment Process for MIS Implants. 2015.**

Exhibit A-1

L. Le Guehennec et. al. Surface Treatments of Titanium Dental Implants for Rapid Osseointegration. Dental Materials 2007 23(7): 844-854.

DENTAL MATERIALS 23 (2007) 844–854

available at www.sciencedirect.com

ScienceDirect

journal homepage: www.intl.elsevierhealth.com/journals/dema

Review

Surface treatments of titanium dental implants for rapid osseointegration

L. Le Guéhennec, A. Soueidan, P. Layrolle, Y. Amouriq*

Inserm U791, LIOAD, Osteoarticular and Dental Tissue Engineering, Faculty of Dental Surgery, 1 Place Alexis Ricordeau, 44042 Nantes cedex 1, France

ARTICLE INFO

Article history:
Received 9 November 2005
Received in revised form 9 June 2006
Accepted 20 June 2006

Keywords:
Osseointegration
Dental implants
Surface roughness
Nano-sized topography
Biomimetic calcium phosphate coating

ABSTRACT

The osseointegration rate of titanium dental implants is related to their composition and surface roughness. Rough-surfaced implants favor both bone anchoring and biomechanical stability. Osteoconductive calcium phosphate coatings promote bone healing and apposition, leading to the rapid biological fixation of implants. The different methods used for increasing surface roughness or applying osteoconductive coatings to titanium dental implants are reviewed. Surface treatments, such as titanium plasma-spraying, grit-blasting, acid-etching, anodization or calcium phosphate coatings, and their corresponding surface morphologies and properties are described. Most of these surfaces are commercially available and have proven clinical efficacy (>95% over 5 years). The precise role of surface chemistry and topography on the early events in dental implant osseointegration remain poorly understood. In addition, comparative clinical studies with different implant surfaces are rarely performed. The future of dental implantology should aim to develop surfaces with controlled and standardized topography or chemistry. This approach will be the only way to understand the interactions between proteins, cells and tissues, and implant surfaces. The local release of bone stimulating or resorptive drugs in the peri-implant region may also respond to difficult clinical situations with poor bone quality and quantity. These therapeutic strategies should ultimately enhance the osseointegration process of dental implants for their immediate loading and long-term success.

Contents

* *Corresponding author*. Tel.: +33 2 4041 2916; fax: +33 2 40 08 37 12.
E-mail address: pierre.layrolle@nantes.inserm.fr (P. Layrolle).

0109-5641/$ – see front matter © 2006 Academy of Dental Materials. Published by Elsevier Ltd. All rights reserved.
doi:10.1016/j.dental.2006.06.025

1. Introduction

In the past 20 years, the number of dental implant procedures has increased steadily worldwide, reaching about one million dental implantations per year. The clinical success of oral implants is related to their early osseointegration. Geometry and surface topography are crucial for the short- and long-term success of dental implants. These parameters are associated with delicate surgical techniques, a prerequisite for a successful early clinical outcome [1]. After implantation, titanium implants interact with biological fluids and tissues. Direct bone apposition onto the surface of the titanium is critical for the rapid loading of dental implants. After the initial stages of osseointegration, both prosthetic biomechanical factors and patient hygiene are crucial for the long-term success of the implants. There are two types of response after implantation. The first type involves the formation of a fibrous soft tissue capsule around the implant. This fibrous tissue capsule does not ensure proper biomechanical fixation and leads to clinical failure of the dental implant. The second type of bone response is related to direct bone–implant contact without an intervening connective tissue layer. This is what is known as osseointegration. This biological fixation is considered to be a prerequisite for implant-supported prostheses and their long-term success. The rate and quality of osseointegration in titanium implants are related to their surface properties. Surface composition, hydrophilicity and roughness are parameters that may play a role in implant–tissue interaction and osseointegration.

This review focuses on the different surfaces and methods that aim to accelerate the osseointegration of dental implants. The physical and chemical properties of implant surfaces are discussed in relation to their biological and clinical behavior. Manufacturers of dental implants have developed a variety of surfaces with different compositions and degrees of roughness. However, there is controversy as to the optimal features for implant surfaces regarding osseointegration kinetics.

2. Chemical composition of the surface of dental implants

The chemical composition or charges on the surface of titanium implants differ, depending on their bulk composition and surface treatments. The composition and charges are critical for protein adsorption and cell attachment. Dental implants are usually made from commercially pure titanium or titanium alloys. Commercially pure titanium (cpTi) has various degrees of purity (graded from 1 to 4). This purity is characterized by oxygen, carbon and iron content. Most dental implants are made from grade 4 cpTi as it is stronger than other grades. Titanium alloys are mainly composed of Ti6Al4V (grade 5 titanium alloy) with greater yield strength and fatigue properties than pure titanium [2].

The surface chemical composition of titanium implants also affects the hydrophilicity of the surface. Highly hydrophilic surfaces seem more desirable than hydrophobic ones in view of their interactions with biological fluids, cells and tissues [3,4]. Contact angle measurements give values ranging from 0° (hydrophilic) to 140° (hydrophobic) for titanium implant surfaces [3,5,6]. In a recent animal study, Buser et al. [3] found that a hydrophilic SLA surface gave higher bone-to-implant contact than regular SLA. Nevertheless, previous in vivo studies performed by Albrektsson and co-workers [7,8] failed to demonstrate higher osseointegration using hydrophilic surfaced dental implants.

3. Surface roughness of dental implants

There are numerous reports that demonstrate that the surface roughness of titanium implants affects the rate of osseointegration and biomechanical fixation [9,10]. Surface roughness can be divided into three levels depending on the scale of the features: macro-, micro- and nano-sized topologies.

The macro level is defined for topographical features as being in the range of millimetres to tens of microns. This scale is directly related to implant geometry, with threaded screw and macroporous surface treatments giving surface roughness of more than 10 μm. Numerous reports have shown that both the early fixation and long-term mechanical stability of the prosthesis can be improved by a high roughness profile compared to smooth surfaces [11–13]. The high roughness resulted in mechanical interlocking between the implant surface and bone ongrowth. However, a major risk with high surface roughness may be an increase in peri-implantitis as well as an increase in ionic leakage [14]. A moderate roughness of 1–2 μm may limit these two parameters [15].

The microtopographic profile of dental implants is defined for surface roughness as being in the range of 1–10 μm. This range of roughness maximizes the interlocking between mineralized bone and the surface of the implant [10,13]. A theoretical approach suggested that the ideal surface should be covered with hemispherical pits approximately 1.5 μm in depth and 4 μm in diameter [16].

The main clinical indication for using an implant with a rough surface is the poor quality or volume of the host bone. In these unfavorable clinical situations, early and high

Table 1 – Surface properties of titanium dental implants

Type of implant	Surface roughness (μm)	Contact angle (°)	References
cpTi	Ra = 0.22 ± 0.01[a]	55.4 ± 4.1	[5,107]
Ti6Al4V	Ra = 0.23 ± 0.01[a]	56.3 ± 2.7	[5,107]
TPS	Ra = 7.01 ± 2.09	n.d.	[5]
SLA	Sa = 1.15 ± 0.05	138.3 ± 4.2	[3]
Modified SLA	Sa = 1.16 ± 0.04	0	[3]
Plasma-sprayed HA coating	Ra = 1.06 ± 0.21	57.4 ± 3.2	[6,108]
Biomimetic CaP coating	Ra = 1.83 ± 0.64	13.4 ± 0.17	This work

[a] Machined and polished surfaces.

bone-to-implant contact would be beneficial for allowing high levels of loading. In the cases of insufficient bone quantity or anatomical limitations, short designed implants with a rough surface have demonstrated superior clinical outcomes than smooth surfaces [17,18]. Numerous studies have shown that surface roughness in this range resulted in greater bone-to-implant contact and higher resistance to torque removal than other types of surface topography [10,13]. These reports have demonstrated that titanium implants with roughened surfaces have greater contact with bone than titanium implants with smoother surfaces [9,10]. However, the Cochrane collaboration has not found any clinical evidence demonstrating the superiority of any particular implant surface [19].

Surface profiles in the nanometer range play an important role in the adsorption of proteins, adhesion of osteoblastic cells and thus the rate of osseointegration [20]. However, reproducible surface roughness in the nanometer range is difficult to produce with chemical treatments. In addition, the optimal surface nano topography for selective adsorption of proteins leading to the adhesion of osteoblastic cells and rapid bone apposition is unknown.

Various methods have been developed in order to create a rough surface and improve the osseointegration of titanium dental implants (Table 1). These methods use titanium plasma-spraying, blasting with ceramic particles, acid-etching and anodization.

3.1. *Roughening of implants by titanium plasma-spraying*

A titanium plasma-spraying (TPS) method has been used for producing rough implant surfaces (Fig. 1). This method consists in injecting titanium powders into a plasma torch at high temperature. The titanium particles are projected on to the surface of the implants where they condense and fuse together, forming a film about 30 μm thick. The thickness must reach 40–50 μm to be uniform. The resulting TPS coating has an average roughness of around 7 μm, which increases the surface area of the implant. It has been shown that this three-dimensional topography increased the tensile strength at the bone/implant interface [11]. In this pre-clinical study using minipigs, the bone/implant interface formed faster with a TPS surface than with smooth surface implants presenting an average roughness of 0.2 μm. However, particles of titanium have sometimes been found in the bone adjacent to these implants [21]. The presence of metallic wear particles from endosseous implants in the liver, spleen, small aggregates of macrophages and even in the para-aortic lymph nodes have also been reported [21]. Metal ions released from implants may be the product of dissolution, fretting and wear, and may be a source of concern due to their potentially harmful local and systemic carcinogenic effects [22,23]. However, the local and systemic adverse effects of the release of titanium ions have not been universally recognized. In a clinical study comparing SLA and TPS implant surfaces, no clinical difference was observed between these two surfaces [24]. In a pre-clinical model, the percentage of bone/implant contact was found to be inferior for the TPS surface than for plasma-sprayed hydroxyapatite-coated implants [25]. Nowadays, there is a consensus on the clinical advantages of implanting moderately rough surfaced implants (in the micrometric range) rather than using rough plasma-sprayed implant surfaces [11,26].

3.2. *Roughening of implants by grit-blasting*

Another approach for roughening the titanium surface consists in blasting the implants with hard ceramic particles. The

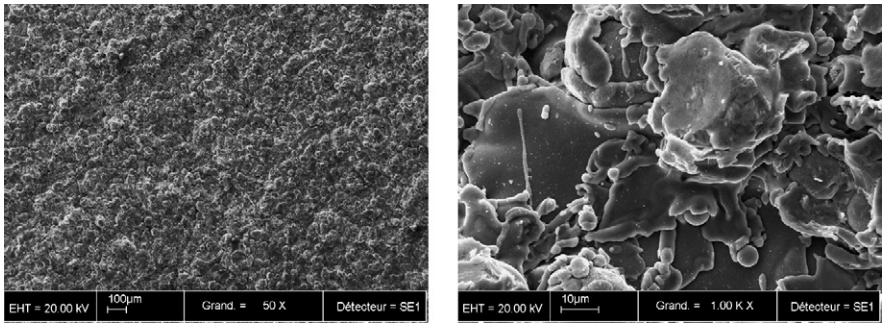

Fig. 1 – SEM micrographs of a titanium plasma-sprayed (TPS) surface (Courtesy of Cam Implants BV, The Netherlands).

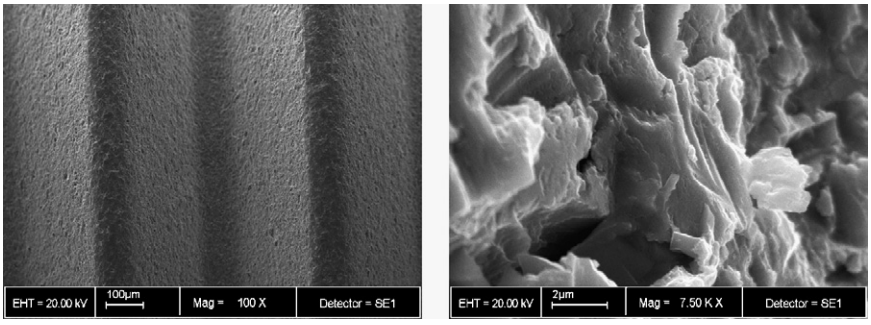

Fig. 2 – SEM micrographs of a TiO blasted surface (Courtesy of Astratech TiOblast^{TM}, France).

ceramic particles are projected through a nozzle at high velocity by means of compressed air. Depending on the size of the ceramic particles, different surface roughnesses can be produced on titanium implants. The blasting material should be chemically stable, biocompatible and should not hamper the osseointegration of the titanium implants. Various ceramic particles have been used, such as alumina, titanium oxide and calcium phosphate particles.

Alumina (Al_2O_3) is frequently used as a blasting material and produces surface roughness varying with the granulometry of the blasting media. However, the blasting material is often embedded into the implant surface and residue remains even after ultrasonic cleaning, acid passivation and sterilization. Alumina is insoluble in acid and is thus hard to remove from the titanium surface. In some cases, these particles have been released into the surrounding tissues and have interfered with the osseointegration of the implants. Moreover, this chemical heterogeneity of the implant surface may decrease the excellent corrosion resistance of titanium in a physiological environment [27].

Titanium oxide is also used for blasting titanium dental implants. Titanium oxide particles with an average size of 25 μm produce a moderately rough surface in the 1–2 μm range on dental implants. An example of a titanium oxide-blasted surface is shown in Fig. 2. An experimental study using microimplants in humans has shown a significant improvement for bone-to-implant contact (BIC) for the TiO_2 blasted implants in comparison with machined surfaces [28]. Other experimental studies confirmed the increase in BIC for titanium grit-blasted surfaces [12,29]. Other studies have reported high clinical success rates for titanium grit-blasted implants, up to 10 years after implantation [30,31]. Comparative clinical studies gave higher marginal bone levels and survival rates for TiO_2 grit-blasted implants than for machined turned implants [32,33].

Wennerberg et al. [13] demonstrated with a rabbit model that grit-blasting with TiO_2 or Al_2O_3 particles gave similar values of bone–implant contact, but drastically increased the biomechanical fixation of the implants when compared to smooth titanium. These studies have shown that the torque force increased with the surface roughness of the implants while comparable values in bone apposition were observed [34]. These studies corroborate that roughening titanium dental implants increases their mechanical fixation to bone but not their biological fixation.

A third possibility for roughening titanium dental implants consists in using a biocompatible, osteoconductive and resorbable blasting material. Calcium phosphates such as hydroxyapatite, beta-tricalcium phosphate and mixtures have been considered useful blasting materials. These materials are resorbable, leading to a clean, textured, pure titanium surface. Experimental studies have demonstrated a higher bone-to-implant contact with these surfaces when compared to machined surfaces [35,36]. Experimental studies have demonstrated a bone-to-implant contact similar to that observed with other blasting surfaces when osseointegration is achieved [37].

3.3. *Roughening of implants by acid-etching*

Etching with strong acids such as HCl, H_2SO_4, HNO_3 and HF is another method for roughening titanium dental implants. Acid-etching produces micro pits on titanium surfaces with sizes ranging from 0.5 to 2 μm in diameter [38,39]. Acid-

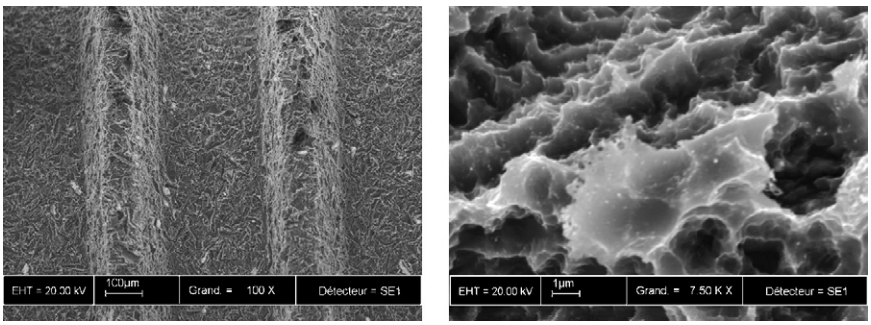

Fig. 3 – SEM micrographs of an SLA surface on a titanium dental implant (Courtesy of Straumann AG, Switzerland).

etching has been shown to greatly enhance osseointegration [40]. Immersion of titanium implants for several minutes in a mixture of concentrated HCl and H_2SO_4 heated above 100 °C (dual acid-etching) is employed to produce a microrough surface (Fig. 3). This type of surface promotes rapid osseointegration while maintaining long-term success over 3 years [41]. It has been found that dual acid-etched surfaces enhance the osteoconductive process through the attachment of fibrin and osteogenic cells, resulting in bone formation directly on the surface of the implant [42]. In the peri-implant area, woven bone with thin trabeculae projecting into the implants, has been described [43]. These studies hypothesized that implants treated by dual acid-etching have a specific topography able to attach to the fibrin scaffold, to promote the adhesion of osteogenic cells, and thus to promote bone apposition [44,45]. Several experimental studies have reported higher bone-to-implant contact and less bone resorption with dual acid-etched surfaces compared to machined or TPS surfaces [9,46,47]. Recently, acid-etching methods have been improved in order to increase cell adhesion and bone neoformation. High temperature acid-etching produces a homogeneous microporous surface with higher bone-to-implant contact than TPS surfaces in experimental studies [48,49]. The wettability of the surface has also been proposed to promote fibrin adhesion. This fibrin adhesion provides contact guidance for the osteoblasts migrating along the surface. An experimental study has demonstrated that a hydrophilic surface greatly improved the bone/implant contact compared to standard sand-blasted and acid-etched implants in minipigs [3].

Another approach involves treating titanium dental implants in fluoride solutions. Titanium is very reactive to fluoride ions, forming soluble TiF_4 species. The surface produced has a microrough topography as shown in Fig. 4. This chemical treatment of the titanium created both a surface roughness and fluoride incorporation favorable to the osseointegration of dental implants [50,51]. It has been shown that this chemical surface treatment enhanced osteoblastic differentiation in comparison with control samples [52]. Fluoridated rough implants also withstood greater push-out forces and showed a significantly higher torque removal than the control implants [50,51]. This chemical treatment may have the potential to further improve implant anchorage in bone by rendering the implant surface bioactive.

Nevertheless, chemical treatments might reduce the mechanical properties of titanium. For instance, acid-etching can lead to hydrogen embrittlement of the titanium, creating micro cracks on its surface that could reduce the fatigue resistance of the implants [53]. Indeed, experimental studies have reported the absorption of hydrogen by titanium in a biological environment. This hydrogen embrittlement of titanium is also associated with the formation of a brittle hybrid phase, leading to a reduction in the ductility of the titanium. This phenomenon is related to the occurrence of fracture mechanisms in dental implants [53].

3.4. *Roughening of implants by anodization*

Micro- or nano-porous surfaces may also be produced by potentiostatic or galvanostatic anodization of titanium in strong acids (H_2SO_4, H_3PO_4, HNO_3, HF) at high current density (200 A/m^2) or potential (100 V). The result of the anodization is to thicken the oxide layer to more than 1000 nm on titanium. When strong acids are used in an electrolyte solution, the oxide layer will be dissolved along current convection lines and thickened in other regions. The dissolution of the oxide layer along the current convection lines creates micro- or nano-pores on the titanium surface [54–57]. Anodization produces modifications in the microstructure and the crystallinity of the titanium oxide layer [58]. The anodization process is rather complex and depends on various parameters such as current density, concentration of acids, composition and electrolyte temperature.

Anodized surfaces result in a strong reinforcement of the bone response with higher values for biomechanical and histomorphometric tests in comparison to machined surfaces [59,60]. A higher clinical success rate was observed for the anodized titanium implants in comparison with turned titanium surfaces of similar shapes [61]. Two mechanisms have been proposed to explain this osseointegration: mechanical interlocking through bone growth in pores, and biochemical bonding [55,62]. Modifications to the chemical composition of the titanium oxide layer have been tested with the incorporation of magnesium, calcium, sulfur or phosphorus [63,64]. It has been found that incorporating magnesium into the titanium oxide layer leads to a higher removal torque value compared to other ions [55].

In summary, surface roughness plays a major role in both the quality and rate of osseointegration of titanium dental

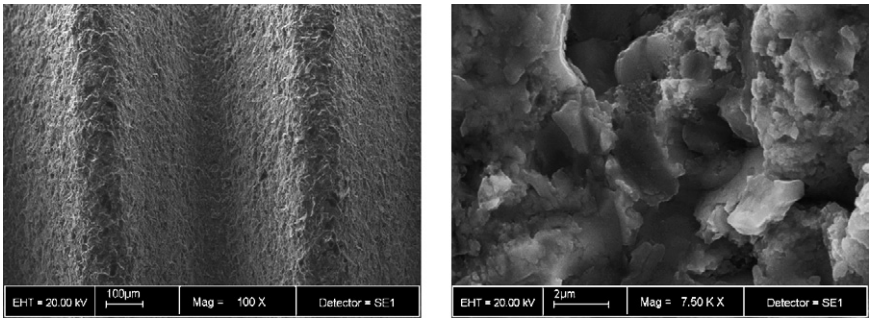

Fig. 4 – SEM micrographs of treatment of titanium dental implants in a fluoride solution surface (Courtesy of Astratech OsseoSpeed™, France).

implants. Highly roughened implants such as TPS or grit-blasted have been shown to favor mechanical anchorage and primary fixation to bone. Topographies in the nanometer range have been used to promote protein adsorption, osteoblastic cell adhesion and the rate of bone tissue healing in the peri-implant region.

4. Osteoconductive calcium phosphate coatings on dental implants

Metal implants have been coated with layers of calcium phosphates mainly composed of hydroxyapatite. Following implantation, the release of calcium phosphate into the peri-implant region increases the saturation of body fluids and precipitates a biological apatite onto the surface of the implant [65,66]. This layer of biological apatite might contain endogenous proteins and serve as a matrix for osteogenic cell attachment and growth [67]. The bone healing process around the implant is therefore enhanced by this biological apatite layer. The biological fixation of titanium implants to bone tissue is faster with a calcium phosphate coating than without [68,69]. It is well-recognized that calcium phosphate coatings have led to better clinical success rates in the long-term than uncoated titanium implants [68,70]. These long-term success rates are due to a superior initial rate of osseointegration [70]. Different methods have been developed to coat metal implants: plasma-spraying, sputter-deposition, sol–gel coating, electrophoretic deposition or biomimetic precipitation. However, only the plasma-spraying coating method has been used for titanium dental implants in clinical practice.

Plasma-spraying is a technique in which hydroxyapatite (HA) ceramic particles are injected into a plasma torch at high temperature and projected on to the surface of the titanium where they condense and fuse together, forming a film (Fig. 5). Plasma-sprayed coatings can be deposited with a thickness ranging from a few micrometers to a few millimeters. In order to obtain mechanical retention of the coating, the surface of the metallic implant must be roughened, e.g. by means of grit-blasting, when using this method.

The plasma-spraying method has disadvantages, however, such as the porosity of the coating and residual stress at the substrate/coating interface, as well as drastic changes in the composition and crystallinity of the initial calcium phosphate powder [71,72]. Several calcium phosphate phases have been observed in plasma-sprayed HA coatings such as tricalcium phosphates (β- and α-TCP), tetracalcium phosphate, calcium oxide and amorphous calcium phosphate (ACP) [73–75]. Plasma-sprayed HA coatings are usually composed of large crystalline HA particles embedded into a highly soluble amorphous calcium phosphate phase. Moreover, the plasma-spraying technique is not very effective for coating tiny dental implants with a complex shape.

Plasma-sprayed HA-coated dental implants have also been associated with clinical problems [6,76–79]. One of the major concerns with plasma-sprayed coatings is the possible delamination of the coating from the surface of the titanium implant and failure at the implant-coating interface despite the fact that the coating is well-attached to the bone tissue. The discrepancy in dissolution between the various phases that make up the coating has led to delamination, particle release and thus the clinical failure of implants [76–79]. Coating delamination has been reported in dental situations where the efficacy of plasma-spraying is not optimal due to the size of the dental implants [6]. Loosening of the coating has also been reported, especially when the implants have been inserted into dense bone.

For all of the above reasons, the clinical use of plasma-sprayed HA-coated dental implants is limited. Plasma-sprayed HA-coated prostheses are nevertheless highly successful in orthopedics. Despite their negative reputation in dental practice, a meta-analytic review did not show that long-term survival rates were inferior for plasma-sprayed HA-coated dental implants compared to other types of dental implant [78].

5. Future trends in dental implant surfaces

A few strategies should be considered in order to improve both the short and long-term osseointegration of titanium dental implants. These future trends concern the modifications of surface roughness at the nanoscale level for promoting protein adsorption and cell adhesion, biomimetic calcium phosphate coatings for enhancing osteoconduction and the incorporation of biological drugs for accelerating the bone healing process in the peri-implant area.

5.1. *Surface roughness at the nanoscale level*

The chemistry and roughness of implant surfaces play a major role in the biological events that follow implantation. Nevertheless, surfaces are often developed using an empirical

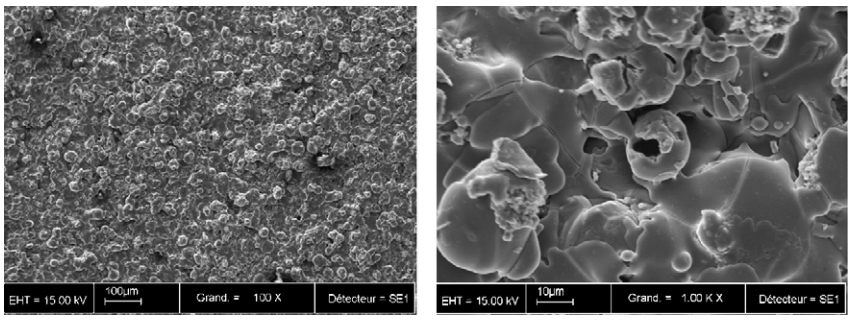

Fig. 5 – SEM micrographs of a plasma-sprayed hydroxyapatite (HA) coating surface (Courtesy of Cam Implants BV, The Netherlands).

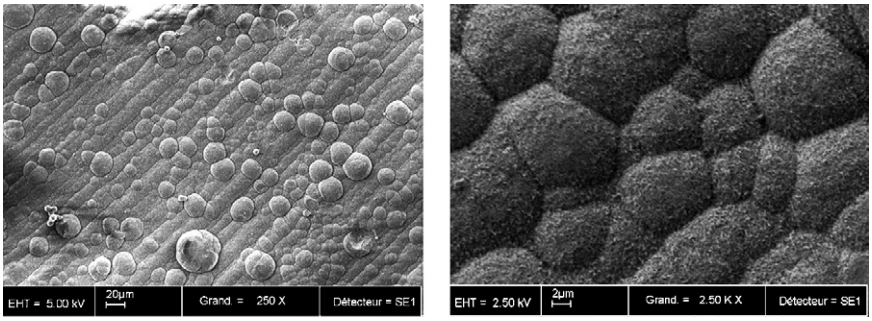

Fig. 6 – SEM micrographs of a biomimetic calcium phosphate coating.

approach with in vitro and in vivo tests. Most of the surfaces currently available have random topography with a wide range of thicknesses, from nanometers to millimeters. The exact biological role of these features is unknown because of the absence of standardized surfaces with repetitive topography at the nano-sized level (e.g. pits with fixed diameters and depth, lanes with controlled profiles). Such controlled or standardized surfaces might help to understand the interactions between specific proteins and cells. These standardized surfaces might also promote early bone apposition on the implants.

Only a few studies have reported modifications to the roughness as well as the chemistry at the nanometer scale in a reproducible manner. Most of these attempts have used processing methods from the electronic industry such as lithography and surface laser-pitting. In vitro experimental studies [80–82] have demonstrated that the attachment of osteoblastic cells was enhanced on submicron scale structures but not on smooth surfaces. Well-developed filopodia directly entered nanometer-sized pores for the initial attachment of the osteoblastic cells. These nanometer structures may also give the cells positive guidance by means of the selective attachment of osteoblasts to the implant surface. This selective attachment process might result in the improvement of initial healing around dental implants.

5.2. *Biomimetic calcium phosphate coatings on titanium dental implants*

In order to avoid the drawbacks of plasma-sprayed HA coatings (see Section 4), scientists have developed a new coating method inspired by the natural process of biomineralization. In this biomimetic method, the precipitation of calcium phosphate apatite crystals onto the titanium surface from simulated body fluids (SBF) formed a coating at room temperature (Fig. 6). In order to accelerate the deposition of coatings from aqueous solutions, several methods have been developed.

The first method involves the electrodeposition of calcium phosphate by using a current, a titanium cathode and a platinum anode [83,84]. This electrochemical method is usually conducted in acidic calcium phosphate solutions and leads to the formation of brushite coatings which are subsequently converted into apatite by hydrothermal processing. The electrochemical deposition performed in simulated body fluid buffered at neutral pH can produce a carbonated apatite coating directly on the titanium surfaces [85]. This method makes possible perfect control of the thickness of the deposit on all kinds of complicated surfaces. The time required for coating is very short and the process presents high reproducibility and efficacy [86,87].

The second method is based on the biomimetic precipitation of calcium phosphate on titanium surfaces by immersion in SBF. This method involves the heterogeneous nucleation and growth of bone-like crystals on the surface of the implant at physiological temperatures and under pH conditions. In general, two subsequent steps have been used to enhance the heterogeneous nucleation of the Ca–P. First, the implants are treated with an alkaline in order to form titanium hydroxyl groups on the titanium surface, to serve as nucleating points [88]. Others have used high concentrations of calcium and phosphate in an increasing pH solution to form a thin layer on the titanium surface. In the second step, the coating develops under crystal growth conditions [89]. The heterogeneous nucleation and growth of the Ca–P on the titanium surface is initiated by the chemical bonding of nano-sized clusters, forming an interfacial unstructured matrix, stabilized by the presence of magnesium ions [90]. The mechanical stability of the Ca–P coating requires a rough titanium surface to ensure the mechanical stability of the coating. In addition, this physiological method broadens the variety of calcium phosphate phases that can be deposited, such as octacalcium phosphate or bone-like carbonate apatite [88,91]. It has been shown that such biomimetic coatings are more soluble in physiological fluids and resorbable by osteoclastic cells like dentin materials than high temperature coatings such as plasma-sprayed HA [91,92]. The osseointegration of titanium implants coated with biomimetic calcium phosphate has been investigated in pre-clinical comparative models. These studies have demonstrated a higher bone-to-implant contact for biomimetic calcium phosphate coatings than for uncoated titanium implants [69,93]. However, the osseointegration of titanium dental implants coated biomimetically has not yet been compared with other surface treatments in pre-clinical models.

5.3. *Incorporation of biologically active drugs into titanium dental implants*

The surface of titanium dental implants may be coated with bone-stimulating agents such as growth factors in order to enhance the bone healing process locally. Members of the transforming growth factor (TGF-β) superfamily, and

in particular bone morphogenetic proteins (BMPs), TGF-β1, platelet-derived growth factor (PDGF) and insulin-like growth factors (IGF-1 and 2) are some of the most promising candidates for this purpose. Experimental data, in which BMPs have been incorporated into dental implants, have been obtained from a variety of methodologies [94–99]. The limiting factor is that the active product has to be released progressively and not in a single burst. Another possibility may be the adjunction of a plasmid containing the gene coding for a BMP [100]. This possibility is limited due to the poor efficacy of inserting plasmids into the cells and the expression of the protein. In addition, overproduction of BMPs by cells might not be desirable after the bone healing process.

The surface of implants could also be loaded with molecules controlling the bone remodeling process. Incorporation of bone antiresorptive drugs, such as biphosphonates, might be very relevant in clinical cases lacking bone support, e.g. resorbed alveolar ridges. It has been shown recently that a biphosphonate incorporated on to titanium implants increased bone density locally in the peri-implant region [101]. The effect of the antiresorptive drug seems to be limited to the vicinity of the implant. Experimental in vivo studies have demonstrated the absence of negative effects but only a slight increase in dental implant osseointegration [102,103]. Other experimental studies using plasma-sprayed HA-coated dental implants immersed in pamidronate or zoledronate demonstrated a significant increase in bone contact area [104–106]. The main problem lies in the grafting and sustained release of antiresorptive drugs on the titanium implant surface. Due to the high chemical affinity of biphosphonates for calcium phosphate surfaces, incorporation of the antiresorptive drug on to dental implants could be achieved by using the biomimetic coating method at room temperatures. However, the ideal dose of antiresorptive drug will have to be determined because the increase in peri-implant bone density is biphosphonate concentration-dependent [106].

6. Conclusion

There are a number of surfaces commercially available for dental implants. Most of these surfaces have proven clinical efficacy (>95% over 5 years). However, the development of these surfaces has been empirical, requiring numerous in vitro and in vivo tests. Most of these tests were not standardized, using different surfaces, cell populations or animal models. The exact role of surface chemistry and topography on the early events of the osseointegration of dental implants remain poorly understood. Furthermore, comparative clinical studies with different implant surfaces are rarely performed. The future of dental implantology should aim at developing surfaces with controlled and standardized topography or chemistry. This approach is the only way to understand protein, cell and tissue interactions with implant surfaces. The local release of bone-stimulating or resorptive drugs in the peri-implant region may also respond to difficult clinical situations with poor bone quality and quantity. These therapeutic strategies should ultimately enhance the osseointegration process of dental implants for their immediate loading and long-term success.

Acknowledgements

The authors acknowledge Straumann AG (Bern, Switzerland) for providing the SLA samples, Astra Tech (Astra Zeneca, Rueil-Malmaison, France) for providing the TiOblast™ and OsseoSpeed™ samples. Cam Implants BV (Leiden, The Netherlands) is also acknowledged for providing the TPS and HA plasma-sprayed samples. We also thank Paul Pilet from the Miscoscopy Centre for SEM pictures and Kirsty Snaith for grammar corrections of the manuscript.

REFERENCES

[1] Albrektsson T, Branemark PI, Hansson HA, Lindstrom J. Osseointegrated titanium implants. Requirements for ensuring a long-lasting, direct bone-to-implant anchorage in man. Acta Orthop Scand 1981;52(2):155–70.
[2] Steinemann S. Titanium-the material of choice? Periodontology 2000 1998;17:7–21.
[3] Buser D, Broggini N, Wieland M, Schenk RK, Denzer AJ, Cochran DL, et al. Enhanced bone apposition to a chemically modified SLA titanium surface. J Dent Res 2004;83:529–33.
[4] Zhao G, Schwartz Z, Wieland M, Rupp F, Geis-Gerstorfer J, Cochran DL, et al. High surface energy enhances cell response to titanium substrate microstructure. J Biomed Mater Res A 2005;74:49–58.
[5] Bagno A, Di Bello C. Surface treatments and roughness properties of Ti-based biomaterials. J Mater Sci Mater Med 2004;15:935–49.
[6] Giavaresi G, Fini M, Cigada A, Chiesa R, Rondelli G, Rimondini L, et al. Mechanical and histomorphometric evaluations of titanium implants with different surface treatments inserted in sheep cortical bone. Biomaterials 2003;24:1583–94.
[7] Carlsson L, Albrektsson T, Berman C. Bone response to plasma-cleaned titanium implants. Int J Oral Maxillofac Implants 1989;4:199–204.
[8] Wennerberg A, Bolind P, Albrektsson T. Glow discharge pre-treated implants combined with temporary bone ischaemia. Swed Dent J 1991;15:95–101.
[9] Cochran DL, Schenk RK, Lussi A, Higginbottom FL, Buser D. Bone response to unloaded and loaded titanium implants with a sandblasted and acid-etched surface: a histometric study in the canine mandible. J Biomed Mater Res 1998;40:1–11.
[10] Wennerberg A, Hallgren C, Johansson C, Danelli S. A histomorphometric evaluation of screw-shaped implants each prepared with two surface roughnesses. Clin Oral Implants Res 1998;9:11–9.
[11] Buser D, Schenk R, Steinemann S, Fiorellini J, Fox C, Stich H. Influence of surface characteristics on bone integration of titanium implants. A histomorphometric study in miniature pigs. J Biomed Mater Res 1991;25:889–902.
[12] Gotfredsen K, Wennerberg A, Johansson C, Skovgaard LT, Hjorting-Hansen E. Anchorage of TiO_2-blasted, HA-coated, and machined implants: an experimental study with rabbits. J Biomed Mater Res 1995;29:1223–31.
[13] Wennerberg A, Albrektsson T, Albrektsson B, Krol JJ. Histomorphometric and removal torque study of screw-shaped titanium implants with three different surface topographies. Clin Oral Implant Res 1996;6:24–30.
[14] Becker W, Becker BE, Ricci A, Bahat O, Rosenberg E, Rose LF, et al. A prospective multicenter clinical trial comparing

one- and two-stage titanium screw-shaped fixtures with one-stage plasma-sprayed solid-screw fixtures. Clin Implant Dent Relat Res 2000;2:159–65.
[15] Albrektsson T, Wennerberg A. The impact of oral implants—past and future, 1966–2042. J Can Dent Assoc 2005;71:327.
[16] Hansson S, Norton M. The relation between surface roughness and interfacial shear strength for bone-anchored implants. A mathematical model. J Biomech 1999;32:829–36.
[17] Testori T, Wiseman L, Woolfe S, Porter S. A prospective multicenter clinical study of the Osseotite implant: four-year interim report. Int J Oral Maxillofac Implants 2001;16:193–200.
[18] Conner K, Sabatini R, Mealey B, Takacks V, Mills M, Cochran D. Guided bone regeneration around titanium plasma-sprayed, acid-etched and hydroxyapatite-coated implants in the canine model. J Periodontol 2003;74:658–68.
[19] Esposito M, Coulthard P, Thomsen P, Worthington HV. Interventions for replacing missing teeth: different types of dental implants. Cochrane Database Syst Rev 2005;25:CD003815.
[20] Brett PM, Harle J, Salih V, Mihoc R, Olsen I, Jones FH, et al. Roughness response genes in osteoblasts. Bone 2004;35:124–33.
[21] Urban RM, Jacobs JJ, Tomlinson MJ, Gavrilovic J, Black J, Peoch M. Dissemination of wear particles to the liver, spleen and abdominal lymph nodes of patients with hip or knee replacement. J Bone Jt Surg Am 2000;82:457–77.
[22] Browne M, Gregson PJ. Effect of mechanical surface pretreatment on metal ions release. Biomaterials 2000;21:385–92.
[23] Martini D, Fini M, De Pasquale V, Bacchelli B, Gamberini M, Tiniti A, et al. Detachment of titanium and fluorohydroxyapatite particles in unloaded endosseous implants. Biomaterials 2003;24:1309–16.
[24] Roccuzzo M, Bunino M, Prioglio F, Bianchi SD. Early loading of sandblasted and acid-etched (SLA) implants: a prospective split-mouth comparative study. Clin Oral Implants Res 2001;12:572–8.
[25] Taba Junior M, Novaes Junior AB, Souza SL, Grisi MF, Palioto DB, Pardini LC. Radiographic evaluation of dental implants with different surface treatments: an experimental study in dogs. Implant Dent 2003;12:252–8.
[26] Ong JL, Carnes DL, Bessho K. Evaluation of titanium plasma-sprayed and plasma-sprayed hydroxyapatite implants in vivo. Biomaterials 2004;25:4601–6.
[27] Aparicio C, Gil FJ, Fonseca C, Barbosa M, Planell JA. Corrosion behavior of commercially pure titanium shot blasted with different materials and size of shot particles for dental implant applications. Biomaterials 2003;24:263–73.
[28] Ivanoff CJ, Hallgren C, Widmark G, Sennerby L, Wennerberg A. Histologic evaluation of the bone integration of TiO(2) blasted and turned titanium microimplants in humans. Clin Oral Implants Res 2001;12:128–34.
[29] Rasmusson L, Kahnberg KE, Tan A. Effects of implant design and surface on bone regeneration and implant stability: an experimental study in the dog mandible. Clin Implant Dent Relat Res 2001;3:2–8.
[30] Gotfredsen K, Karlsson U. A prospective 5-year study of fixed partial prostheses supported by implants with machined and TiO_2-blasted surface. J Prosthodont 2001;10:2–7.
[31] Rasmusson L, Roos J, Bystedt H. A 10-year follow-up study of titanium dioxide-blasted implants. Clin Implant Dent Relat Res 2005;7:36–42.
[32] van Steenberghe D, De Mars G, Quirynen M, Jacobs R, Naert I. A prospective split-mouth comparative study of two screw-shaped self-tapping pure titanium implant systems. Clin Oral Implants Res 2000;11:202–9.
[33] Astrand P, Engquist B, Dahlgren S, Engquist E, Feldmann H, Grondahl K. Astra Tech and Branemark System implants: a prospective 5-year comparative study. Results after one year. Clin Implant Dent Relat Res 1999;1:17–26.
[34] Abron A, Hopfensperger M, Thompson J, Cooper L. Evaluation of a predictive model for implant surface topography effects on early osseointegration in the rat tibia model. J Prosth Dent 2001;85:40–6.
[35] Novaes A, Souza S, de Oliveira P, Souza A. Histomorphometric analysis of the bone-implant contact obtained with 4 different implant surface treatments placed side by side in the dog mandible. Int J Oral Maxillofac Implants 2002;17:377–83.
[36] Piatelli M, Scarano A, Paolantonio M, Iezzi G, Petrone G, Piatelli A. Bone response to machined and resorbable blast material titanium implants: an experimental study in rabbits. J Oral Implantol 2002;28:2–8.
[37] Mueller WD, Gross U, Fritz T, Voigt C, Fischer P, Berger G, et al. Evaluation of the interface between bone and titanium surfaces being blasted by aluminium oxide or bioceramic particles. Clin Oral Implants Res 2003;3:349–56.
[38] Massaro C, Rotolo F, De Riccardis F, Milella E, Napoli A, Wieland M, et al. Comparative investigation of the surface of commercial titanium dental implants. Part 1: chemical composition. J Mater Sci Mater Med 2002;13:535–48.
[39] Zinger O, Anselme K, Denzer A, Habersetzer P, Wieland M, Jeanfils J, et al. Time-dependent morphology and adhesion of osteoblastic cells on titanium model surfaces featuring scale-resolved topography. Biomaterials 2004;25:2695–711.
[40] Wong M, Eulenberger J, Schenk R, Hunziker E. Effect of surface topology on the osseointegration of implant materials in trabecular bone. J Biomed Mater Res 1995;29:1567–75.
[41] Cho SA, Park KT. The removal torque of titanium screw inserted in rabbit tibia treated by dual acid etching. Biomaterials 2003;24:3611–7.
[42] Park JY, Davies JE. Red blood cell and platelet interactions with titanium implant surfaces. Clin Oral Implants Res 2000;11:530–9.
[43] Trisi P, Lazzara R, Rebaudi A, Rao W, Testori T, Porter SS. Bone-implant contact on machined and dual acid-etched surfaces after 2 months of healing in the human maxilla. J Periodontol 2003;74:945–56.
[44] Davies JE. Mechanisms of endosseous integration. Int J Prosthodont 1998;11:391–401.
[45] Trisi P, Lazzara R, Rao W, Rebaudi A. Bone-implant contact and bone quality: evaluation of expected and actual bone contact on machined and osseotite implant surfaces. Int J Periodontics Restorative Dent 2002;22:535–45.
[46] Trisi P, Marcato C, Todisco M. Bone-to-implant apposition with machined and MTX microtextured implant surfaces in human sinus grafts. Int J Periodontics Restorative Dent 2003;23:427–37.
[47] Cochran DL, Buser D, ten Bruggenkate CM, Weingart D, Taylor TM, Bernard JP, et al. The use of reduced healing times on ITI implants with a sandblasted and acid-etched (SLA) surface: early results from clinical trials on ITI SLA implants. Clin Oral Implants Res 2002;13:144–53.
[48] Novaes Jr AB, Papalexiou V, Grisi MF, Souza SS, Taba Jr M, Kajiwara JK. Influence of implant microstructure on the osseointegration of immediate implants placed in periodontally infected sites. A histomorphometric study in dogs. Clin Oral Implants Res 2004;15:34–43.
[49] Papalexiou V, Novaes Jr AB, Grisi MF, Souza SS, Taba Jr M, Kajiwara JK. Influence of implant microstructure on the dynamics of bone healing around immediate implants placed into periodontally infected sites. A confocal laser

scanning microscopic study. Clin Oral Implants Res 2004;15:44–53.
[50] Ellingsen JE. Pre-treatment of titanium implants with fluoride improves their retention in bone. J Mater Sci Mater Med 1995;6:749–58.
[51] Ellingsen JE, Johansson CB, Wennerberg A, Holmen A. Improved retention and bone-to-implant contact with fluoride-modified titanium implants. Int J Oral Maxillofac Implants 2004;19:659–66.
[52] Cooper LF, Takabe J, Guo J, Abron A, Holmen A, Ellingsen JE. Fluoride modification effects on osteoblast behavior and bone formation at TiO(2) grit-blasted c.p. titanium endosseous implants. Biomaterials 2006;27:926–36.
[53] Yokoyama K, Ichikawa T, Murakami H, Miyamoto Y, Asaoka K. Fracture mechanisms of retrieved titanium screw thread in dental implants. Biomaterials 2002;23:2459–65.
[54] Sul YT, Johansson CB, Jeong Y, Roser K, Wennerberg A, Albrektsson T. Oxidized implants and their influence on the bone response. J Mater Sci Mater Med 2001;12:1025–31.
[55] Sul YT, Johansson C, Wennerberg A, Cho LR, Chang BS, Albrektsson T. Optimum surface properties of oxidized implants for reinforcement of osseointegration: surface chemistry, oxide thickness, porosity, roughness, and crystal structure. Int J Oral Maxillofac Implants 2005;20:349–59.
[56] Xiropaidis AV, Qahash M, Lim WH, Shanaman RH, Rohrer MD, Wikesjo UM, et al. Bone-implant contact at calcium phosphate-coated and porous titanium oxide (TiUnite)-modified oral implants. Clin Oral Implants Res 2005;16:532–9.
[57] Huang YH, Xiropaidis AV, Sorensen RG, Albandar JM, Hall J, Wikesjo UM. Bone formation at titanium porous oxide (TiUnite) oral implants in type IV bone. Clin Oral Implants Res 2005;16:105–11.
[58] Sul YT, Johansson CB, Roser K, Albrektsson T. Qualitative and quantitative observations of bone tissue reactions to anodised implants. Biomaterials 2002;23:1809–17.
[59] Sul YT, Johansson CB, Jeong Y, Wennerberg A, Albrektsson T. Resonance frequency and removal torque analysis of implants with turned and anodized surface oxides. Clin Oral Implants Res 2002;13:252–9.
[60] Rocci A, Martignoni M, Gottlow J. Immediate loading of Branemark System TiUnite and machined-surface implants in the posterior mandible: a randomized open-ended clinical trial. Clin Implant Dent Relat Res 2003;5:S57–63.
[61] Jungner M, Lundqvist P, Lundgren S. Oxidized titanium implants (Nobel Biocare TiUnite) compared with turned titanium implants (Nobel Biocare mark III) with respect to implant failure in a group of consecutive patients treated with early functional loading and two-stage protocol. Clin Oral Implants Res 2005;16:308–12.
[62] Schupbach P, Glauser R, Rocci A, Martignoni M, Sennerby L, Lundgren A, et al. The human bone-oxidized titanium implant interface: a light microscopic, scanning electron microscopic, back-scatter scanning electron microscopic, and energy-dispersive X-ray study of clinically retrieved dental implants. Clin Implant Dent Relat Res 2005;7:S36–43.
[63] Sul YT, Johansson CB, Albrektsson T. Oxidized titanium screws coated with calcium ions and their performance in rabbit bone. Int J Oral Maxillofac Implants 2002;17:625–34.
[64] Sul YT, Byon ES, Jeong Y. Biomechanical measurements of calcium-incorporated oxidized implants in rabbit bone: effect of calcium surface chemistry of a novel implant. Clin Implant Dent Relat Res 2004;6:101–10.
[65] de Groot K, Wolke JG, Jansen JA. Calcium phosphate coatings for medical implants. Proc Inst Mech Eng 1998;212:137–47.
[66] Daculsi G, Laboux O, Malard O, Weiss P. Current state of the art of biphasic calcium phosphate bioceramics. J Mater Sci Mater Med 2003;14:195–200.
[67] Davies JE. Understanding peri-implant endosseous healing. J Dent Educ 2003;67:932–49.
[68] Morris HF, Ochi S, Spray JR, Olson JW. Periodontal-type measurements associated with hydroxyapatite-coated and non-HA-coated implants: uncovering to 36 months. Ann Periodontol 2000;5:56–67.
[69] Barrere F, van der Valk CM, Meijer G, Dalmeijer RA, de Groot K, Layrolle P. Osteointegration of biomimetic apatite coating applied onto dense and porous metal implants in femurs of goats. J Biomed Mater Res 2003;67:655–65.
[70] Geurs NC, Jeffcoat RL, McGlumphy EA, Reddy MS, Jeffcoat MK. Influence of implant geometry and surface characteristics on progressive osseointegration. Int J Oral Maxillofac Implants 2002;17:811–5.
[71] Filiaggi MJ, Coombs NA, Pilliar RM. Characterization of the interface in the plasma-sprayed HA coating/Ti-Al6-4V implant system. J Biomed Mater Res 1991;25:1211–30.
[72] Radin S, Ducheyne P. Plasma spraying induced changes of calcium phosphate ceramic characteristics and the effect on in vitro stability. Mater Med 1992;3:33–42.
[73] De Groot K, Wolke JCG, Jansen JA. State of the art: hydroxylapatite coatings for dental implants. J Oral Implant 1994;20:232–4.
[74] Kim Y, LeGeros J, LeGeros RZ. Characterization of commercial HA-coated implants. J Dent Res 1994;73:137 [abstract no. 287].
[75] LeGeros RZ, LeGeros JP, Kim Y, Kijkowska R, Zheng R, Bautista C, et al. Calcium phosphates in plasma-sprayed HA coatings. Ceram Trans 1995;48:173–89.
[76] Wheeler S. Eight-year clinical retrospective study of titanium plasma-sprayed and hydroxyapatite-coated cylinder implants. Int J Oral Maxillofac Implants 1996;11:340–50.
[77] Chang YL, Lew D, Park JB, Keller JC. Biomechanical and morphometric analysis of hydroxyapatite-coated implants with varying cristallinity. J Oral Maxillofac Surg 1999;57:1096–108.
[78] Lee J, Rouhfar L, Beirne O. Survival of hydroxypatite-coated implants: a meta-analytic review. J Oral Maxillofac Surg 2000;58:1372–9 [discussion 1379–80].
[79] Tinsley D, Watson C, Russell J. A comparison of hydroxyapatite coated implant retained fixed and removable mandibular prostheses over 4 to 6 years. Clin Oral Implant Res 2001;12:159–66.
[80] Anselme K, Bigerelle M, Noel B, Iost A, Hardouin P. Effect of grooved titanium substratum on human osteoblastic cell growth. J Biomed Mater Res 2002;60:529–40.
[81] Bigerelle M, Anselme K, Noel B, Ruderman I, Hardouin P, Iost A. Improvement in the morphology of Ti-based surfaces: a new process to increase in vitro human osteoblast response. Biomaterials 2002;23:1563–77.
[82] Zhu X, Chen J, Scheideler L, Altebaeumer T, Geis-Gerstorfer J, Kern D. Cellular reactions of osteoblasts to micron- and submicron-scale porous structures of titanium surfaces. Cells Tissues Organs 2004;178:13–22.
[83] Wang X, Yan W, Hayakawa S, Tsuru K, Osaka A. Apatite deposition on thermally and anodically oxidized titanium surfaces in a simulated body fluid. Biomaterials 2003;24:4631–7.
[84] Yang B, Uchida M, Kim HM, Zhang X, Kokubo T. Preparation of bioactive titanium metal via anodic oxidation treatment. Biomaterials 2004;25:1003–10.
[85] Wang J, de Boer J, de Groot K. Preparation and characterization of electrodeposited calcium phosphate/chitosan coating on Ti6Al4V plates. J Dent Res 2004;83:296–301.
[86] Ban S, Maruno S. Deposition of calcium phosphate on titanium by electrochemical process in simulated body fluid. Jpn J Appl Phys 1993;32:1577–80.

[87] Sena LA, Andrade MC, Rossi AM, Soares GA. Hydroxyapatite deposition by electrophoresis on titanium sheets with different surface finishing. J Biomed Mater Res 2002;60:1–7.
[88] Kokubo T, Kushitani H, Abe Y, Yamamuro T. Apatite coating on various substrates in simulated body fluids. Bioceramics 1989;2:235–42.
[89] Habibovic P, Barrère F, van Blitterswijk CA, de Groot K, Layrolle P. Biomimetic hydroxyapatite coating on metal implants. J Am Ceram Soc 2002;85:517–22.
[90] Barrere F, Snel M, Van Blitterswijk C, de Groot K, Layrolle P. Nano-scale study of the nucleation and growth of calcium phosphate coating on titanium implants. Biomaterials 2004;25:2901–10.
[91] Barrere F, van der Valk CM, Dalmeijer RA, van Blitterswijk CA, de Groot K, Layrolle P. In vitro and in vivo degradation of biomimetic octacalcium phosphate and carbonate apatite coatings on titanium implants. J Biomed Mater Res 2003;64:378–87.
[92] Leeuwenburgh S, Layrolle P, Barrère F, de Bruijn J, Schoonman J, van Blitterswijk CA, et al. Osteoclastic resorption of biomimetic calcium phosphate coatings in vitro. J Biomed Mater Res 2001;56:208–15.
[93] Habibovic P, Li J, van der Valk CM, Meijer G, Layrolle P, van Blitterswijk CA, et al. Biological performance of uncoated and octacalcium phosphate-coated Ti6Al4V. Biomaterials 2005;26:23–36.
[94] Bessho K, Carnes DL, Cavin R, Chen HY, Ong JL. BMP stimulation of bone response adjacent to titanium implants in vivo. Clin Oral Implants Res 1999;10: 212–8.
[95] Wikesjo UM, Sorensen RG, Kinoshita A, Wozney JM. RhBMP-2/alphaBSM induces significant vertical alveolar ridge augmentation and dental implant osseointegration. Clin Implant Dent Relat Res 2002;4:174–82.
[96] Tatakis DN, Koh A, Jin L, Wozney JM, Rohrer MD, Wikesjo UM. Peri-implant bone regeneration using recombinant human bone morphogenetic protein-2 in a canine model: a dose-response study. J Periodontal Res 2002;37:93–100.
[97] Stenport VF, Roos-Jansaker AM, Renvert S, Kuboki Y, Irwin C, Albrektsson T, et al. Failure to induce supracrestal bone growth between and around partially inserted titanium implants using bone morphogenetic protein (BMP): an experimental study in dogs. Clin Oral Implants Res 2003;14:219–25.
[98] Boyne P, Jones SD. Demonstration of the osseoinductive effect of bone morphogenetic protein within endosseous dental implants. Implant Dent 2004;13:180–4.
[99] Liu Y, de Groot K, Hunziker EB. BMP-2 liberated from biomimetic implant coatings induces and sustains direct ossification in an ectopic rat model. Bone 2005;36:745–57.
[100] Huang YC, Simmons C, Kaigler D, Rice KG, Mooney DJ. Bone regeneration in a rat cranial defect with delivery of PEI-condensed plasmid DNA encoding for bone morphogenetic protein-4 (BMP-4). Gene Ther 2005;12:418–26.
[101] Josse S, Faucheux C, Soueidan A, Grimandi G, Massiot D, A1onso B, et al. Chemically modified calcium phosphates as novel materials for bisphosphonate delivery. Adv Mater 2004;16:1423–7.
[102] Meraw SJ, Reeve CM. Qualitative analysis of peripheral peri-implant bone and influence of alendronate sodium on early bone regeneration. J Periodontol 1999;70:1228–33.
[103] Meraw SJ, Reeve CM, Wollan PC. Use of alendronate in peri-implant defect regeneration. J Periodontol 1999;70:151–8.
[104] Yoshinari M, Oda Y, Ueki H, Yokose S. Immobilization of bisphosphonates on surface modified titanium. Biomaterials 2001;22:709–15.
[105] Kajiwara H, Yamaza T, Yoshinari M, Goto T, Iyama S, Atsuta I, et al. The bisphosphonate pamidronate on the surface of titanium stimulates bone formation around tibial implants in rats. Biomaterials 2005;26:581–7.
[106] Peter B, Pioletti DP, Laib S, Bujoli B, Pilet P, Janvier P, et al. Calcium phosphate drug delivery system: influence of local zoledronate release on bone implant osteointegration. Bone 2005;36:52–60.
[107] Mabboux F, Ponsonnet L, Morrier JJ, Jaffrezic N, Barsotti O. Surface free energy and bacterial retention to saliva-coated dental implant materials—an in vitro study. Colloids Surf B Biointerfaces 2004;39:199–205.
[108] Ferraz MP, Monteiro FJ, Serro AP, Saramago B, Gibson IR, Santos JD. Effect of chemical composition on hydrophobicity and zeta potential of plasma sprayed HA/CaO-P_2O_5 glass coatings. Biomaterials 2001;22:3105–12.

Exhibit A-2

Sergey V. Dorozhkin and Matthias Epple. Biological and Medical Significance of Calcium Phosphates. Angewandte Chemie International Edition. 2002 41(17): 3130-3146.


Fertilizers
Hydroxyapatite
$Ca_5(PO_4)_3OH$
Brushite
$Ca_3(PO_4)_2$
DCPD
Bone
Implants
$CaHPO_4$
Teeth
β-TCP
Tricalcium phosphate
ANGEWANDTE
CHEMIE
© WILEY-VCH

Biological and Medical Significance of Calcium Phosphates

Sergey V. Dorozhkin and Matthias Epple*

Dedicated to Professor Sir John Meurig Thomas on the occasion of his 70th birthday

The inorganic part of hard tissues (bones and teeth) of mammals consists of calcium phosphate, mainly of apatitic structure. Similarly, most undesired calcifications (i.e. those appearing as a result of various diseases) of mammals also contain calcium phosphate. For example, atherosclerosis results in blood-vessel blockage caused by a solid composite of cholesterol with calcium phosphate. Dental caries result in a replacement of less soluble and hard apatite by more soluble and softer calcium hydrogenphosphates. Osteoporosis is a demineralization of bone. Therefore, from a chemical point of view, processes of normal (bone and teeth formation and growth) and pathological (atherosclerosis and dental calculus) calcifications are just an in vivo crystallization of calcium phosphate. Similarly, dental caries and osteoporosis can be considered to be in vivo dissolution of calcium phosphates. On the other hand, because of the chemical similarity with biological calcified tissues, all calcium phosphates are remarkably biocompatible. This property is widely used in medicine for biomaterials that are either entirely made of or coated with calcium phosphate. For example, self-setting bone cements made of calcium phosphates are helpful in bone repair and titanium substitutes covered with a surface layer of calcium phosphates are used for hip-joint endoprostheses and tooth substitutes, to facilitate the growth of bone and thereby raise the mechanical stability. Calcium phosphates have a great biological and medical significance and in this review we give an overview of the current knowledge in this subject.

Keywords: bioinorganic chemistry · biomaterials · biomimetic synthesis · biomineralization · materials science

1. Introduction

Calcium phosphates are the most important inorganic constituents of biological hard tissues. In the form of carbonated hydroxyapatite (HA), they are present in bone, teeth, and tendons to give these organs stability, hardness, and function. Calcium phosphate crystals are also found in "dead" nature as mineral deposits of considerable size, having grown over many years under sometimes extreme conditions of pressure and temperature. In contrast, biologically formed calcium phosphates are often nanocrystals that are precipitated under mild conditions (ambient pressure, near room temperature).

The biological formation of minerals by living organisms is commonly called "biomineralization".[1–9] Today more than 60 minerals are known that are used by organisms, for example, for protection (shell), as tools (teeth), as gravity sensors (octoconia or statoliths), or as a skeleton. In terms of absolute quantity, calcium phosphates are minor compared to calcium carbonate ($CaCO_3$) and silicon dioxide (as silicic acid $SiO_2 \cdot n H_2O$), which both occur in huge amounts in marine single-cell organisms. Another very important class of biominerals are iron oxides that occur, for example, in snail teeth or magnetotactic bacteria.[1] The presence of calcium phosphates in vertebrates (such as humans) makes them particularly important in biomedicine, as many diseases result from irregularities in the skeletal system (i.e. in bone) or the dental system (in teeth). It must also be stressed that, although the presence of calcium phosphate in these hard tissues is crucial for survival, there are occasions on which calcium phosphate minerals crystallize in an irregular way in undesired regions. These phenomena are called pathological crystallization or ectopic mineralization, of which atherosclerosis, stone formation, or dental calculus are prominent examples.

Herein, we give an overview of the occurrence, formation, and significance of calcium phosphate minerals in living organisms, with a special emphasis on current biomedical questions.

[*] Prof. Dr. M. Epple, Dr. S. V. Dorozhkin
Solid-State Chemistry, Faculty of Chemistry
University of Bochum
Universitätsstrasse 150, 44780 Bochum (Germany)
Fax: (+49) 234-321-4558
E-mail: matthias.epple@ruhr-uni-bochum.de

  1433-7851/02/4117-3131 $ 20.00+.50/0

2. Geological and Biological Occurrence

Calcium and phosphorus are widely distributed elements on our planet. The surface layer of the Earth contains about 3.4 wt% of calcium and 0.10 wt% of phosphorus.[10] Combinations of oxides of these two elements with or without incorporation of water give different calcium phosphates. Unless doped with a colored transition-metal ion (often the case in nature), all calcium phosphates are white solids. Most calcium phosphates are only sparingly soluble in water, and some can be considered to be insoluble, but all dissolve in acids. Ortho- (PO_4^{3-}), pyro- ($P_2O_7^{4-}$), and poly- ($(PO_3)_n^{n-}$) phosphates can be structurally distinguished. Although calcium pyrophosphates occur in some pathological calcifications, only calcium orthophosphates will be considered here. They are the major component of all human calcified tissues, and natural calcium orthophosphates are the source for phosphorus-containing fertilizers.[11–14]

Geologically, natural calcium orthophosphates are found in different regions to fluoroapatite deposits, $Ca_{10}(PO_4)_6F_2$, or phosphorites. Most geological environments contain calcium phosphates, usually as accessory minerals (<5%). In some sedimentary rocks (phosphorites) and rarely in igneous segregations (fluoroapatite), the concentration is high enough to permit an economic use. The largest world deposits of natural phosphate rock are located in Morocco, Russia, Kazakhstan, and the USA (Florida, Tennessee).[11–14] Most natural calcium phosphates occur as small polycrystals. Larger crystals usually have the crystal structure of apatites (hexagonal system, space group $P6_3/m$, or monoclinic system, space group $P2_1/b$). None of these crystals are pure compounds; they are always admixtures of other elements. For example, calcium ions may be partially replaced by Sr, Ba, Mg, K, Na, Fe; phosphate ions may be replaced by AsO_4^{3-}, CO_3^{2-}, and VO_4^{3-}; hydroxide, chloride, bromide, carbonate, and oxide ions may substitute fluoride ions in the crystal lattice. Moreover, some ions in the crystal structure may be missing, which leaves crystallographic defects. This leads to the formation of nonstoichiometric compounds. Figure 1 shows polycrystalline and single-crystalline calcium phosphate minerals.

The major industrial application of calcium phosphate minerals is in the production of agricultural fertilizers. Natural calcium phosphates that are used for fertilizer production can be of geological or of biological origin for example, guano

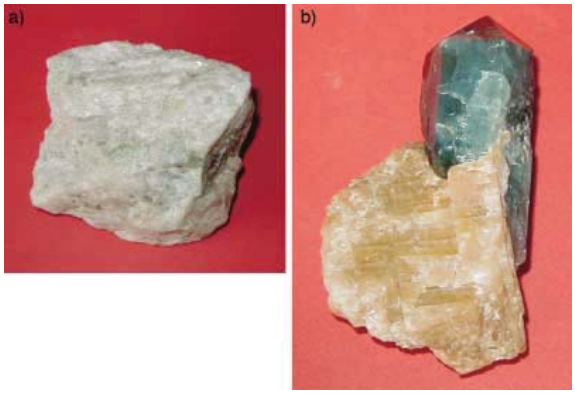

Figure 1. Polycrystalline (a) and single-crystalline (b) fluoroapatite (chemical formula: $Ca_{10}(PO_4)_6F_2$) of geological origin. The single crystal has a grey–green color caused by incorporated transition metals.

Matthias Epple studied chemistry at the Technical University of Braunschweig and obtained his Ph.D. in 1992 (Prof. H. K. Cammenga). In 1993, he held a postdoctoral position at the University of Washington (Seattle, Prof. J. C. Berg). From 1994 to 1997 he worked on his Habilitation in the group of Prof. Reller at the University of Hamburg, interrupted by research stays at the Royal Institution in London with Prof. J. M. Thomas. In 1998, he received the Heinz-Maier-Leibnitz prize and a Heisenberg stipend from the DFG. Since 2000, he has been Professor of Inorganic Chemistry at the University of Bochum. His research interests include the reactivity of solids, molecular crystals, synchrotron radiation, biomaterials, and biomineralization. He has authored more than 90 publications in these fields. He is also a member of the advisory board for synchrotron radiation at the German Electron Synchrotron Facility (DESY, Hamburg) and a member of the board of the Ruhr Competence Center of Medical Technology.

M. Epple

S. V. Dorozhkin

Dr. Sergey V. Dorozhkin studied chemistry and chemical engineering at the Moscow Institute of Chemical Technology, Moscow, USSR. Later he joined the Research Institute of Fertilizers (Moscow, USSR) where he worked on the dissolution mechanism of natural fluoroapatite. He received his Ph.D. degree under the supervision of Prof. Igor V. Melikhov (Chemistry Department of the M. V. Lomosonov Moscow State University, Russia) in 1992. Since that he has worked as a post-doctoral researcher on calcium phosphates and biomaterials at the Universities of Strasburg and Nantes (both France), as well as at the University of Aveiro (Portugal). From 2000 to 2002 he was a post-doctoral researcher on biomineralization at the Department of Solid-State Chemistry of the University of Bochum (Germany).

(mineralized excrements of birds, accumulated over thousands of years, e.g. in the South Sea at Nauru, Banaba, and Makatea). On the 21 km^2 island of Nauru, about 2 million tons of fertilizers are mined every year, which is leading to severe ecological problems. The total capacity of industrial plants in the world exceeds 25 million tons of phosphate fertilizers per year (as P_2O_5).[12]

In biological systems, calcium orthophosphates occur as the principal inorganic constituent of normal (bones, teeth, fish enameloid, and some species of shells) and pathological (dental and urinary calculus and stones, atherosclerotic lesions) calcifications.[15–18] Structurally, they occur mainly in the form of poorly crystallized nonstoichiometric sodium-, magnesium-, and carbonate-containing HA (often called "biological apatite" or dahllite). The main constituents of human bones are calcium orthophosphates (≈50–60 wt%), collagen (≈30–40 wt%), and water (≈10 wt%). In microscopic studies of the interface between implanted calcium phosphate biomaterials and the host bone, poorly crystallized nonstoichiometric carbonated apatite similar to that of bone apatite was found.[19–21] Detailed information on the chemical composition of the most important human normal calcified tissues is given in Table 1. Figure 2 shows a picture of a calcined bone, that is, only the calcium phosphate skeleton, after burning off all organic components.

As a variety of stoichiometric calcium phosphates is known, abbreviations have traditionally been introduced to distinguish between the different compounds. Important parameters are the molar Ca/P ratio and the solubility. Table 2 presents the known calcium phosphate phases. For the chemically pure compounds, the Ca/P ratio can be between 0.5–2.0. In general, the lower this ratio, the more acidic and soluble in water the calcium phosphate is (see ref. [22] for the apparent solubility of these phases as a function of pH value and calcium concentration). A brief description of all calcium orthophosphates is given below. Table 3 contains their crystallographic data.

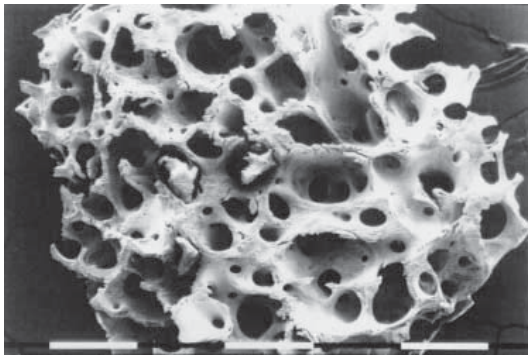

Figure 2. Calcined porous bone (*spongiosa*) showing the high porosity and the interconnecting network of pores (magnification: 20.4 ×).

MCPM (monocalcium phosphate monohydrate, $Ca(H_2PO_4)_2 \cdot H_2O$) is the most acidic and water-soluble calcium phosphate compound. It precipitates from highly acidic solutions that are normally used in the industrial production of phosphorus-containing fertilizer ("triple superphosphate").[12] At temperatures above 100 °C, it transforms into MCPA (monocalcium phosphate anhydrate, $Ca(H_2PO_4)_2$). Because of its comparatively high acidity and solubility, MCPM is never found in biological calcifications. However, MCPM is used in some calcium phosphate cements in medicine.[23–27] Other applications are as antacids, acidulents, and mineral supplements for baking powders, foods, and beverages.[28]

MCPA is the anhydrous form of MCPM. It crystallizes under similar conditions as MCPM but at temperatures above 100 °C (e.g. from highly concentrated mother liquors in fertilizer production). Like MCPM, MCPA never appears in calcified tissues, and there is no current application in medicine; it is mainly used as a fertilizer.[12, 28]

DCPD (dicalcium phosphate dihydrate, $CaHPO_4 \cdot 2H_2O$; the mineral brushite) can be easily crystallized from aqueous

Table 1. Comparative composition and structural parameters of inorganic phases of adult-human calcified tissues.[a][15, 21]

Composition	Enamel	Dentin	Bone	Hydroxyapatite (HA)
calcium [wt%][b]	36.5	35.1	34.8	39.6
phosphorus (as P) [wt%][b]	17.7	16.9	15.2	18.5
Ca/P (molar ratio)[b]	1.63	1.61	1.71	1.67
sodium [wt%][b]	0.5	0.6	0.9	–
magnesium [wt%][b]	0.44	1.23	0.72	–
potassium [wt%][b]	0.08	0.05	0.03	–
carbonate (as CO_3^{2-}) [wt%][c]	3.5	5.6	7.4	–
fluoride [wt%][b]	0.01	0.06	0.03	–
chloride [wt%][b]	0.30	0.01	0.13	–
pyrophosphate,(as $P_2O_7^{4-}$) [wt%][c]	0.022	0.10	0.07	–
total inorganic [wt%][c]	97	70	65	100
total organic [wt%][c]	1.5	20	25	–
water [wt%][c]	1.5	10	10	–
a axis [Å][d]	9.441	9.421	9.41	9.430
c axis [Å][d]	6.880	6.887	6.89	6.891
crystallinity index, (HA = 100)	70–75	33–37	33–37	100
typical crystal sizes [nm][1, 105, 107]	100 × 50 × 50μm	35 × 25 × 4	50 × 25 × 4	200–600
ignition products (800 °C)	β-TCP + HA	β-TCP + HA	HA + CaO	HA
elasticity modulus (GPa)[261]	80	15	0.34–13.8	10
compressive strength (MPa)	10	100	150	100

[a] Because of the considerable variation found in biological samples, typical values are given in these cases. [b] Ashed samples. [c] Unashed samples. [d] Lattice parameters: ± 0.003 Å.

Table 2. Properties of the biologically relevant calcium orthophosphates.[a][103, 104]

Ca/P ratio	Compound	Formula	Solubility at 25 °C, $-\log(K_{sp})$	Solubility at 37 °C, $-\log(K_{sp})$	pH stability range in aqueous solution at 25 °C
0.5	monocalcium phosphate monohydrate (MCPM)	$Ca(H_2PO_4)_2 \cdot H_2O$	1.14	no data	0.0 – 2.0
0.5	monocalcium phosphate anhydrate (MCPA)	$Ca(H_2PO_4)_2$	1.14	no data	[d]
1.0	dicalcium phosphate dihydrate (DCPD, "brushite")	$CaHPO_4 \cdot 2H_2O$	6.59	6.63	2.0 – 6.0
1.0	dicalcium phosphate anhydrate (DCPA, "monetite")	$CaHPO_4$	6.90	7.02	[d]
1.33	octacalcium phosphate (OCP)	$Ca_8(HPO_4)_2(PO_4)_4 \cdot 5H_2O$	96.6	95.9	5.5 – 7.0
1.5	α-tricalcium phosphate (α-TCP)	$\alpha\text{-}Ca_3(PO_4)_2$	25.5	25.5	[b]
1.5	β-tricalcium phosphate (β-TCP)	$\beta\text{-}Ca_3(PO_4)_2$	28.9	29.5	[b]
1.2 – 2.2	amorphous calcium phosphate (ACP)	$Ca_x(PO_4)_y \cdot n H_2O$	[c]	[c]	[e]
1.5 – 1.67	calcium-deficient hydroxyapatite (CDHA)	$Ca_{10-x}(HPO_4)_x(PO_4)_{6-x}(OH)_{2-x}$ $(0 < x < 1)$	≈ 85.1	≈ 85.1	6.5 – 9.5
1.67	hydroxyapatite (HA)	$Ca_{10}(PO_4)_6(OH)_2$	116.8	117.2	9.5 – 12
2.0	tetracalcium phosphate (TTCP)	$Ca_4(PO_4)_2O$	38 – 44	37 – 42	[b]

[a] The solubility is given as the logarithm of the ion product of the given formulae (excluding hydrate water) with concentrations in mol L^{-1}. [b] These compounds cannot be precipitated from aqueous solutions. [c] Cannot be measured precisely. However, the following values were reported: 25.7 ± 0.1 (pH 7.40), 29.9 ± 0.1 (pH 6.00), 32.7 ± 0.1 (pH 5.28).[78] [d] Stable at temperatures above 100 °C. [e] Always metastable. The composition of a precipitate depends on the solution pH value and composition.

Table 3. Crystallographic data of calcium phosphates.[72, 73]

Compound	Space group	Unit cell parameters[a]	Z[b]	Density [g cm^{-3}]
MCPM	triclinic $P\bar{1}$	$a = 5.6261(5)$, $b = 11.889(2)$, $c = 6.4731(8)$ $\alpha = 98.633(6)$, $\beta = 118.262(6)$, $\gamma = 83.344(6)$	2	2.23
MCPA	triclinic $P\bar{1}$	$a = 7.5577(5)$, $b = 8.2531(6)$, $c = 5.5504(3)$ $\alpha = 109.87(1)$, $\beta = 93.68(1)$, $\gamma = 109.15(1)$	2	2.58
DCPD	monoclinic Ia	$a = 5.812(2)$, $b = 15.180(3)$, $c = 6.239(2)$ $\beta = 116.42(3)$	4	2.32
DCPA	triclinic $P\bar{1}$	$a = 6.910(1)$, $b = 6.627(2)$, $c = 6.998(2)$ $\alpha = 96.34(2)$, $\beta = 103.82(2)$, $\gamma = 88.33(2)$	4	2.89
OCP	triclinic $P\bar{1}$	$a = 19.692(4)$, $b = 9.523(2)$, $c = 6.835(2)$ $\alpha = 90.15(2)$, $\beta = 92.54(2)$, $\gamma = 108.65(1)$	1	2.61
α-TCP	monoclinic $P2_1/a$	$a = 12.887(2)$, $b = 27.280(4)$, $c = 15.219(2)$ $\beta = 126.20(1)$	24	2.86
β-TCP	rhombohedral $R3cH$	$a = b = 10.439(1)$, $c = 37.375(6)$ $\gamma = 120$	21[c]	3.07
HA	monoclinic $P2_1/b$	$a = 9.84214(8)$, $b = 2a$, $c = 6.8814(7)$ $\gamma = 120$ (monoclinic)	4	3.16
	or hexagonal $P6_3/m$	$a = b = 9.4302(5)$, $c = 6.8911(2)$ $\gamma = 120$ (hexagonal)	2	
TTCP	monoclinic $P2_1$	$a = 7.023(1)$, $b = 11.986(4)$, $c = 9.473(2)$ $\beta = 90.90(1)$	4	3.05

[a] a, b, c are given in Å and α, β, γ in °. [b] Number of formula units per unit cell. [c] Per hexagonal unit cell.

solutions. DCPD transforms into dicalcium phosphate anhydrate at temperatures above 80 °C. DCPD is of biological importance because it is often found in pathological calcifications (dental calculi, crystalluria, chondrocalcinosis,[15–17] and urinary stones[18]). DCPD has been proposed as an intermediate in both bone mineralization and dissolution of enamel in acids (dental caries).[15–18] In surgery, DCPD is used in calcium phosphate cements[27, 29–34] and, in dentistry, in toothpaste together with fluoride-containing compounds (e.g. NaF) for protection against caries.[35–38] Other applications are in fertilizers,[12] glass production, calcium supplements in foods, and mineral supplements in cereals.[28]

DCPA (dicalcium phosphate anhydrate, $CaHPO_4$; the mineral monetite) is the anhydrous form of DCPD. DCPA, like DCPD, can be crystallized from aqueous solutions but at 100 °C. Unlike DCPD, DCPA occurs in neither normal nor pathological calcifications. It is used in calcium phosphate cements,[33, 39–44] and other applications are as polishing agents, sources of calcium and phosphate in nutritional supplements, tabletting aids, and toothpaste components.[28]

OCP (octacalcium phosphate, $Ca_8(HPO_4)_2(PO_4)_4 \cdot 5H_2O$) is often found as an intermediate phase during the precipitation of the thermodynamically more stable calcium phosphates (e.g. HA, calcium-deficient HA (CDHA)) from aqueous solutions. OCP consists of apatitic layers (with atomic arrangements of calcium and phosphate ions similar to those of HA) separated by hydrated layers (water molecules). OCP is of great biological importance because it is one of the stable components of human dental and urinary calculi.[45–47] It plays an important role in the in vivo formation of apatitic biominerals. A "central OCP inclusion" (also known as "central dark line") is seen by transmission electron microscopy in many biological apatites and in some synthetically precipitated HA (see below for a detailed discussion).[48–51] Although OCP has not been observed in vascular calcifications, it has been strongly suggested as the precursor phase to

biological apatites found in natural and prosthetic heart valves.[52, 53]

β-TCP (β-tricalcium phosphate) is the "true calcium orthophosphate" of the stoichiometric composition $Ca_3(PO_4)_2$. It cannot be precipitated from solution, but may only be prepared by calcination, e.g. of CDHA (see below), at temperatures above 800 °C [Eq. (1)]:

$$Ca_9(HPO_4)(PO_4)_5OH \rightarrow 3\,Ca_3(PO_4)_2 + H_2O \quad (1)$$

At temperatures above 1125 °C, it transforms into the high-temperature phase α-TCP. Being the stable phase at room temperature, β-TCP is less soluble in water than α-TCP (Table 2). Pure β-TCP never occurs in biological calcifications. Only the magnesium-containing form called "whitlockite" (chemical formula: β-$(Ca,Mg)_3(PO_4)_2$) is found in dental calculi and urinary stones,[15–18, 54] dental caries, salivary stones, arthritic cartilage, as well as in some soft-tissue deposits.[15–18] In biomedicine, β-TCP is used in calcium phosphate bone cements.[23, 24, 55–58] In combination with HA, β-TCP is used as a "biphasic calcium phosphate" ("BCP")[59–65] as a bone-substitution ceramic. Other applications include fertilizers,[12] polishing and dental powders, porcelains, pottery, enamel, and animal food supplements.[28]

α-TCP (α-tricalcium phosphate, α-$Ca_3(PO_4)_2$) is a metastable phase at room temperature, prepared from β-TCP at above 1125 °C. α-TCP is more reactive in aqueous systems than β-TCP and can be hydrolyzed to a mixture of other calcium phosphates. It never occurs in biological calcifications and has a limited application in medicine in calcium phosphate cements.[26, 31, 33, 34, 41–44, 66] α-TCP is also used as a fertilizer.[28]

ACP (amorphous calcium phosphate) is often encountered as a transient phase during the formation of calcium phosphates in aqueous systems. Usually, ACP is the first phase that is precipitated from a supersaturated solution prepared by rapid mixing of solutions containing of calcium cations and phosphate anions.[67–71] The chemical composition of ACP strongly depends on the solution pH value and the concentrations of calcium and phosphate ions in the mother liquor. For example, ACP phases with Ca/P ratios in the range of 1.18:1 (precipitated at solution pH 6.6) to 1.53:1 (precipitated at solution pH 11.7)[72, 73] and even up to 2.5:1[15–17] have been described.

The structure of ACP is still uncertain. IR spectra of ACP show broad, featureless phosphate absorption bands. The compounds are amorphous, according to X-ray diffraction experiments. Electron microscopy of ACP usually reveals spherical particles with typical diameters of 20–200 nm. However, it is likely that ACP has an apatitic short-range structure, but with a crystal size so small that it appears amorphous in X-ray diffraction experiments (no coherent X-ray scattering). This is supported by X-ray absorption spectroscopic data (EXAFS; extended X-ray absorption fine structure) on biogenic and synthetic samples.[74–77] On the other hand, it was proposed that the basic structural unit of ACP is a 9.5 Å diameter, roughly spherical cluster of ions with the composition $Ca_9(PO_4)_6$.[72, 73] These clusters were found experimentally as seed nuclei during the crystallization of HA, and a model was developed to describe the crystallization of HA as a stepwise assembly of these units.[78] Biologically, ACP (often containing magnesium, carbonate, and pyrophosphate) is found in soft-tissue pathological calcifications (e.g. heart-valve calcifications of uremic patients).[15–18] In medicine, ACP is sometimes used in calcium phosphate cements.[31–33] Bioactive composites of ACP with polymers have properties suitable for use in dentistry[79–82] and surgery.[83–86]

CDHA (calcium-deficient hydroxyapatite) can be easily prepared by the simultaneous addition of calcium- and phosphate-containing solutions into boiling water, followed by boiling the suspension for several hours. During this time, initially precipitated OCP or ACP (this depends on the solution pH value) are transformed into CDHA. On heating above 700 °C, dry CDHA with Ca/P = 1.5:1 will convert into β-TCP and that with 1.5:1 < Ca/P < 1.67:1 will convert into a mixture of HA and β-TCP (the above-mentioned biphasic calcium phosphate, BCP).[59–65]

Because of its nonstoichiometric character, CDHA always contains other ions. The extent depends on the counterions of the chemicals used for preparation (e.g. Na^+, Cl^-). There have been no direct determinations of the structures of CDHA and the unit cell parameters are uncertain. As a first approximation, CDHA may be considered as HA with some ions missing.[87] According to the chemical formula of CDHA (Table 2), there are vacant calcium ion sites (mainly Ca2 sites,[88, 89] see HA below) and hydroxide ion sites in the crystal structure of this compound. However, little is known about the vacancies of phosphate ions: in CDHA, part of the phosphate ions is either protonated or substituted by other ions (e.g. carbonate).

Unsubstituted CDHA (i.e. containing calcium, phosphate, hydrogenphosphate, and hydroxide ions only) does not exist in biological systems; it occurs only with ionic substitutions: Na^+, K^+, Mg^{2+}, Sr^{2+} for Ca^{2+}; carbonate for phosphate; fluoride, chloride, and carbonate for hydroxide, and some water, form the so-called "biological apatite" or dahllite—the main inorganic component of animal and human normal and pathological calcifications.[15, 16] Therefore, CDHA is a very promising compound for the manufacture of artificial bone substitutes.

HA (hydroxyapatite, $Ca_{10}(PO_4)_6(OH)_2$) is the most stable and least soluble of all calcium orthophosphates (Table 2). Pure HA crystallizes in the monoclinic space group $P2_1/b$. However, at temperatures above 250 °C, there is a monoclinic to hexagonal phase transition in HA[72, 73] (space group $P6_3/m$).[90, 91] Some impurities, like partial substitution of hydroxide by fluoride or chloride ions, stabilize the hexagonal structure of HA at ambient temperature. For this reason, the very rare single crystals of natural HA always exhibit a hexagonal space group.

HA can be prepared in aqueous solutions by mixing exactly stoichiometric quantities of calcium- and phosphate-containing solutions at pH > 9, followed by boiling for several days under a CO_2-free atmosphere, filtration, and drying. Microcrystalline samples of HA can also be prepared by solid-state reactions of other calcium phosphates (e.g. MCPM, DCPA, DCPD, OCP) with CaO, $Ca(OH)_2$, or $CaCO_3$ at temperatures

above 1200 °C, in an atmosphere of equal volumes of water and nitrogen. Single crystals of HA can be prepared by hydrothermal synthesis.[72, 73] A water-free synthesis can be performed in ethanol from $Ca(OEt)_2$ and H_3PO_4.[92, 93]

Pure HA never occurs in biological systems. However, becuase of the chemical similarities to bone and teeth mineral (Table 1), HA is widely used as a coating for orthopedic (e.g. hip-joint prosthesis) and dental implants (reviewed in refs. [94, 95]), and a calcium phosphate cement with HA has also been developed.[29] Because of the great similarity to bone mineral, HA is also used in liquid chromatography of proteins and other biological compounds.[96–101]

TTCP (tetracalcium phosphate $Ca_4(PO_4)_2O$) is the most basic calcium orthophosphate. However, its solubility in water is higher than that of HA (Table 2). TTCP cannot be precipitated from aqueous solutions, and thus can only be prepared by a solid-state reaction above 1300 °C, for example, by heating homogenized, equimolar quantities of DCPA and $CaCO_3$ in dry air, or in a stream of dry nitrogen [Eq. (2)]:[72, 73]

$$2\,CaHPO_4 + 2\,CaCO_3 \rightarrow Ca_4(PO_4)O + 2\,CO_2 + H_2O \quad (2)$$

TTCP is not very stable in aqueous solutions; it slowly hydrolyses to HA and calcium hydroxide.[72, 73] Consequently, TTCP is never found in biological calcifications. In medicine, TTCP is widely used for the preparation of various self-setting calcium phosphate cements.[27, 29–31, 39, 41, 102–104]

3. Biomineralization and Biological Hard Tissues

Biological mineralization (biomineralization) is the process of in vivo formation of inorganic minerals. As shown in Table 1 and discussed above, in the human body all normal and most pathological calcifications consist of calcium phosphates. Other minerals such as calcium carbonate (found in mollusk shells, algae, fish, ascidians, and plants), calcium oxalate (present in plants), $CaSO_4$ (jellyfish), $SrSO_4$ (single-celled sea organisms of the genus *acantharia*), and $BaSO_4$ (algae), silicon dioxide (marine algae and plants), and iron oxide (in bacteria, limpets, chitons, or mollusk teeth) are also found in biological systems,[1, 4, 5] but that is another story. Only the chemical and structural peculiarities of calcified tissues consisting of calcium phosphates will be discussed here.

According to Weiner and Wagner, "the term bone refers to a family of materials, all of which are built up of mineralized collagen fibrils".[105, 106] This family of materials also includes dentin (the material that constitutes the interior of a tooth), cementum (the thin layer between the root of a tooth and the jaw), and mineralized tendons.[105, 107] Let us start with the "real" bones.

3.1. Bone

Bone is the major calcification present in a human body.[1] It serves as structural (mechanical) support for the body and as the major reservoir of calcium and phosphate ions necessary for a wide variety of metabolic functions. From the chemical point of view, bone is a composite material (Table 1) of calcium phosphate and collagen. The physiological fluids present in bone act as plasticizers. Porosity is an important property of bone, as it allows the body fluids and cells to access the various regions of the osseous tissue while also influencing the mechanical anisotropy.[1, 5, 15–17, 19–21, 105, 108–112]

Usually bone is composed of a relatively dense outer layer (*Corticalis*; the cortical or compact bone) surrounding a less dense, porous tissue (*Spongiosa*; cancellous bone), which is filled with a gel-like tissue known as bone marrow (Figure 3). Bone is a highly complex material that exhibits a strongly hierarchical structure on different length scales (see refs. [1, 5, 105, 108–112] for detailed discussions).

Figure 3. A noncalcined cancellous bone (femoral head) showing the transition from a more compact outer layer (*corticalis*) to a more porous interior (*spongiosa*).

Microscopically, the constituent building blocks of bone are mineralized collagen fibrils of 80–100 nm thickness and a length of a few to tens of microns (Figure 4). These fibrils are composites of biological apatite (i.e. CDHA with ionic substitutions) and molecules of type I collagen. The crystals of biological apatite in bone are always plateletlike (elongated along the crystallographic *c* axis) and very thin; 2–4 nm (in other words, just a few unit cells thick!—see Table 1). The crystals insert themselves in a parallel fashion into the collagen fibrils, while the latter are formed by self-assembly of collagen triple helices.[105] Recently, this lowest level of hierarchical organization of bone has been successfully simulated by HA precipitation on amphiphilic peptide nanofibers.[113] However, the interface between collagen and crystals of biological apatite is still poorly understood. It is not known why the crystals of biological apatite are platelet-shaped.[1, 5, 105, 108–112]

In general, a sequence of temporal events can be recognized during bone formation. The first stage involves the synthesis and extracellular assembly of the collagen I matrix framework of fibrils, followed by its mineralization. The

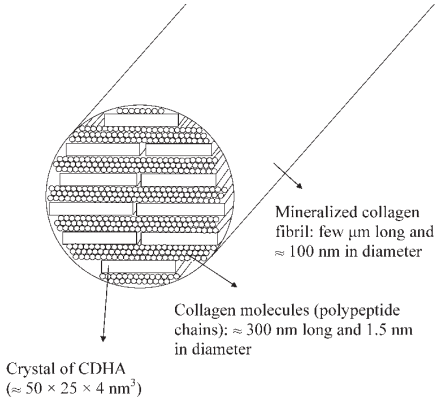

Figure 4. Schematic drawing of the mineralized collagen fibrils that are the basic constituents of bone. Platelet-shaped nanocrystals of CDHA are incorporated in a parallel way between collagen molecules, with the crystallographic *c* axis parallel to the fiber axis.

crystals of biological apatite grow with a specific crystalline orientation—the *c* axes of the crystals are roughly parallel to the long axes of the collagen fibrils within which they are deposited.[5, 105, 107] The same is true for dentin and enamel,[114, 115] as well as for more primitive living organisms. For example, in the shell of the mollusk *Lingula unguis* which consists of CDHA, the crystal *c* axes are oriented parallel to the β-chitin fibrils.[116] Therefore, the orientation of CDHA crystals parallel to the long axes of an organic framework could be a general feature of the calcium phosphate biomineralization process.

Unlike other mineralized tissues, bone continuously undergoes a so-called "remodeling" process as it is resorbed by specialized cells called osteoclasts and formed by another type of cells called osteoblasts in a delicate equilibrium. Osteoporosis is the condition in which bone resorption dominates, and in osteopetrosis, the reverse process is dominant. That is why mature bone consists of a very complex assembly of bone "patches", each of which has a slightly different structure and a different age.[1, 5, 105, 107–112]

There is no general agreement on the chemical mechanism of bone formation. It is clear that the inorganic part of bone consists of biological apatite, that is, CDHA in which some ions have been replaced but (surprisingly!) without detectable amounts of hydroxide ions.[117–119] However, various in vitro experiments on the precipitation of CDHA and HA revealed that none of these compounds directly precipitates from supersaturated aqueous solutions containing calcium and phosphate ions: some intermediate phases (so-called "precursors") are always involved.[15–17, 48–53, 67–71] Three compounds (DCPD, ACP, and OCP) are possible precursors to CDHA and HA precipitation in vitro. Therefore, the same compounds are suggested as the precursors to in vivo bone formation. Evidently, the precursor phase of bone is of a transient nature, which complicates its detection, especially in vivo. In 1966, Brown et al. suggested that OCP is the original precipitate on which biological apatite nucleates in the following step.[120] This idea was extended in their further investigations.[121–124] By use of high-resolution transmission electron microscopy, this hypothesis was supported: computer-simulated lattice images of the "central dark line" in mineralized tissues revealed that it consisted of OCP.[48–50]

Simultaneously with Brown, the research group led by Posner proposed that ACP is the initially precipitated phase of bone formation in vivo.[125–127] This conclusion was drawn from the following facts:

- When calcium orthophosphates are prepared by rapid precipitation from aqueous solutions containing calcium cations and phosphate anions at $pH > 8.5$ in vitro, the initial solid phase that appears is amorphous.
- Mature bone mineral is a mixture of ACP and poorly crystallized CDHA.
- Early bone mineral has a lower crystallinity than mature bone,[125–133] which suggests that after being formed the crystals of bone mineral undergo some transformations during maturation.

For obvious reasons, there is only indirect evidence for the in vivo crystal growth of bone mineral. Studies of animal bones of different ages showed that the X-ray diffraction peaks become sharper with increasing age, that is, the crystallinity and/or the domain size increase. This change occurs anisotropically, that is, it is more pronounced in the crystallographic *a* axis [(310) reflections] than the *c* axis [(002) reflections].[134, 135] In addition to this, other changes, such as an increase of calcium content and a decrease of HPO_4^{2-} occur in bone mineral with age.[136, 137] Both crystal size and carbonate content increase during aging in rats and cows.[137] From a chemical point of view, these changes indicate a slow transformation of a poorly crystallized CDHA into a better crystallized HA.

There is a current debate on the question of whether bone formation is an active or a passive process. As an "active process", one describes the assembly of calcium phosphate nanocrystals within a spatially confined compartment of an osteoblast, that is, within a matrix vesicle. These structures have been found by transmission electron microscopy for bone and tooth formation.[138–140] The term "passive process" comes from the observation that blood serum is supersaturated with respect to calcium phosphate precipitation,[141] therefore mineralization should occur spontaneously at a suitable nucleus (i.e. on a collagen fibril). The collagen fibrils have a specific structure with a periodicity of 67 nm and 35–40 nm gaps or holes between the ends of the collagen molecules, where bone mineral is incorporated in the mineralized fibril. A nucleation within these holes would lead to discrete crystals with a size related to the nucleating cavity in the collagen fibril. It was proposed that the temporary absence of specific inhibitors leads to precipitation and thereby regulates this physicochemical bone formation.[142–144] The question of whether cells do actively form and deposit bone mineral or whether a systemic regulation of inhibitors controls bone formation is still open.[145] The truth probably lies somewhere in between, that is, calcium phosphate nanocrystals are formed within cells from a supersaturated medium and excreted near the collagen fibers where they are finally deposited.

3.2. Teeth

Teeth are the second major normal calcification present in mammals.[1] The structure of teeth is even more complicated than that of bone (Figure 5). For example, unlike bone, teeth consist of at least two different biominerals: enamel (outside) and dentin (interior). As shown in Table 1, dentin and bone have many similarities, and in most aspects they can be regarded as being essentially the same material.[1, 72, 73, 105, 107–112, 136] Therefore, most statements made above for bone are also valid for dentin.

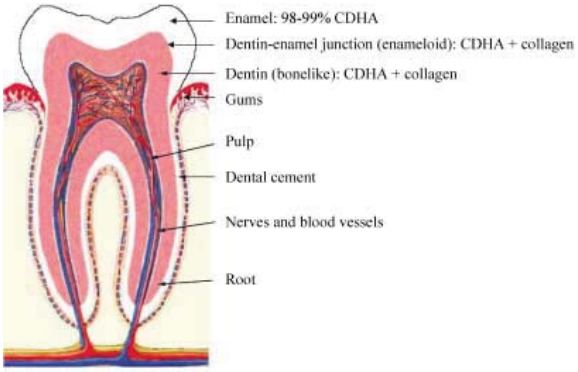

Figure 5. Schematic picture of a tooth and its local chemical composition.

Tooth enamel contains crystals of biological apatite that are much larger than those of bone and dentin (Table 1). In addition, its organic phase does not contain collagen. At the interface between enamel and dentin, there is an "enameloid" phase; a hard tissue that contains enamel-like crystals of biological apatite and collagen fibrils.[1]

Enamel and enameloid consist of biological apatite crystals that are remarkably different from the other mineralized tissues in humans and vertebrates. In enamel, needlelike crystal rods are tens of microns long (up to 100 μm) but sometimes only 50 nm wide,[146–150] which is much larger than the mineral crystals of dentin and bone (Table 1), but nevertheless consist of carbonated CDHA.[151–153] On the surface, there is also some fluoride content in place of hydroxide ions[154] although the overall content of fluoride ions in enamel is small (about 0.01 wt %;[16] see also Table 1). Note that fluoroapatite is not found in enamel.[1]

The enamel crystals are generally organized into parallel arrays under strict biological control. This structure can be deduced from the observation that, at every stage, the parallel arrays are well-ordered and that the crystal rods all have a remarkably uniform cross section (Figure 6).[146–148] The first detectable crystals in enamel formation are flat, thin ribbons,[146–148] that were reported to be OCP,[109, 155–157] β-$(Ca,Mg)_3(PO_4)_2$,[156] or DCPD.[117, 119] During maturation of the enamel, the mineral content increases from initially 45 wt % to 98–99 wt %,[117] accompanied by widening and thickening of the crystal rods.[117, 119, 158, 159] Simultaneously, the

Figure 6. Scanning electron micrograph of the forming enamel on a continuously growing rat incisor, which shows ordered rods of calcium phosphates. Scale bar: 10 μm (taken from ref. [1] with permission).

Ca/P ratio increases[158, 159] and the carbonate content decreases,[160–162] which finally results in the most highly mineralized and hardest skeletal tissue.

Enamel crystals show the (100) face at the sides and presumably the (001) face at the ends,[163, 164] as usual for HA. A "central dark line" is observed by TEM in the centers of enamel crystals (also observed in bone and dentin), which consists of OCP.[48–51] As described above for bone, X-ray diffraction shows that the crystals of "younger" dentin are less ordered than those of more mature dentin.[136] Therefore, maturation of dentin is a slow transformation of a poorly crystallized CDHA into a better crystallized HA.

The development of individual enamel and dentin crystals was studied by high-resolution transmission electron microscopy.[165–167] Both processes appear to be roughly comparable and were described in a four-step process. The first two steps include the initial nucleation and formation of nanometer-sized particles of CDHA. They are followed by formation of ribbonlike crystals, which until recently was considered to be the first step of biological crystal formation in the tooth.[165–167] These complicated processes, starting with the heterogeneous nucleation of inorganic calcium phosphate on an organic extracellular matrix, are controlled in both tissues by the organic matrix and are under cellular control (odontoblasts and ameloblasts).[168] To complicate the process even further, regular and discrete domains of various charges or charge densities on the surface of CDHA crystals derived from the maturation stage of enamel development were recently discovered by a combination of atomic and chemical force microscopy.[169] Organic molecules (e.g. amelogenin)[169] at physiological solution pH values appear to bind on the charged surface domains of CDHA.

On the other hand, dentin and enamel share a common starting location: the dentin–enamel junction.[170–172] The steps of enamel crystal growth at the junction are a matter of current debate. Some authors claim that the enamel crystals grow epitaxially on the pre-existing dentin crystals, because of a high continuity between enamel and dentin crystals.[173–175] Others have shown that enamel crystals are formed at a given distance from the dentin surface[155–157, 176] and could either

reach dentin crystals by a subsequent growth[177] or remain distant.[176, 178] Thus, both structure and formation of the teeth appear to be more complicated than those of the bone.

A physicochemical mineralization occurs every day on our teeth. Enamel is only formed during dentinogenesis in the jaw, that is, it will never be repaired by cellular action. If it is etched, for example, by acidic food or beverages, CDHA is dissolved. Fortunately, the saliva in the mouth is supersaturated with respect to CDHA deposition (as is the blood serum), and after a while, the surface layer is restored again. This process does not involve any biological action and therefore can be classified as "passive mineralization" (see also the discussion above on bone formation). Replacement of some hydroxide ions with fluoride ions (which leads to fluorohydroxyapatite) lowers the solubility and therefore improves the acid resistance.[154]

3.3. Cartilage

Cartilage is usually (but not exclusively) part of the endoskeleton of animals[1, 179] and exists both in mineralized and unmineralized forms. Only vertebrates develop mineralized cartilage, in some cases in the central portions of the vertebra and close to the surface of jaws. Except for pathological cases, the mineralization of cartilage occurs in two situations in the body: First, during bone formation in the endochondral plate (in almost all vertebrates) and second, as final mineralized product (only in sharks and certain other fishes[180]).[1]

Mineralized cartilage consists of the unmineralized cartilage plus crystals of CDHA, as well as considerable amounts of amino acids, phosphoserine, and other biological compounds. The molecular organization of macromolecules of cartilage and CDHA crystals is still not fully understood. Mineralized cartilage and bone coexist in close proximity in the endochondral plate during bone formation. They have similar macromolecular constituents, and both contain CDHA.[1] However, the shape of the CDHA crystals in mineralized cartilage, in general, resembles that in enamel: the crystals were found to be needlelike (CDHA crystals of bone are platelike),[1, 105, 108–112] but much shorter (25–75 nm[181] or 50–160 nm[182]) than those of enamel (up to 100 μm[146–150]). The average thickness of the CDHA crystals in mineralized cartilage was reported as 5–7.5 nm[181] and 1.8 nm.[182]

The process of cartilage mineralization has been well-described elsewhere.[183–185] Before the crystal formation, the organic matrix (consisting of proteoglycans, type II collagen and water)[1] first takes up calcium and then phosphate.[185] The first crystals of CDHA, those formed in cartilage, were needlelike and located inside cellular matrix vesicles.[183, 184] After growth within the vesicles, the crystals extend out of these containers into the surrounding organic matrix. They aggregate into clusters of randomly oriented crystals. In a second step, these clusters further aggregate to form the mature mineralized-cartilage structure with a random arrangement of crystals.[181] Physicochemical investigations of the crystals revealed their very poor crystallinity and the presence of significant amounts of nonapatitic calcium phosphates. The concentration of such nonapatitic phosphates was found to increase during the early stages of cartilage mineralization but then decreased as the mineral content steadily rose, until full mineralization was achieved.[186] Therefore, the CDHA crystals in the vesicles act as centers of cartilage mineralization. However, a detailed understanding of the mechanisms of crystal nucleation and growth in these vesicles is not yet available.[1]

3.4. Shells

Rarely, calcium phosphates are encountered in mollusk shells (that in most cases consist of calcium carbonate).[187, 188] When biomineralization was "invented" by nature about 570 million years ago, there were both mollusks with calcium carbonate and calcium phosphate shells. Over time, the ones with calcium phosphate shells mostly disappeared (so-called "problematica"), and today the overwhelming majority of mollusk has shells of calcium carbonate.[1] Figure 7 shows fossilized shells of the species *Lingula* that consist of calcium phosphate (apatite).[116]

Figure 7. Fossilized shells of the brachiopod *Lingula* from the Lower Triassic, consisting of calcium phosphate (taken from http://inyo.topcities.com/ef/lingula.html with permission).

4. Pathological Crystallization of Calcium Phosphates

Unwanted deposition of calcium phosphates in the body can lead to severe diseases. Calcium phosphate depositions are responsible, among other things, for urinary stones,[15, 189, 190] atherosclerosis,[141, 191–193] dental calculus,[45, 46] calcification of artificial heart valves,[194–198] and calcified menisci ("chondrocalcinosis").[199, 200] Figure 8 shows an example of atherosclerotic depositions of calcium phosphate (together with cholesterol) that was isolated from arteries.[193, 201] Blockage of arteries by such deposits is the major cause of death in developed countries.

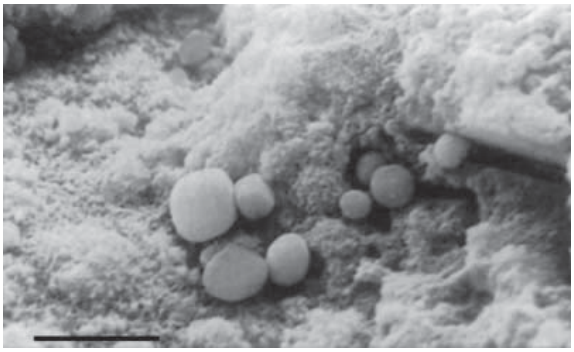

Figure 8. Spherical calcium phosphate particles isolated from an atherosclerotic lesion. Scale bar: 4 μm (taken from ref. [193] with permission).

As many body fluids (blood, saliva) are supersaturated with respect to HA precipitation,[141] we may conclude that calcification is thermodynamically feasible but kinetically hindered in most parts of the body. Therefore, suitable inhibitory mechanisms must be at work to prevent an unwanted mineralization in the body. The mechanisms of this inhibition are a topic of current research in molecular medicine, as it can be concluded that disruptions of this inhibition are probably the cause of pathological calcifications. In addition, the fine-tuned equilibrium of bone resorption and formation may be based on such processes. For instance, in mice in which the genes that are responsible for the production of the specific blood proteins (fetuine,[142, 144] matrix Gla protein[143, 202]) were knocked out, uncontrolled calcification in the arteries occurs. Obviously, these proteins serve as inhibitors of calcium phosphate precipitation by suitable complexation of the dissolved ions or by effectively preventing formed nuclei from further growth by preferential adsorption.[203–205]

On the other hand, some mechanisms have been identified that enhance crystallization.[141] Currently discussed, especially for the case of atherosclerosis, are:

- the heterogeneous nucleation of calcium phosphates on the membranes of dead cells that contain phospholipids (phosphate groups act as nucleators),[192, 195]
- nucleation by antibodies that are specific for cholesterol,[205, 206] and
- cellular action of osteoblast-like cells (so-called pericytes) within arteries that form bonelike tissue.[207]

For the case of atherosclerosis, obviously a number of effects are responsible for the pathological calcification; these range from purely physicochemical effects (supersaturation)[141] over biologically induced nucleation to the biologically controlled deposition of calcium phosphates by specialized cells.[141]

Similar effects exist during the calcification of artificial heart valves. The replacement of heart valves by implants of either biological (porcine heart valves) or synthetic origin is now a common procedure in cardiosurgery (about 150000 are implanted every year worldwide).[196] However, the implanted devices tend to calcify after implantation (in some cases even after a few months), that is, they become stiff because of deposition of calcium phosphate. The origin of this behavior is not yet clear but, at least with heart valves of biological origin, a nucleation by membranes of dead cells (phospholipids) appears likely.[194–198]

5. Calcium Phosphates as Biomaterials

The treatment of injuries or diseases often requires surgical action. For the past 50 years, biomaterials have increasingly been applied to improve surgical procedures or to restore lost body functions. Bone fractures are usually treated with metallic wires, nails, screws, and plates, joints are replaced by artificial endoprostheses (hip or knee), and lost teeth are replaced by metallic implants in the jaw, to name a few examples. As soon as foreign materials come into internal contact with the body, the question of biocompatibility becomes paramount, as any adverse effect (namely toxicity, allergy, inflammation, corrosion, and mechanical failure) must be strictly avoided. The search for optimally designed biomaterials is still ongoing as a joint effort of physicians, engineers, chemists, and physicists.[15, 194, 208–213]

Calcium phosphates generally have an excellent biocompatibility, that is, they are well-accepted by the body and integrate well, for example, into bone upon implantation. This is because of their almost ubiquitous presence in the body in either the dissolved or solid form. Consequently, they have found important applications as biomaterials, particularly for hard-tissue regeneration.[21, 47, 66, 214–221]

In the bulk form, calcium phosphates are used as artificial bone-substitution material for surgical treatment of bone defects by orthopedic surgeons and maxillofacial surgeons.[15, 16, 219, 222] A bone defect that is caused, for example, by tumor extraction, complicated fracture, or inflammation must be filled with a suitable material to permit growth of new bone into this defect. Otherwise, ingrowth of fibrous tissue would prevent bone formation within the defect. Because the ideal substitute (the "golden standard"), a patient's own spongious bone from the *Iliac crest* (hip) is usually not available in sufficient quantities, and as materials of biological origin are critically discussed because of possible infections or immune reactions, the need for a fully synthetic material is evident. Today, many different calcium phosphate ceramics are on the market for the treatment of bone defects (see, for example, refs. [15, 16, 219, 222] for overviews).

Chemically, synthetic bone-substitution materials are usually based on HA, β-TCP, or BCP (i.e. a composite of HA and β-TCP).[15, 16, 219, 222, 223] The requirements for an ideal substitute are usually:

- a porosity with a pore diameter of some 100 μm size (to permit ingrowth of bone cells; see Figures 2 and 3),
- a biodegradation rate comparable to the formation of bone tissue (i.e. between a few months and about two years), and
- a sufficient mechanical stability.[15, 16, 219, 222]

HA is more stable than α- and β-TCP under physiological conditions, as it has a lower solubility and slower resorption kinetics.[15, 16, 219, 222] Implants of calcined HA of high crystallinity are present in a defect even years after implantation in a virtually unchanged form, therefore β-

TCP[218] or BCP[21, 61, 63, 64] ceramics are favored today. An ideal material should be degraded inside the defect simultaneously with the formation of a new bone, that is, the full restoration of the defect with biological material is desired. Figure 9 shows three examples of calcium phosphate-based bone-substitution materials of different origins. Implant porosity is a very important property to allow cell invasion and bone ingrowth.

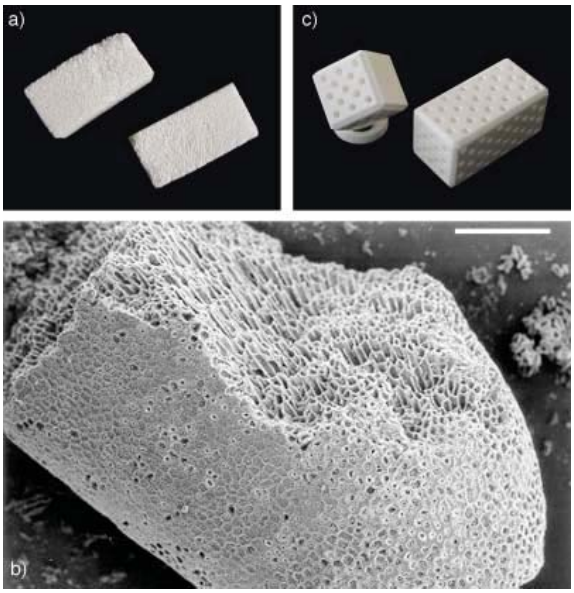

Figure 9. Examples of porous calcium phosphate-based bone-substitution materials: a) Cerabone (hydroxyapatite) from spongious calcined bovine bone (about $3 \times 1 \times 1$ cm^3); b) Algipore (hydroxyapatite) from hydrothermal processing of calcium carbonate-containing algae with ammonium phosphate. Scale bar: 100 μm; c) Cerasorb (synthetic phase-pure β-TCP) with CNC (computer numerical control)-drilled holes (about $1 \times 1 \times 2$ cm^3).

A new concept in the treatment of bone defects was introduced with bone cements based on calcium phosphates, which harden inside the defect. Although different formulations are on the market (see the discussion of the different calcium phosphates above), they usually consist of solid calcium phosphates that are mixed with a solution to induce the precipitation of a CDHA-like phase [Eq. (3), not stoichiometrically balanced]:[66, 102–104, 211, 212]

$$Ca(H_2PO_4)\cdot 2H_2O\,(s) + \beta\text{-}Ca_3(PO_4)_2\,(s) + CaCO_3\,(s) + Na_2HPO_4\,(aq) \rightarrow Ca_{8.8}(HPO_4)_{0.7}(PO_4)_{4.5}(CO_3)_{0.7}(OH)_{1.3}\,(s) \quad (3)$$

The advantage of this procedure is that the cement adapts better to the defect geometry than ceramic materials that are implanted as solids. The structure and composition of the hardened calcium phosphate is close to that of bone mineral; therefore, a facilitated resorption is observed.[66]

Calcium phosphate coatings on metals are often applied in medicine. Metallic implants are encountered in endoprostheses (total hip-joint replacements) and artificial tooth sockets. The requirement for mechanical stability necessitates the use of a metallic body for such devices. As metals usually do not undergo bone bonding, that is, they do not form a mechanically stable bond between implant and bone tissue, ways have been sought to improve the mechanical contact at the interface.[194, 208, 224] One possibility is to coat the metal with calcium phosphate ceramics; these increase the roughness of the bone surface and thereby facilitate bone bonding, and may therefore serve as a "glue" between the metal and bone (Figure 10).

Figure 10. Calcium phosphates in hip endoprostheses: a ceramic ball joint (Al_2O_3), a calcium-phosphate coated endoprosthesis ("cementless endoprosthesis") and an uncoated endoprosthesis that must be fixed in place with PMMA bone cement.

Two methods of bone coating are currently applied: Application of molten calcium phosphate by high-temperature plasma spraying and precipitation from a supersaturated calcium phosphate solution. The first approach[94, 95, 216, 224] is very rough from a chemical point of view. Solid calcium phosphate is injected into a plasma flame and directed towards an implant that is appropriately rotated to achieve a uniform coating. This extremely fast quenching leads to the formation of a mixture of calcium phosphates on the implant surface. Metal and calcium phosphate are strongly joined after this procedure.[94, 95, 216, 224]

The second approach involves dipping metallic implants into supersaturated calcium phosphate solutions. This method was strongly promoted by the work of Kokubo and co-workers and van Blitterswijk and co-workers, who showed that after appropriate surface etching, a stable interface evolves between metal and ceramic.[225–230] The method also permits coating of internal surfaces (difficult with plasma spraying) and the incorporation of biologically active substances, for example, proteins or antibiotics into the coating.[231] A special case is surface coating with a biomimetic defect apatite by dipping into simulated body fluid (SBF), a solution that contains the inorganic ions of human blood plasma in almost natural concentrations.[225–228, 232–235] Figure 10 shows both a calcium phosphate-coated and an uncoated hip endoprosthesis. The latter has to be fixed in the femur bone by a suitable bone cement based on poly(me-

thylmethacrylate) (PMMA). Note that this polymer is not biodegradable and remains in the operation site.[224, 236]

The same principles are valid for tooth implant systems that are fixed into the jawbone, onto which artificial teeth are attached. In general, the mechanical contact between implant and bone is crucial, as considerable forces have to be withstood. Coating of such dental implants with calcium phosphates (usually by plasma spraying) leads to better and faster bone attachment. Figure 11 shows such a plasma-spray-coated tooth implant in low and high magnification. Finally, Figure 12 shows the surface of a nickel-titanium shape-memory alloy (NiTi, "Nitinol") that was coated with calcium phosphate from solution to improve its biocompatibility.[237]

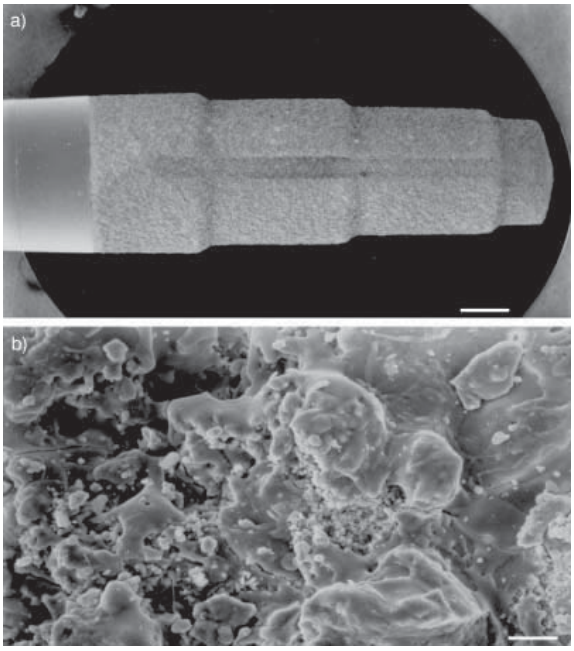

Figure 11. Dental implants (by Friadent) coated with calcium phosphate by a plasma-spray process. a: $\times 10$, b: $\times 1000$. Note the irregular, rough structure of the deposited calcium phosphate at the higher magnification. Scale bars 1 mm and 10 μm, respectively.

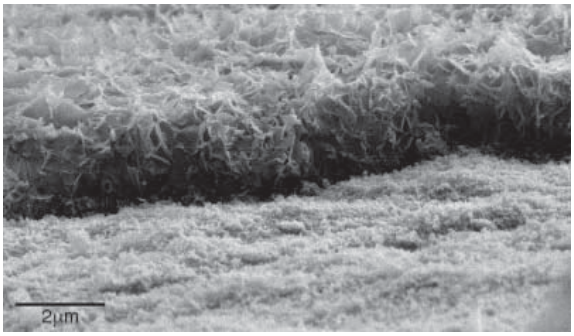

Figure 12. The surface of a nickel–titanium shape-memory alloy ("Nitinol") that was coated with a calcium phosphate layer by dipping into an supersaturated calcium phosphate solution. The front part shows the etched metal surface from which the calcium phosphate layer has been mechanically removed. Scale bar: 2 μm.

6. Biomimetic Crystallization of Calcium Phosphates

Nature's ability to assemble inorganic compounds into the biological structures (shells, spicules, teeth, bone, skeletons) is still not reproducible by synthetic procedures. Because of its potential benefits for materials science, research groups around the world are increasingly addressing the question of biomineralization. When considering calcium phosphates, the demand of clinical medicine to design biocompatible implants and to treat diseases related to crystallization phenomena adds a strong practical impetus to understanding these processes. The fundamentals of biomineralization have been reviewed extensively.[1, 3–7, 238–241] We will limit ourselves to considerations of biologically inspired crystallization of calcium phosphates and present a few examples that demonstrate the current possibilities.

An approach to the preparation of biomimetic bone-substitution materials was made by Pompe et al., who crystallized HA on collagen to obtain a bonelike composite.[242] Although the ultrastructure of bone could not be realized, such collagen–HA tapes are currently under investigation for clinical use. Note that the final step to make bone out of artificial implants is up to the body's own remodeling function. Ozin et al. precipitated HA in the presence of surfactants, to obtain a biomimetic lamellar product.[243] Stupp et al. have prepared so-called "organoapatites" with a bonelike crystallinity by precipitation of calcium phosphate in the presence of organic polyelectrolytes.[214, 217, 244, 245] Kokubo and co-workers and van Blitterswijk and co-workers were successful in coating different substrates with a bonelike apatite layer (see refs. [229, 234] and those given above on coated metal prostheses). We have recently prepared bulk samples of bonelike apatite and composites of it with biodegradable polymers.[84–86, 246]

Nancollas and co-workers invented the "Constant-Composition Technique" to monitor and control the external conditions (mainly solution pH value and concentrations of participating ions) during a crystallization experiment.[22, 247] Generally, during precipitation of calcium phosphates from a neutral solution, the pH value decreases because of the release of protons that were formerly bound to hydrogen phosphate or dihydrogen phosphate [Eq. (4)].

$$5\,Ca^{2+}(aq) + 3\,HPO_4^{2-}(aq) + 5\,H_2O(l) \rightarrow Ca_5(PO_4)_3OH(s) + 4\,H_3O^+(aq) \quad (4)$$

One of the main differences between chemical and biological crystallization is the rate of precipitation. Usually in chemistry, precipitation occurs fast whereas in biology the crystals need days, weeks, or months to grow. A suitable simulation of this process, especially in the presence of (bio)organic additives, must therefore slow down the crystallization. This can be achieved by separating the two components with a suitable membrane or medium that acts as a diffusion barrier (a double-diffusion technique). If this medium itself contains some biomimetic functional groups, it can have a templating influence on the growing crystals. Work along this line has been carried out by Iijima et al.

(collagen matrix from bovine achilles tendon,[248] and membranes in the presence of bovine[249] and murine[250] amelogenins), Kniep and co-workers (matrix of denaturated collagen),[154, 251, 252] Epple and co-workers (matrix of microporous polyglycolide),[253–256] Falini et al. (matrix of collagen),[257] and Stupp and co-workers (carbon-coated TEM grid).[113] Work on the crystallization from SBF under static and dynamic conditions to yield bonelike apatite was also reported recently by Vallet-Regi and co-workers[258, 259] and by Epple and co-workers.[256, 260]

Interactions between collagen and growing fluoroapatite crystals are responsible for a fractal growth of fluoroapatite into dumbbell shapes that finally close to give spheres.[154, 251, 252] Figure 13 shows this special morphology.

Figure 13. A biomimetically grown aggregate of fluoroapatite that was crystallized in a gelatin matrix. The crystal shape can be explained and simulated by a fractal growth mechanism. Scale bar: 10 μm (taken from ref. [252] with permission).

By combining the constant-composition technique with the double-diffusion setup, we were able to identify different crystal morphologies of fluoroapatite as functions of overall concentration (i.e. supersaturation), pH value, and fluoride ion concentration.[254, 255] Figure 14 shows a uniform crystal population that was prepared by this method.

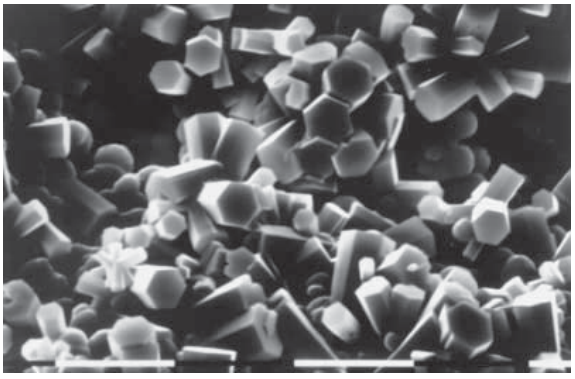

Figure 14. Hexagonal fluoroapatite crystals that were grown by a double-diffusion technique under controlled conditions (pH 7.4, 37 °C, constant ion concentrations, 7 days). Note the well-shaped crystals and their uniform size and morphology. Scale bar: 10 μm.

7. Summary and Outlook

Although it may appear surprising to the nonspecialist, there are still many open questions within the area of calcium phosphate chemistry. The basic questions concerning crystallography, thermodynamics, and phase relationships have been answered. Nevertheless, when it comes to the biological formation of calcium phosphates, issues including rate of crystallization, control of morphology, incorporation of foreign ions, and interaction with biomolecules remain hot topics that are not well understood even today. A better understanding of structure, formation, and dissolution of such biominerals will lead to improved biomaterials that can substitute bone and teeth. This knowledge will also help to counter widespread pathological calcifications such as atherosclerosis, stone formation, or dental calculus. Further progress of unforeseeable impact will come from modern genetics, where gene structures are currently related to hard-tissue formation.

We thank Alexander Becker, Dr. Jongsik Choi, Elena Dorozhkina, Dr. Bernd Hasse (now at DESY), Dr. Fabian Peters (now at Curasan), Carsten Schiller, Dr. Karsten Schwarz (now at Tutogen), Dr. Michael Siedler, and Drazen Tadic for their research contributions during the past years. We also thank Dr. Jörg Arnoldi (Mathys), Dr. Philip Cantzler (Friadent), Dr. Peter Seidel (Coripharm), and Prof. Gerd Willmann (Ceramtec) for providing material. We are also grateful to the Deutsche Forschungsgemeinschaft (DFG), to the Fonds der Chemischen Industrie, to the Deutscher Akademischer Austauschdienst (DAAD), and to HASYLAB at DESY (Hamburg) for generous support of our work during the past years.

Received: December 3, 2001 [A 505]

[1] H. A. Lowenstam, S. Weiner, *On Biomineralization*, Oxford University Press, New York, **1989**.
[2] K. Simkiss, K. M. Wilbur, *Cell Biology and Mineral Deposition*, Academic Press, San Diego, **1989**.
[3] L. Addadi, S. Weiner, *Angew. Chem.* **1992**, *104*, 159 – 176; *Angew. Chem. Int. Ed. Engl.* **1992**, *31*, 153 – 169.
[4] S. Mann, *J. Mater. Chem.* **1995**, *5*, 935 – 946.
[5] S. Mann, *Biomimetic Materials Chemistry*, Wiley/VCH, New York/Weinheim, **1995**.
[6] G. A. Ozin, *Acc. Chem. Res.* **1997**, *30*, 17 – 27.
[7] E. Baeuerlein, *Biomineralization*, Wiley-VCH, Weinheim, **2000**.
[8] S. Mann, *Angew. Chem.* **2000**, *112*, 3532 – 3548; *Angew. Chem. Int. Ed.* **2000**, *39*, 3392 – 3406.
[9] S. A. Davis, M. Breulmann, K. H. Rhodes, B. Zhang, S. Mann, *Chem. Mater.* **2001**, *13*, 3218 – 3226.
[10] R. C. Weast, *The CRC Handbook of Chemistry and Physics*, 66th ed., CRC, Boca Raton, FL, **1985 – 1986**.
[11] D. McConnell in *Apatite: Its Crystal Chemistry, Mineralogy, Utilization, and Biologic Occurrences*, Springer, New York, **1973**, pp. 111 – 115.
[12] P. Becker in *Fertilizer Science and Technology Series*, Marcel Dekker, New York, **1989**, pp. 6 – 20.
[13] D. K. Smith in *Hydroxyapatite and Related Materials* (Eds.: P. W. Brown, B. Constantz), CRC, Boca Raton, FL, **1994**, pp. 29 – 44.
[14] A. I. Angelov, B. V. Levin, Y. D. Chernenko in *Phosphate Ore. A Reference Book (in Russian)*, Nedra business center, Moskau, **2000**, pp. 1 – 120.
[15] R. Z. LeGeros, *Calcium Phosphates in Oral Biology and Medicine*, Karger, Basel, **1991**.

[16] R. Z. LeGeros in *Hydroxyapatite and Related Materials* (Eds.: P. W. Brown, B. Constantz), CRC, Boca Raton, FL, **1994**, pp. 3 – 28.
[17] R. Z. LeGeros, *Z. Kardiol.* **2001**, *90* (Suppl. 3), III/116 – III/125.
[18] A. Hesse, D. Heimbach, *World J. Urol.* **1999**, *17*, 308 – 315.
[19] B. M. Tracy, R. H. Doremus, *J. Biomed. Mater. Res.* **1984**, *18*, 719 – 726.
[20] G. Daculsi, R. Z. LeGeros, M. Heughebaert, I. Barbieux, *Calcif. Tissue Int.* **1990**, *46*, 20 – 27.
[21] G. Daculsi, J. M. Bouler, R. Z. LeGeros, *Int. Rev. Cytol.* **1997**, *172*, 129 – 191.
[22] P. Koutsoukos, Z. Amjad, M. B. Tomson, G. H. Nancollas, *J. Am. Chem. Soc.* **1980**, *102*, 1553 – 1557.
[23] A. A. Mirtchi, J. Lemaitre, N. Terao, *Biomaterials* **1989**, *10*, 475 – 480.
[24] A. A. Mirtchi, J. Lemaitre, E. Munting, *Biomaterials* **1989**, *10*, 634 – 638.
[25] O. Bermúdez, M. G. Boltong, F. C. M. Driessens, J. A. Planell, *J. Mater. Sci. Mater. Med.* **1994**, *5*, 67 – 71.
[26] O. Bermúdez, M. G. Boltong, F. C. M. Driessens, J. A. Planell, *J. Mater. Sci. Mater. Med.* **1994**, *5*, 160 – 163.
[27] F. C. M. Driessens, M. G. Boltong, O. Bermúdez, J. A. Planell, M. P. Ginebra, E. Fernández, *J. Mater. Sci. Mater. Med.* **1994**, *5*, 164 – 170.
[28] M. Windholz, *The Merck Index: An Encyclopedia of Chemicals, Drugs, and Biologicals*, 10th ed., Merck, Rahway, NJ, **1983**.
[29] M. Otsuka, Y. Matsuda, Y. Suwa, J. L. Fox, W. I. Higuchi, *Chem. Pharm. Bull. (Tokyo)* **1993**, *41*, 2055 – 2057.
[30] C. Hamanishi, K. Kitamoto, K. Ohura, S. Tanaka, Y. Doi, *J. Biomed. Mater. Res.* **1996**, *32*, 383 – 389.
[31] K. Kurashina, H. Kurita, M. Hirano, A. Kotani, C. P. Klein, K. de Groot, *Biomaterials* **1997**, *18*, 539 – 543.
[32] F. C. M. Driessens, J. A. Planell, M. G. Boltong, I. Khairoun, M. P. Ginebra, *Proc. Inst. Mech. Eng. Part H* **1998**, *212*, 427 – 435.
[33] S. Takagi, L. C. Chow, K. Ishikawa, *Biomaterials* **1998**, *19*, 1593 – 1599.
[34] H. Yamamoto, S. Niwa, M. Hori, T. Hattori, K. Sawai, S. Aoki, M. Hirano, H. Takeuchi, *Biomaterials* **1998**, *19*, 1587 – 1591.
[35] J. J. Crall, J. M. Bjerga, *J. Oral Pathol.* **1987**, *16*, 488 – 491.
[36] J. S. Wefel, J. D. Harless, *J. Dent. Res.* **1987**, *66*, 1640 – 1643.
[37] P. M. Hoppenbrouwers, E. Groenendijk, N. R. Tewarie, F. C. M. Driessens, *J. Dent. Res.* **1988**, *67*, 1254 – 1256.
[38] A. Gaffar, J. Blake-Haskins, J. Mellberg, *Int. Dent. J.* **1993**, *43* (Suppl. 1), 81 – 88.
[39] Y. Fukase, E. D. Eanes, S. Takagi, l. C. Chow, W. E. Brown, *J. Dent. Res.* **1990**, *69*, 1852 – 1855.
[40] K. S. TenHuisen, P. W. Brown, *J. Dent. Res.* **1994**, *73*, 598 – 606.
[41] O. Bermúdez, M. G. Boltong, F. C. M. Driessens, J. A. Planell, *J. Mater. Sci. Mater. Med.* **1994**, *5*, 144 – 146.
[42] E. Fernandez, M. P. Ginebra, M. G. Boltong, F. C. M. Driessens, J. Ginebra, E. A. de Maeyer, V. M. Verbeeck, J. A. Planell, *J. Biomed. Mater. Res.* **1996**, *32*, 367 – 374.
[43] E. Fernandez, F. J. Gil, S. M. Best, M. P. Ginebra, F. C. M. Driessens, J. A. Planell, *J. Biomed. Mater. Res.* **1998**, *42*, 403 – 406.
[44] E. Fernandez, F. J. Gil, S. M. Best, M. P. Ginebra, F. C. M. Driessens, J. A. Planell, *J. Biomed. Mater. Res.* **1998**, *41*, 560 – 567.
[45] R. Z. LeGeros, *J. Dent. Res.* **1974**, *53*, 45 – 50.
[46] H. Schroeder, *Formation and Inhibition of Dental Calculus*, Hubert, Vienna, **1969**.
[47] L. C. Chow, E. D. Eanes, *Octacalcium Phosphate*, *Vol. 18*, Karger, Basel, **2001**.
[48] D. G. A. Nelson, G. J. Wood, J. C. Barry, *Ultramicroscopy* **1986**, *19*, 253 – 266.
[49] M. Iijima, D. G. A. Nelson, Y. Pan, A. T. Kreinbrink, M. Adachi, T. Goto, Y. Moriwaki, *Calcif. Tissue Int.* **1996**, *59*, 377 – 384.
[50] P. S. Bodier-Houllé, P. J. C. Voegel, F. J. G. Cuisinier, *Acta Crystallogr. Sect. D* **1998**, *54*, 1377 – 1381.
[51] T. Aoba, H. Komatsu, Y. Shimazu, H. Yagishita, Y. Taya, *Connect. Tissue Res.* **1998**, *38*, 129 – 145.
[52] B. B. Tomazic, W. E. Brown, F. J. Shoen, *J. Biomed. Mater. Res.* **1994**, *28*, 35 – 47.
[53] G. H. Nancollas, W. Wu, *J. Crystal Growth* **2000**, *211*, 137 – 142.
[54] T. Kodaka, K. Debari, S. Higashi, *J. Electron Microsc. (Tokyo)* **1988**, *37*, 73 – 80.
[55] A. A. Mirtchi, J. Lemaitre, E. Munting, *Biomaterials* **1990**, *11*, 83 – 88.
[56] A. A. Mirtchi, J. Lemaitre, E. Munting, *Biomaterials* **1991**, *12*, 505 – 510.
[57] J. Lemaitre, E. Munting, A. A. Mirtchi, *Rev. Stomatol. Chir. Maxillofac.* **1992**, *93*, 163 – 165.
[58] K. Ohura, M. Bohner, P. Hardouin, J. Lemaitre, G. Pasquier, B. Flautu, *J. Biomed. Mater. Res.* **1996**, *30*, 193 – 200.
[59] G. Daculsi, R. Z. LeGeros, E. Nery, K. Lynch, B. Kerebel, *J. Biomed. Mater. Res.* **1989**, *23*, 883 – 894.
[60] G. Daculsi, M. D'Arc Bagot, P. Corlieu, M. Gersdorff, *Ann. Otol. Rhinol. Laryngol.* **1992**, *101*, 669 – 674.
[61] J. M. Bouler, M. Trecant, J. Delecrin, J. Royer, N. Passuti, G. Daculsi, *J. Biomed. Mater. Res.* **1996**, *32*, 603 – 609.
[62] J. Wang, W. Chen, Y. Li, S. Fan, J. Weng, X. Zhang, *Biomaterials* **1998**, *19*, 1387 – 1392.
[63] G. Daculsi, *Biomaterials* **1998**, *19*, 1473 – 1478.
[64] G. Daculsi, P. Weiss, J. M. Bouler, O. Gauthier, F. Millot, E. Aguado, *Bone* **1999**, *25* (Suppl. 2), 59S – 61S.
[65] I. Alam, I. Asahina, K. Ohmamiuda, S. Enomoto, *J. Biomed. Mater. Res.* **2001**, *54*, 129 – 138.
[66] B. R. Constantz, I. C. Ison, M. T. Fulmer, R. D. Poser, S. T. Smith, M. VanWagoner, J. Ross, S. A. Goldstein, J. B. Jupiter, D. I. Rosenthal, *Science* **1995**, *267*, 1796 – 1799.
[67] J. D. Termine, E. D. Eanes, *Calcif. Tissue Res.* **1972**, *10*, 171 – 197.
[68] E. D. Eanes, J. D. Termine, M. U. Nylen, *Calcif. Tissue Res.* **1973**, *12*, 143 – 158.
[69] J. L. Meyer, E. D. Eanes, *Calcif. Tissue Res.* **1978**, *28*, 59 – 68.
[70] J. L. Meyer, E. D. Eanes, *Calcif. Tissue Res.* **1978**, *28*, 209 – 216.
[71] R. E. Wuthier, G. S. Rice, J. E. Wallace, R. L. Weaver, R. Z. LeGeros, E. D. Eanes, *Calcif. Tissue Int.* **1985**, *37*, 401 – 410.
[72] J. C. Elliot, *Structure and Chemistry of the Apatites and Other Calcium Orthophosphates*, Elsevier, Amsterdam, **1994**.
[73] J. C. Elliot in *Les matériaux en phosphate de calcium. Aspects fondamentaux* (Eds.: E. Brès, P. Hardouin), Sauramps Medical, Montpellier, **1998**.
[74] J. E. Harries, D. W. L. Hukins, S. S. Hasnain, *J. Phys. C* **1986**, *19*, 6859 – 6872.
[75] J. E. Harries, D. W. L. Hukins, C. Holt, S. S. Hasnain, *J. Cryst. Growth* **1987**, *84*, 563 – 570.
[76] M. G. Taylor, K. Simkiss, J. Simmons, L. N. Y. Wu, R. E. Wuthier, *Cell. Mol. Life Sci.* **1998**, *54*, 192 – 202.
[77] F. Peters, K. Schwarz, M. Epple, *Thermochim. Acta* **2000**, *361*, 131 – 138.
[78] K. Onuma, A. Ito, *Chem. Mater.* **1998**, *10*, 3346 – 3351.
[79] D. Skrtic, A. W. Hailer, S. Takagi, J. M. Antonucci, E. D. Eanes, *J. Dent. Res.* **1996**, *75*, 1679 – 1686.
[80] D. Skrtic, J. M. Antonucci, E. D. Eanes, *Dent. Mater.* **1996**, *12*, 295 – 301.
[81] M. S. Park, E. D. Eanes, J. M. Antonucci, D. Skrtic, *Dent. Mater.* **1998**, *14*, 137 – 141.
[82] D. Skrtic, J. M. Antonucci, E. D. Eanes, F. C. Eichmiller, G. E. Schumacher, *J. Biomed. Mater. Res.* **2000**, *53*, 381 – 391.
[83] C. Schiller, M. Siedler, F. Peters, M. Epple, *Ceram. Trans.* **2001**, *114*, 97 – 108.
[84] W. Linhart, F. Peters, W. Lehmann, A. F. Schilling, K. Schwarz, M. Amling, J. M. Rueger, M. Epple, *J. Biomed. Mater. Res.* **2001**, *54*, 162 – 171.
[85] D. Tadic, M. Epple, *Biomed. Tech.* **2001**, 224 – 225.
[86] D. Tadic, F. Peters, M. Epple, *Biomaterials* **2002**, *23*, 2553 – 2559.
[87] P. W. Brown, R. I. Martin, *J. Phys. Chem. B* **1999**, *103*, 1671 – 1675.
[88] A. Mortier, J. Lemaitre, L. Rodrique, P. G. Rouxhet, *J. Solid State Chem.* **1989**, *78*, 215 – 219.
[89] J. Jeanjean, U. Vincent, M. Fedoroff, *J. Solid State Chem.* **1994**, *103*, 68 – 72.
[90] N. Rangavittal, A. R. Landa-Cánovas, J. M. González-Calbet, M. Vallet-Regi, *J. Biomed. Mater. Res.* **2000**, *51*, 660 – 668.
[91] J. Y. Kim, R. R. Fenton, B. A. Hunter, B. J. Kennedy, *Aust. J. Chem.* **2000**, *53*, 679 – 686.
[92] P. Layrolle, A. Lebugle, *Chem. Mater.* **1994**, *6*, 1996 – 2004.
[93] P. Layrolle, A. Lebugle, *Chem. Mater.* **1996**, *8*, 134 – 144.
[94] W. Suchanek, M. Yoshimura, *J. Mater. Res.* **1998**, *13*, 94 – 117.
[95] L. L. Hench, *J. Am. Ceram. Soc.* **1998**, *81*, 1705 – 1728.

[96] M. Fountoulakis, M. F. Takacs, P. Berndt, H. Langen, B. Takacs, *Electrophoresis* **1999**, *20*, 2181 – 2195.
[97] M. Mirshahi, L. Camoin, C. Nicolas, I. Ghedira, J. Cozette, J. P. Faure, *Curr. Eye Res.* **1999**, *18*, 327 – 334.
[98] R. Freitag, S. Vogt, M. Modler, *Biotechnol. Prog.* **1999**, *15*, 573 – 576.
[99] J. Wissing, S. Heim, L. Flohe, U. Bilitewski, R. Frank, *Electrophoresis* **2000**, *21*, 2589 – 2593.
[100] S. R. Shepard, C. Brickman-Stone, J. L. Schrimsher, G. Koch, *J. Chromatogr. A* **2000**, *891*, 93 – 98.
[101] G. Yin, Z. Liu, R. Zhou, J. Zhan, J. Wang, N. Yuan, *J. Chromatogr. A* **2001**, *918*, 393 – 399.
[102] L. C. Chow, *Nippon Seramikkusu Kyokai Gakujutsu Ronbunshi* **1991**, *99*, 954 – 964.
[103] E. Fernandez, F. J. Gil, M. P. Ginebra, F. C. M. Driessens, J. A. Planell, S. M. Best, *J. Mater. Sci. Mater. Med.* **1999**, *10*, 169 – 176.
[104] E. Fernandez, F. J. Gil, M. P. Ginebra, F. C. M. Driessens, J. A. Planell, S. M. Best, *J. Mater. Sci. Mater. Med.* **1999**, *10*, 177 – 183.
[105] S. Weiner, H. D. Wagner, *Annu. Rev. Mater. Sci.* **1998**, *28*, 271 – 298.
[106] S. Weiner, W. Traub, H. D. Wagner, *J. Struct. Biol.* **1999**, *126*, 241 – 255.
[107] H. Limeback, *Curr. Opin. Dent.* **1991**, *1*, 826 – 835.
[108] N. M. Hancox, *Biology of Bone*, Cambridge University Press, Cambridge, **1972**.
[109] W. E. Brown, L. C. Chow, *Annu. Rev. Mater. Sci.* **1976**, *6*, 213 – 236.
[110] J. Currey, *The Mechanical Adaptations of Bones*, Princeton University Press, Princeton, **1984**.
[111] R. Lakes, *Nature* **1993**, *361*, 511 – 515.
[112] A. C. Lawson, J. T. Czernuszka, *Proc. Inst. Mech. Eng. Part H* **1998**, *212*, 413 – 425.
[113] J. D. Hartgerink, E. Beniash, S. I. Stupp, *Science* **2001**, *294*, 1684 – 1688.
[114] A. Jodaikin, S. Weiner, Y. Talmon, E. Grossman, W. Traub, *Int. J. Biol. Macromol.* **1988**, *10*, 349 – 352.
[115] A. G. Fincham, J. Moradian-Oldak, T. G. H. Diekwisch, D. M. Lyaruu, J. T. Wright, P. Bringas, H. C. Slavkin, *J. Struct. Biol.* **1995**, *115*, 50 – 59.
[116] M. Iijima, Y. Moriwaki, *Calcif. Tiss. Int.* **1990**, *47*, 237 – 242.
[117] L. C. Bonar, M. Shimizu, J. E. Roberts, R. G. Griffin, M. J. Glimcher, *J. Bone Miner. Res.* **1991**, *6*, 1167 – 1176.
[118] C. Rey, V. Renugopalakrishnan, B. Collins, M. J. Glimcher, *Calcif. Tissue Int.* **1991**, *49*, 251 – 258.
[119] C. Rey, J. L. Miquel, L. Facchini, A. P. Legrand, M. J. Glimcher, *Bone* **1995**, *16*, 583 – 586.
[120] W. E. Brown, *Clin. Orthop. Relat. Res.* **1966**, *44*, 205 – 220.
[121] M. S. Tung, W. E. Brown, *Calcif. Tissue Int.* **1983**, *35*, 783 – 790.
[122] M. S. Tung, W. E. Brown, *Calcif. Tissue Int.* **1985**, *37*, 329 – 331.
[123] W. E. Brown, N. Eidelman, B. Tomazic, *Adv. Dent. Res.* **1987**, *1*, 306 – 313.
[124] C. Siew, S. E. Gruninger, L. C. Chow, W. E. Brown, *Calcif. Tissue Int.* **1992**, *50*, 144 – 148.
[125] E. D. Eanes, I. H. Gillessen, A. S. Posner, *Nature* **1965**, *208*, 365 – 367.
[126] J. D. Termine, A. S. Posner, *Science* **1966**, *153*, 1523 – 1525.
[127] J. D. Termine, A. S. Posner, *Nature* **1966**, *211*, 268 – 270.
[128] R. A. Harper, A. S. Posner, *Proc. Soc. Exp. Biol. Med.* **1966**, *122*, 137 – 142.
[129] A. S. Posner, *Physiol. Rev.* **1969**, *49*, 760 – 792.
[130] A. S. Posner, *Fed. Proc.* **1973**, *32*, 1933 – 1937.
[131] A. L. Boskey, A. S. Posner, *J. Phys. Chem. A* **1973**, *77*, 2313 – 2317.
[132] A. S. Posner, *Bull. Hosp. Jt. Dis.* **1978**, *39*, 126 – 144.
[133] M. J. Glimcher, L. C. Bonar, M. D. Grynpas, W. J. Landis, A. H. Roufosse, *J. Cryst. Growth* **1981**, *53*, 100 – 119.
[134] J. M. Burnell, E. J. Teubner, A. G. Miller, *Calcif. Tissue Int.* **1980**, *31*, 13 – 19.
[135] S. Weiner, W. Traub, *FEBS Lett.* **1986**, *206*, 262 – 266.
[136] E. D. Pellegrino, R. M. Blitz, *Calcif. Tissue Res.* **1972**, *10*, 118 – 135.
[137] R. Legros, N. Balmain, G. Bonel, *Calcif. Tissue Int.* **1987**, *41*, 137 – 144.
[138] H. P. Wiesmann, L. Chi, U. Stratmann, U. Plate, H. Fuchs. U. Joos, H. J. Höhling, *Cell Tissue Res.* **1998**, *294*, 93 – 97..
[139] U. Plate, T. Kotz, H. P. Wiesmann, U. Stratmann, U. Joos, H. J. Höhling, *J. Microsc.* **1996**, *183*, 102 – 107.
[140] U. Stratmann, K. Schaarschmidt, H. P. Wiesmann, U. Plate, H. J. Höhling, *Cell Tissue Res.* **1996**, *284*, 223 – 230.
[141] M. Epple, P. Lanzer, *Z. Kardiol.* **2001**, *90* (Suppl. 3), III/2 – III/5.
[142] W. Jahnen-Dechent, T. Schinke, A. Trindl, W. Muller-Esterl, F. Sablitzky, S. Kaiser, M. Blessing, *J. Biol. Chem.* **1997**, *272*, 31496 – 31503.
[143] T. Schinke, M. D. McKnee, G. Karsenty, *Nat. Genet.* **1999**, *21*, 150 – 151.
[144] W. Jahnen-Dechent, G. Schäfer, A. Heiss, J. Grötzinger, *Z. Kardiol.* **2001**, *90* (Suppl. 3), III/47 – III/56.
[145] P. Ducy, M. Amling, S. Takeda, M. Priemel, A. F. Schilling, F. T. Beil, J. Shen, C. Vinson, J. M. Rueger, G. Karsenty, *Cell* **2000**, *100*, 197 – 207.
[146] E. Rönnholm, *J. Ultrastruct. Res.* **1962**, *6*, 249 – 303.
[147] M. U. Nylen, E. D. Evans, K. A. Omnel, *J. Cell. Biol.* **1963**, *18*, 109 – 123.
[148] Y. Miake, S. Shimoda, M. Fukae, T. Aoba, *Calcif. Tissue Int.* **1993**, *53*, 249 – 256.
[149] G. Daculsi, J. Menanteau, L. M. Kerebel, D. Mitre, *Calcif. Tissue Int.* **1984**, *36*, 550 – 555.
[150] A. Jodaikin, W. Traub, S. Weiner, *J. Ultrastruct. Res.* **1984**, *89*, 324 – 332.
[151] R. M. Frank, R. F. Sognnaes, R. Kerns in *Calcification in Biological Systems*, AAAS, Washington, DC, **1960**, pp. 163 – 202.
[152] I. Schroeder, R. M. Frank, *Cell. Tissue Res.* **1985**, *242*, 449 – 451.
[153] E. F. Brès, J. C. Voegel, R. M. Frank, *J. Microsc.* **1990**, *160*, 183 – 201.
[154] S. Busch, U. Schwarz, R. Kniep, *Chem. Mater.* **2001**, *13*, 3260 – 3271.
[155] J. P. Simmer, A. G. Fincham, *Crit. Rev. Oral Biol. Med.* **1995**, *6*, 84 – 108.
[156] T. G. Diekwisch, B. J. Berman, S. Genters, H. C. Slavkin, *Cell. Tissue Res.* **1995**, *279*, 149 – 167.
[157] T. Aoba, *Anat. Rec.* **1996**, *245*, 208 – 218.
[158] C. Robinson, S. J. Brookes, W. A. Bonass, R. C. Shore, J. Kirkham, *Ciba Found. Symp.* **1997**, *205*, 156 – 170.
[159] C. E. Smith, *Crit. Rev. Oral. Biol. Med.* **1998**, *9*, 128 – 161.
[160] M. Sydney-Zax, I. Mayer, D. Deutsch, *J. Dent. Res.* **1991**, *70*, 913 – 916.
[161] C. Rey, V. Renugopalakrishnan, M. Shimizu, B. Collins, M. J. Glimcher, *Calcif. Tissue Int.* **1991**, *49*, 259 – 268.
[162] T. Takagi, T. Ogasawara, J. Tagami, M. Akao, Y. Kuboki, N. Nagai, R. Z. LeGeros, *Connect. Tissue Res.* **1998**, *38*, 181 – 187.
[163] K. A. Selvig, *Calcif. Tissue Res.* **1970**, *6*, 227 – 238.
[164] K. A. Selvig, *J. Ultrastruct. Res.* **1972**, *41*, 369 – 375.
[165] F. J. G. Cuisinier, P. Steuer, B. Senger, J. C. Voegel, R. M. Frank, *Cell. Tissue Res.* **1993**, *273*, 175 – 182.
[166] F. J. G. Cuisinier, P. Steuer, A. Brisson, J. C. Voegel, *J. Crystal Growth* **1995**, *156*, 443 – 453.
[167] P. Houllé, J. C. Voegel, P. Schultz, F. J. G. Cuisinier, *J. Dent. Res.* **1997**, *76*, 895 – 904.
[168] S. Mann, *Nature* **1993**, *365*, 499 – 505.
[169] J. Kirkham, J. Zhang, S. J. Brookes, R. C. Shore, S. R. Wood, D. A. Smith, M. L. Wallwork, O. H. Ryu, C. Robinson, *J. Dent. Res.* **2000**, *79*, 1943 – 1947.
[170] A. Boyde in *Tooth Enamel* (Eds.: M. V. Stack, R. W. Fearnhead), Wright, Bristol, **1965**, pp. 163 – 167.
[171] H. Warshawsky, A. Nanci, *J. Dental Res.* **1982**, *61*, 1504 – 1514.
[172] H. Warshawsky, *Anat. Rec.* **1989**, *224*, 242 – 262.
[173] A. L. Arsenault, B. W. Robinson, *Calcif. Tissue Int.* **1989**, *45*, 111 – 121.
[174] Y. Hayashi, *J. Electron Microsc.* **1992**, *41*, 387 – 391.
[175] Y. Hayashi, *J. Electron Microsc.* **1993**, *42*, 141 – 146.
[176] P. Bodier-Houllé, P. Steuer, J. M. Meyer, L. Bigeard, F. J. G. Cuisinier, *Cell. Tissue Res.* **2000**, *301*, 389 – 395.
[177] Y. Takano, Y. Hanaizumi, H. Oshima, *Anat. Rec.* **1996**, *245*, 174 – 185.
[178] W. Dong, H. Warshawsky, *Adv. Dent. Res.* **1996**, *10*, 232 – 237.
[179] P. Person in *Cartilage: Structure, Function and Biochemistry* (Ed.: B. K. Hall), Academic Press, New York, **1983**, pp. 31 – 57.
[180] M. L. Moss, L. Moss-Salentijn in *Cartilage: Structure, Function and Biochemistry* (Ed.: B. K. Hall), Academic Press, New York, **1983**, pp. 1 – 30.
[181] R. A. Robinson, D. A. Cameron, *J. Biophys. Biochem.* **1956**, *2* (Suppl.), 253 – 260.
[182] E. Bonucci, *J. Ultrastruct. Res.* **1967**, *20*, 33 – 50.

[183] S. Y. Ali, A. Wisby, L. Evans, J. Craig-Grey, *Calcif. Tissue Res.* **1977**, *22* (Suppl.), 490 – 493.
[184] S. Y. Ali in *Cartilage: Structure, Function and Biochemistry* (Ed.: B. K. Hall), Academic Press, New York, **1983**, pp. 343 – 378.
[185] I. M. Shapiro, A. Boyde, *Metab. Bone Dis. Relat. Res.* **1984**, *5*, 317 – 322.
[186] C. Rey, K. Beshah, R. Griffin, M. J. Glimcher, *J. Bone Miner. Res.* **1991**, *6*, 515 – 525.
[187] D. McConnell, *Bull. Geol. Soc. Am.* **1963**, *74*, 363 – 364.
[188] H. A. Lowenstam, *Chem. Geol.* **1972**, *9*, 153 – 166.
[189] W. Achilles, *Contrib. Nephrol.* **1987**, *58*, 59 – 64.
[190] W. Achilles, U. Jockel, A. Schaper, M. Burk, H. Riedmiller, *Scanning Microsc.* **1995**, *9*, 577 – 585.
[191] H. C. Stary, *Z. Kardiol.* **2000**, *89* (Suppl. 2), II/28 – II/35.
[192] K. M. Kim, *Z. Kardiol.* **2001**, *90* (Suppl. 3), III/99 – III/105.
[193] B. B. Tomazic, *Z. Kardiol.* **2001**, *90* (Suppl. 3), III/68 – III/80.
[194] E. Wintermantel, S. W. Ha, *Medizintechnik mit biokompatiblen Werkstoffen und Verfahren*, Springer, Heidelberg, **2002**.
[195] C. Giachelli, *Z. Kardiol.* **2001**, *90* (Suppl. 3), III/31 – III/38.
[196] B. Glasmacher, E. Nellen, H. Reul, G. Rau, *Materialwiss. Werkstofftech.* **1999**, *30*, 806 – 808.
[197] M. Deiwick, B. Glasmacher, E. Pettenazzo, D. Hammel, W. Castellon, G. Thiene, H. Reul, E. Berendes, H. H. Scheld, *Thorac. Cardiovasc. Surg.* **2001**, *49*, 78 – 83.
[198] E. Pettenazzo, M. Deiwick, G. Thiene, G. Molin, B. Glasmacher, F. Martignago, T. Bottio, H. Reul, M. Valente, *J. Thorac. Cardiovasc. Surg.* **2001**, *121*, 500 – 509.
[199] D. J. McCarty, H. M. Hogan, R. A. Gatter, M. Grossmann, *J. Bone Jt. Surg. Am. Vol.* **1966**, *48*, 309 – 317.
[200] *Oxford Textbook of Rheumatology*, *Vol. 2* (Eds.: P. J. Maddison, D. A. Isenberg, P. Woo, D. N. Glass), 2th ed., Oxford University Press, Oxford, **1998**, pp. 1567 – 1581.
[201] B. B. Tomazic in *Hydroxyapatite and Related Materials* (Eds.: P. W. Brown, B. Constantz), CRC, Boca Raton, FL, **1994**, pp. 93 – 116.
[202] G. Luo, P. Ducy, M. D. McKee, G. J. Pinero, E. Loyer, R. R. Behringer, G. Karsenty, *Nature* **1997**, *386*, 78 – 81.
[203] S. Albeck, S. Weiner, L. Addadi, *Chem. Eur. J.* **1996**, *2*, 278 – 284.
[204] N. Kessler, D. Perl-Treves, L. Addadi, M. Eisenstein, *Proteins* **1999**, *34*, 383 – 394.
[205] L. Addadi, S. Weiner, M. Geva, *Z. Kardiol.* **2001**, *90* (Suppl. 3), III/92 – III/98.
[206] D. Izhaky, L. Addadi, *Chem. Eur. J.* **2000**, *6*, 869 – 874.
[207] A. E. Canfield, M. J. Foherty, A. C. Wood, C. Farrington, B. Ashton, N. Begum, B. Harvey, A. Poole, M. E. Grant, R. P. Boot-Handford, *Z. Kardiol.* **2000**, *89* (Suppl. 2), II/20 – II/27.
[208] D. F. Williams, *Medical and Dental Materials*, *Vol. 14*, VCH, Weinheim, **1992**.
[209] P. Fratzl, *Phys. Unserer Zeit* **1999**, *30*, 196 – 200.
[210] R. Langer, *Acc. Chem. Res.* **2000**, *33*, 94 – 101.
[211] M. Bohner, *Injury* **2000**, *31* (Suppl. 4), D37 – D47.
[212] M. Bohner, *Eur. Spine J.* **2001**, *10*, S114 – S121.
[213] M. Epple, *Biomed. Tech.* **2001**, 36 – 38.
[214] S. I. Stupp, G. W. Ciegler, *J. Biomed. Mater. Res.* **1992**, *26*, 169 – 183.
[215] G. Berger, R. Gildenhaar, U. Ploska, M. Willfahrt, *Bioceramics* **1997**, *10*, 367 – 370.
[216] D. M. Liu, *J. Mater. Sci. Mater. Med.* **1997**, *8*, 227 – 232.
[217] S. I. Stupp, P. V. Braun, *Science* **1997**, *277*, 1242 – 1248.
[218] J. M. Rueger, W. Linhart, D. Sommerfeldt, *Orthopäde* **1998**, *27*, 89 – 95.
[219] J. M. Rueger, *Orthopäde* **1998**, *27*, 72 – 79.
[220] M. Epple, J. M. Rueger, *Nachr. Chem. Techn. Lab.* **1999**, *47*, 1405 – 1410.
[221] S. A. Redey, S. Razzouk, C. Rey, D. Bernache-Assollant, G. Leroy, M. Nardin, G. Cournout, *J. Biomed. Mater. Res.* **1999**, *45*, 140 – 147.
[222] R. Z. LeGeros, J. P. LeGeros in *Knochenersatzmaterialien und Wachstumsfaktoren* (Eds.: R. Schnettler, E. Markgraf), Thieme, Stuttgart, **1997**,pp. 180.
[223] Z. Z. Zyman, I. Ivanov, D. Rochmistrov, V. Glushko, N. Tkachenko, S. Kijko, *J. Biomed. Mater. Res.* **2001**, *54*, 256 – 263.
[224] G. Willmann, *Adv. Eng. Mater.* **1999**, *1*, 95 – 105.
[225] T. Kokubo, F. Miyaji, H. M. Kim, *J. Am. Ceram. Soc.* **1996**, *79*, 1127 – 1129.
[226] W. Q. Yan, T. Nakamura, K. Kawanabe, S. Nishigochi, M. Oka, T. Kokubo, *Biomaterials* **1997**, *18*, 1185 – 1190.
[227] T. Kokubo, *Acta Mater.* **1998**, *46*, 2519 – 2527.
[228] F. Barrère, P. Layrolle, C. A. van Blitterswijk, K. de Groot, *Bone* **1999**, *25*, 107S – 111S.
[229] F. Barrère, P. Layrolle, C. A. van Blitterswijk, K. de Groot, *J. Mater. Sci. Mater. Med.* **2001**, *12*, 529 – 534.
[230] T. Kokubo, H. M. Kim, M. Kawashita, T. Nakamura, *Z. Kardiol.* **2001**, *90* (Suppl. 3), III/86 – III/91.
[231] H. B. Wen, J. R. de Wijn, C. A. van Blitterswijk, K. de Groot, *J. Biomed. Mater. Res.* **1999**, *46*, 245 – 252.
[232] T. Kokubo, *Thermochim. Acta* **1996**, *280/281*, 479 – 490.
[233] H. B. Wen, R. A. J. Dalmeijer, F. Z. Cui, C. A. van Blitterswijk, K. de Groot, *J. Mater. Sci. Mater. Med.* **1998**, *9*, 925 – 930.
[234] C. Loty, J. M. Sautier, H. Boulekbache, T. Kokubo, H. M. Kim, N. Forest, *J. Biomed. Mater. Res.* **2000**, *49*, 423 – 434.
[235] H. M. Kim, T. Miyazaki, T. Kokubo, T. Nakamura in *Bioceramics 13*, *Vol. 192 – 195* (Eds.: S. Giannini, A. Moroni), Trans Tech Publications, Ütikon-Zürich, **2001**, pp. 47 – 50.
[236] K. D. Kühn, *Bone Cements*, Springer, Berlin, **2000**.
[237] J. S. Choi, M. Köller, D. Müller, G. Muhr, M. Epple, *Biomed. Tech.* **2001**, 226 – 227.
[238] S. Mann, G. A. Ozin, *Nature* **1996**, *382*, 313 – 318.
[239] S. Mann, *J. Chem. Soc. Dalton Trans.* **1997**, 3953 – 3961.
[240] S. Weiner, L. Addadi, *J. Mater. Chem.* **1997**, *7*, 689 – 702.
[241] J. Moradian-Oldak, *Matrix Biol.* **2001**, *20*, 293 – 305.
[242] W. Pompe, S. Lampenscherf, S. Rößler, D. Scharnweber, K. Weis, H. Worch, J. Hofinger, *Mater. Sci. Forum* **1999**, *308 – 311*, 325 – 330.
[243] G. A. Ozin, N. Varaksa, N. Coombs, J. E. Davies, D. D. Perovic, M. Ziliox, *J. Mater. Chem.* **1997**, *7*, 1601 – 1607.
[244] S. I. Stupp, G. C. Mejicano, J. A. Hanson, *J. Biomed. Mater. Res.* **1993**, *27*, 289 – 299.
[245] S. I. Stupp, J. A. Hanson, J. A. Eurell, G. W. Ciegler, A. Johnson, *J. Biomed. Mater. Res.* **1993**, *27*, 301 – 311.
[246] S. Weihe, M. Wehmöller, A. Tschakaloff, R. von Oepen, C. Schiller, M. Epple, H. Eufinger, *Mund Kiefer Gesichtschir.* **2001**, *5*, 299 – 304.
[247] M. B. Tomson, G. H. Nancollas, *Science* **1978**, *200*, 1059 – 1060.
[248] M. Iijima, Y. Moriwaki, R. Yamaguchi, Y. Kuboki, *Connect. Tissue Res.* **1997**, *36*, 73 – 83.
[249] M. Iijima, Y. Moriwaki, T. Takagi, J. Moradian-Oldak, *J. Cryst. Growth* **2001**, *222*, 615 – 626.
[250] M. Iijima, Y. Moriwaki, H. B. Wen, A. G. Fincham, J. Moradian-Oldak, *J. Dental Res.* **2002**, *81*, 69 – 73.
[251] R. Kniep, S. Busch, *Angew. Chem.* **1996**, *108*, 2788 – 2791; *Angew. Chem. Int. Ed. Engl.* **1996**, *35*, 2624 – 2627.
[252] S. Busch, H. Dolhaine, A. DuChesne, S. Heinz, O. Hochrein, F. Laeri, O. Podebrad, U. Vietze, T. Weiland, R. Kniep, *Eur. J. Inorg. Chem.* **1999**, 1643 – 1653.
[253] K. Schwarz, M. Epple, *Chem. Eur. J.* **1998**, *4*, 1898 – 1903.
[254] F. Peters, M. Epple, *Z. Kardiol.* **2001**, *90* (Suppl. 3), III/81 – III/85.
[255] F. Peters, M. Epple, *J. Chem. Soc. Dalton Trans.* **2001**, 3585 – 3592.
[256] S. V. Dorozhkin, E. I. Dorozhkina, F. Peters, M. Epple, *Z. Kardiol.* **2002**, in press.
[257] G. Falini, M. Gazzano, A. Ripamonti, *J. Mater. Chem.* **2000**, *10*, 535 – 538.
[258] I. Izquierdo-Barba, A. J. Salinas, M. Vallet-Regi, *J. Biomed. Mater. Res.* **2000**, *51*, 191 – 199.
[259] M. Vallet-Regi, J. Pérez-Pariente, I. Izquierdo-Barba, A. J. Salinas, *Chem. Mater.* **2000**, *12*, 3770 – 3775.
[260] S. V. Dorozhkin, E. I. Dorozhkina, M. Epple, **2002**, unpublished results.
[261] J. S. Rees, *Eur. J. Oral Sci.* **1998**, *106*, 1028 – 1032.

Exhibit A-3

Chung-Wei Yang and Truan-Sheng Lui. Biological and Biomedical Coatings Handbook: Processing and Characterization. Chapter 6: Hydrothermal Crystallization with Microstructural Self-Healing Effect on Mechanical and Failure Behaviors of Plasma-Sprayed Hydroxyapatite Coatings. 2011: 240-253.

Referring to past reports, it has been generally recognized that postheat treatments such as air or vacuum heat treatments, spark plasma sintering (SPS) technique, and hydrothermal treatments, etc., can significantly help to improve the phase composition, crystallinity, mechanical properties, and biological responsibility of plasma-sprayed HACs [16,45,52–65]. In addition, the steam treatment during the in-flight stage of the plasma spraying can also result in a significant increase in the crystallinity (from 58% to 79%) of plasma-sprayed HACs [66]. The mechanism can be recognized that the entrapping of water molecules into HA droplets and the improvement in crystallinity and phase purity from amorphous calcium phosphate to HA is achieved by reversing the HA decomposition through providing extra OH^-. Overall, the degree of crystallinity, phase stability, and postheat treatments of calcium phosphate and plasma-sprayed HACs—which are closely related to heating temperatures, atmosphere, water molecules, and partial steam pressure—is presented in the next section. Considering that HA is one of the natural apatite minerals and the phase stability in an atmosphere with plenty of water molecules and saturated steam pressure, the hydrothermal synthesis, which is quite similar to mineral formation environment in the earth, is an important method in the preparation of HA crystals. The hydrothermal technique and hydrothermal materials processing are becoming a popular field of research for scientists and technologists of various disciplines. Therefore, Sections 6.3 and 6.4 will specifically reveal the advantages and effects of hydrothermal crystallization on improving the microstructural homogeneity, phase purity, biological responses, adhesive bonding strength, and failure mechanism of plasma-sprayed HACs. In addition, the kinetics of hydrothermal crystallization, which is significantly related to the saturated steam pressure in a hermetical system, will also be deduced and discussed in Section 6.3. The reliability and failure behaviors of HA-coated implants should be studied in detail to ensure their long-term stability in clinical applications, since biological degradation and failure of artificial joints that result from dissolution and dissociation may occur during the period of implantation. Thus, knowledge of statistical analysis of the reliability engineering by the Weibull model will be represented in Section 6.5. Meanwhile, the failure probability density function, cumulative failure probability, failure rate, and reliability functions, which correlate with the cohesive strength of coatings and the adhesive strength of a coating to a metal substrate, will also be reviewed in this section.

Characteristics of HA Coatings

Phase Stability of the Crystalline HA Powders

Pure HA has a theoretical composition of 39.68 wt.% Ca element, 18.45 wt.% of P element, a Ca/P weight ratio of 2.151, and a Ca/P molar ratio of 1.667. According to criterion of ASTM F1185-88, the acceptable composition for commercial HA powder should be a minimum value of 95 wt.% HA purity, as established by x-ray diffraction analysis. HA can be produced by using a variety of methods, and the characteristics of raw HA powders have significant effects on the subsequent products with HA being in the form of dense or porous bulks and in coatings. In biological and clinical applications, HA bulks and HA-coated implants are often immersed and applied in solutions or in the body fluids. Thus, the stability of HA bulks and coating implants is significantly affected by the environmental temperatures and the pH values.

Generally, high-purity HA powder is soluble in acid solution, insoluble in alkaline solution, and slightly soluble in water. Also, the solubility of crystalline HA is varied with the presence of amino acids, proteins, enzymes, and other organic compounds. The dissolution rate also depends on the particle size and the shape of HA granules and the porosity, crystal size, and crystallinity of HA implants. As indicated by Driessens [67], there are only two calcium phosphate compounds that are stable at room temperature when in contact with aqueous solutions. It is the pH value of the solution that determines which one is stable. At a pH value lower than 4.2, the component $CaHPO_4{\cdot}2H_2O$ (dicalcium phosphate) is the most stable phase, while at a pH value higher than 4.2, well-crystallized HA is a stable phase. In addition, Adam et al. found that the surface of tricalcium phosphate ($Ca_3(PO_4)_2$, TCP) and tetracalcium phosphate ($Ca_4P_2O_9$, TP) compounds will be coated with thin HA layers through the phase transformation at a suitable pH value [68], and these reactions can be represented as follows [69].

$$4Ca_3(PO_4)_2 \rightarrow Ca_{10}(PO_4)_6(OH)_2 + 2Ca^{2+} + 2HPO^{4-} \quad (6.1)$$

$$3Ca_4P_2O_9 + 3H_2O \rightarrow Ca_{10}(PO_4)_6(OH)_2 + 2Ca^{2+} + 4OH^- \quad (6.2)$$

The in vitro dissolution properties of crystalline HA depend on several factors, such as the type and concentration of the buffered or unbuffered solutions, pH of the solutions, degree of saturation, solid/solution ratio, the length of suspension in solutions, and the crystallinity of the HA [70–74]. In the case of ceramic HA bulks, the degree of porosities, defect structure, the amount, and the type of other calcium phosphate phases present also display significant influences. The extent of dissolution of the ceramic HA bulk is less in lactic acid buffer compared to that in acetic acid buffer [75]. For the crystalline HA powders containing other calcium phosphate phases, the extent of dissolution will be affected by the type and the amount of non-HA phases. According to previous studies made by Ducheyne et al. [76] and Radin and Ducheyne [77], the evaluation of dissolution rate for the nonwell-crystallized HA, α-TCP, β-TCP, T,P and crystallized HA were measured in 0.05 mol Tris(hydroxy)methylaminomethane-HCl buffered solution at pH 7.3, 37°C for immersion time periods ranging from 15 min to 72 h. The results indicated that the concentration of dissolved Ca^{2+} reaches saturation (about 1.5 mM) for TP in a few minutes immersion, and the value significantly exceeds that of β-TCP ([Ca^{2+}] is about 1×10^{-1} mM) and crystalline HA ([Ca^{2+}] is less than 1×10^{-1} mM) after 24 h immersion. Comparing the dissolution rate of β-TCP with α-TCP, the dissolution rate of β-TCP is about four times larger than that of α-TCP. Therefore, it can be recognized that the dissolution rate of various monophasic calcium phosphate compounds decreased in the following order [76–78]:

Amorphous HA > TP > α-TCP > β-TCP > crystalline HA

In addition, the results of previous studies also showed that the values of solubility product (K) for β-TCP and crystalline HA powder are 1.2×10^{-29} $mol^5\ l^{-5}$ and 3.04×10^{-59} $mol^9\ l^{-9}$ at 25°C, respectively [79,80]. Thus, when HA bulks or HA-coated implants, which have a low crystallinity and high impurity phase content, are implanted, it may result in the dissolution, degradation of mechanical properties, and the dissociation of implants [47,48,76]. Therefore, the degree of crystallinity, phases, and chemical compositions of ceramic HA bulks and HA-coated implants must be controlled in order to maintain long-term stability in the body fluid after implantation.

The thermal stability of crystalline HA is rather complicated. Figure 6.2 shows the phase diagrams of $CaO–P_2O_5$ system [81] at high temperature without water present (Figure 6.2a) and with a partial water vapor pressure of 500 mmHg (Figure 6.2b). Various calcium phosphate compounds can be found at high temperatures, such as α-C_3P (α-TCP), C_4P (TP), monetite (C_2P), and mixtures of CaO and C_4P. It can be seen that crystalline HA is not stable when the ambient atmosphere contains no water. If the partial water vapor pressure is increased, then the crystalline HA becomes a stable phase and it can be found in the phase diagram, as shown in Figure 6.2b. Previous studies reported that the partial dehydration of HA significantly occurred at a temperature higher than 900°C [82], and the oxyhydroxyapatite (OHA) in the form of $Ca_{10}(PO_4)_6(OH)_{0.8}O_{0.6}V_{0.6}$ may occur when the heating temperature is higher than 1100°C. With increasing heating temperatures higher than 1300°C, the HA would decompose and the apatite structure changes to a new space group with the appearance of α-TCP and TP according to the reaction shown in Equation 6.3 [83]. The α-TCP is resulted from the transformation of β-TCP at temperatures above 1300°C, and the reaction shown in Equation 6.3 is followed by the reaction shown in Equation 6.4. Thus, it is generally recognized that the highest temperature of HA without phase decomposition is about 1300°C in an ambient atmosphere that contains no water.

$$Ca_{10}(PO_4)_6(OH)_2 \rightarrow 2\alpha\text{-}Ca_3(PO_4)_2 + Ca_4P_2O_9 + H_2O \quad (6.3)$$

$$Ca_4P_2O_9 \rightarrow \alpha\text{-}Ca_3(PO_4)_2 + CaO \quad (6.4)$$

The importance of partial water vapor pressure is shown more clearly in Figure 6.3, which reveals the influence of water vapor pressure on the phase stability of HA. At 1300°C

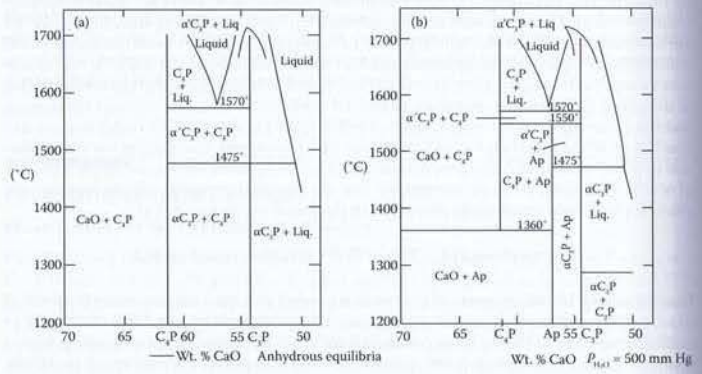

FIGURE 6.2
Phase diagram of the system $CaO–P_2O_5$ at high temperature: (a) no water present and (b) partial water vapor pressure of 500 mmHg. (From Gross et al., *J. Biomed. Mater. Res.*, 39, 580–587, 1998. With permission.)

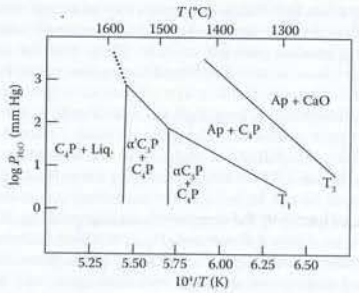

FIGURE 6.3
Influence of ambient water vapor pressure on phase compositions of calcium phosphate. (From Gross et al., *J. Biomed. Mater. Res.*, 39, 580–587, 1998. With permission.)

(or 10^4/T for Equation 6.4), this diagram shows the stable phases are α-TCP and TP when the water vapor pressure is 1 mmHg (log $P_{H_2O} = 0$). The stable phases are HA + TP, and HA + CaO at partial water vapor pressures of about 10 mmHg (log $P_{H_2O} = 1$) and 100 mmHg (log $P_{H_2O} = 2$), respectively. It reveals that a higher partial water vapor pressure can help to maintain and replenish the OH^- groups within the HA crystal structure, and to increase the phase-stabilized temperature of HA. Applying a steam atmosphere or a high steam pressure is an effective method to maintain high thermal stability of HA during the manufacturing process [84]. For a calcium phosphate compound with a Ca/P ratio exceeding HA by only a few percent, stable phases would be changed between α-TCP, TP, HA, and CaO. When the partial water vapor pressure is presented, the formation of the α-CP, β-TCP, and TP phases will be minimized and HA will be the more stable phase below 1550°C [8,12], as shown in Figure 6.2b. But HA becomes unstable and it will still decompose into α-TCP and TP following the reaction shown in Equation 6.3 at temperatures higher than 1550°C.

Plasma-Sprayed HACs

Thermal spray processing has been applied for many years to deposit layer coatings for various purposes such as wear resistance, thermal barrier coatings (TBCs), biocompatibility, and so forth. The major advantages of the thermal spray processes are the ability to apply a wide variety of compositions, including most metallic and ceramic materials, without significantly heating substrate surface to be coated [85]. The main thermal spray techniques include flame spraying, atmospheric plasma spraying (APS), vacuum plasma spraying (VPS), high velocity oxygen fuel (HVOF) spraying, arc metallization, and detonation gun spraying. Among these techniques, the plasma spraying process is becoming the extensively applied technique of the thermal spraying methods and is commonly used to deposit HA into dental implants and orthopedic prostheses. Investigations into some calcium phosphate compounds and HA coatings on metallic implants, such as Ti–6Al–4V,

started with the observation that HA in the pores of a metal implant with a porous coating would significantly affect the rate and vitality of bone ingrowth onto pores [15,86].

The plasma spraying process was patented in 1960s, and the technical utilization of plasma as a high-temperature source is realized in the plasma torch. The plasma gun consists of a cone-shaped tungsten cathode and a cylindrical copper anode. The principle of plasma spraying is to induce an arc by a high current density and a high electric potential between the anodic copper nozzle and tungsten cathode. Gases flow through the annular space between these two electrodes, and an arc is initiated by a high-frequency discharge. Noble gases of He and Ar are usually used as the primary plasma-generating gas. Diatomic gases of H_2 and N_2 can be used as the secondary gas to increase the enthalpy of plasma flame. Factors influencing the degree of particles melting during plasma spraying include variables such as current density and gas mixture that control the temperature of the plasma. The widely used plasma-generating gas is pure Ar (purity <99.95 wt.%). Since the thermal conductivity and the heat conduction potential for diatomic gases such as H_2 and N_2 are much higher than Ar [87], a mixed gas composition with Ar and H_2/N_2 gives quite a hotter plasma torch than 100% Ar gas. When well-crystallized HA powders are injected into the high-temperature plasma flame (normally in the range of 1×10^4 to $1.5 \times 10^{4\circ}$C), small granules will be evaporated in the flame, and larger particles are melted or partially melted quickly by the high-temperature plasma flame. Then these melted droplets are accelerated to about 200 m/s before impacting the substrate [88,89]. The high-impact velocity supplies high kinetic energy, which is expended in spreading the molten or semimolten droplets and creating a lamellar microstructure. In addition, the high cooling rate upon impact is estimated to be of the order of 10^6 to 10^8 K s^{-1} [90]. Therefore, the large contact area with the substrate and the rapid solidification result in producing amorphous calcium phosphate (ACP) component within coatings, and it is more commonly found at the coating/substrate interface.

Since the plasma spraying process involves high temperature and rapid solidification, it will result in the dehydroxylation and decomposition of HA and the formation of an amorphous structure within coatings. This decomposition sequence occurs in these steps [91,92]:

$$Ca_{10}(PO_4)_6(OH)_2 \rightarrow Ca_{10}(PO_4)_6(OH)_{2-2x}O_xV_x + xH_2O \quad (6.5)$$

$$Ca_{10}(PO_4)_6(OH)_{2-2x}O_xV_x \rightarrow Ca_{10}(PO_4)_6O_xV_x + (1-x)H_2O \quad (6.6)$$

$$Ca_{10}(PO_4)_6O_xV_x \rightarrow 2\alpha\text{-}Ca_3(PO_4)_2 + Ca_4P_2O_9 \quad (6.7)$$

$$\alpha\text{-}Ca_3(PO_4)_2 \rightarrow 3CaO + P_2O_5 \quad (6.8)$$

$$Ca_4P_2O_9 \rightarrow 4CaO + P_2O_5 \quad (6.9)$$

The symbol "V" in the formulas of oxyhydroxyapatite ($Ca_{10}(PO_4)_6(OH)_{2-2x}O_xV_x$, OHA) and oxyapatite ($Ca_{10}(PO_4)_6O_xV_x$, OA) refers to lattice vacancies in positions of the OH^- groups along the crystallographic *c*-axis in the structure of HA. Thus, the x-ray pattern of a plasma-sprayed HA coating shows the presence of α-TCP, β-TCP, TP, and CaO phases in addition to crystalline HA. The reduction in peak intensity and peak broadening of HA peaks provide an evidence for the formation of ACP. The formation of these additional

phases is a result of the extreme temperature of plasma flame and rapid cooling and highly reactive atmospheres that favor nonequilibrium and metastable structures.

When OA appears to be stable in the absence of water vapor environment, it will readily retransform to HA according to the reaction [93,94]

$$O^{2-}\text{ (solid)} + V\text{ (solid)} + H_2O\text{ (gas)} \rightarrow 2OH^-\text{ (solid)} \quad (6.10)$$

The equilibrium temperature of the reaction shown in Equation 6.7 is determined by the temperature of incongruent melting of HA at 1570°C [95]. Based on the decomposition sequence, a model has been developed [91,96,97] that shows the in-flight evolution of calcium phosphate phases, as represented in Figure 6.4. It shows that the inner core, which is still at a temperature below 1550°C, consists of HA, OHA, and OA as stable phases during the short residence time of HA particles in the plasma flame (reactions shown in Equations 6.5 and 6.6). The second shell of Figure 6.2b, which is heated to temperatures of 1360°C to 1570°C, just below the incongruent melting temperature of HA. It undergoes a solid state decomposition to a mixture of α-TCP and TP. The third shell was heated to temperatures above 1570°C following the reaction shown in Equation 6.7. The outer shell is composed of CaO and a melt whose Ca/P ratio shifts by continuous evaporation of P_2O_5 along the liquids of the phase diagram (Figure 6.2) toward CaO-richer phases following reactions shown in Equations 6.8 and 6.9. While impacting at the substrates, this molten phase solidifies to produce ACP with various Ca/P ratios [92,102].

X-ray diffraction (XRD) has been widely used for determining the phase composition, phase content, and crystal structure of plasma-sprayed HACs, as well as for estimating the index of crystallinity and identifying other calcium phosphate compounds generated as a result of the high-temperature spraying process. Figure 6.5 shows the x-ray diffraction patterns of the well-crystallized HA powders (Figure 6.5a) and the plasma-sprayed HACs (Figure 6.5b). The difference in the phase composition and crystallinity between well-crystallized HA and plasma-sprayed HACs are quite evident. The peak intensity of HA phase is significantly decreased after plasma spraying. In addition, it can be seen that a fairly high content of ACP and other impurity phases including TCP, TP, and CaO are represented in the plasma-sprayed HACs besides the desired HA phase. The reduction

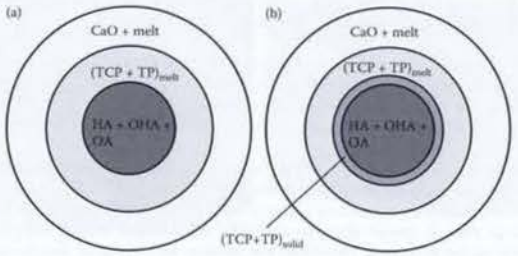

FIGURE 6.4
Schematic model of thermal decomposition of a spherical HA particle subjected to high temperature in a plasma flame at (a) a partial water vapor pressure of about 500 mmHg and (b) a partial water vapor pressure of about 10 mmHg. (From Heimann, R.B., *Surf. Coat. Technol.*, 201, 2012–2019, 2006. With permission.)

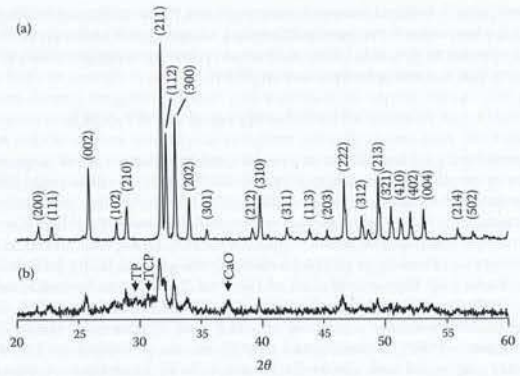

FIGURE 6.5
X-ray diffractions of (a) well-crystallized HA powder and (b) plasma-sprayed HACs.

in peak intensity and peak broadening of HA peaks suggest the formation of ACP [103]. The formation of these phases is a result of HA phase decomposition and dehydroxylation affected by extreme temperatures of plasma flame, rapid solidification, and highly reactive atmospheres that favor nonequilibrium or metastable structures according to the reactions described before. Plasma-sprayed HACs typically have high defect contents, amorphous components, and residual stresses, which result in a broadening of the x-ray diffraction peaks. In addition to providing the variation in phase composition, another material characteristic of plasma-sprayed HACs obtained through the x-ray diffraction analysis is the index of crystallinity. The crystallinity has been defined in different ways for biomedical applications, and it was initially used as an indication of the crystal size or perfection of the crystal lattice in HA crystals [98]. In order to quantitatively evaluate the crystallinity of plasma-sprayed HACs, a commonly used index of crystallinity (IOC) defined the ratio of the three strongest HA main peaks ((211), (112), and (300), JCPDS 9-432), the integral intensity of the plasma-sprayed HACs (I_c), and the well-crystallized single HA phase starting powders (I_p) according to the relationship IOC = $(I_c/I_p) \times 100\%$ [99–102]. As shown in Figure 6.5a, this method supposes that the IOC of the well-crystallized HA is 100%. According to this method, the IOC value of plasma-sprayed HACs with a diffraction pattern as shown in Figure 6.5b is about 20.3% [101].

Although x-ray diffraction has been a conventional and effective analysis method to obtain the phase composition and quantitative phase content of plasma-sprayed HACs, the limitation is that x-ray diffraction can only detect phases and provide an average value within a large area. It cannot provide sufficient information when amorphous components are the major products. Therefore, the feasible technique of Raman spectroscopy provides another way to reinforce the application of the x-ray diffraction method. The Raman spectroscopy can provide information on the short and intermediate range ordering in the solids and it allows a direct and nondestructive detection from the sample surface. Since both in vitro and in vivo biological properties of plasma-sprayed HACs are

significantly dependent on the phases, detailed microstructure information such as the individual thermal-sprayed splats acquired with the Raman spectroscopy is important. Studies on thermal-sprayed splats can help to establish the understanding of individual splat's contribution to the phase composition of the thermal-sprayed coatings. In addition, the crystallinity of plasma-sprayed HACs and phase composition at various locations within individual thermal-sprayed HA splats have been quantitatively determined by the Raman spectroscopy analysis [66,94,104,105].

In addition to evaluating the index of crystallinity, it is also important to quantify the phase composition of amorphous component, crystalline HA, and other calcium phosphate phases of plasma-sprayed HACs by quantitative XRD analysis through the internal and external standards. However, pure phases and mixtures with different compositions are needed for establishing the calibration curves, and ACP is not easy to isolate and quantify. Thus, the lack of full quantification and its long task of obtaining calibration curves makes this technique unpopular. To fully determine the phase composition and quantify the amount of decomposed phases, including the amorphous component, of the as-sprayed coatings, the Rietveld method of structure determination from x-ray and neutron powder diffraction patterns is another effective way and has widely been used to study calcium phosphate compounds [60,106–111]. The Rietveld method creates an effective separation of the overlapping data from x-ray and neutron diffraction patterns, thereby allowing an accurate determination of the structure. This method has been successful and today, the structure of materials in the form of powders is being determined. In addition, a more widely used application of the Rietveld method is in determining the components of chemical mixtures. The conventional quantitative phase analysis (QPA), which is carried out using relative peak height ratios of HA and other phases involved by the Rietveld method provides a powerful tool that offers the user simultaneous quantitative phase determination of multiphase systems containing amorphous content. The quantitative analysis results of crystalline HA, amorphous, and various calcium phosphate phases plasma-sprayed and crystallized HACs will be represented in the next section.

Figure 6.6a shows the surface morphology of the plasma-sprayed HACs. It displays a typical microstructural feature, which is composed of completely molten splats (indicated by arrows), accumulated partially molten splats (marked by the circle), and thermal-induced

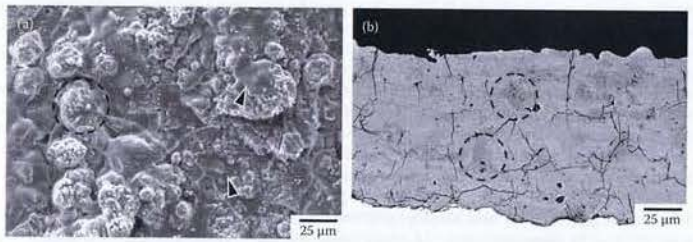

FIGURE 6.6
Typical plasma-sprayed HACs microstructural features for (a) surface morphology with microcracks, accumulated splats (marked by circles), and molten splats (indicated by arrows). (b) Cross-sectional microstructure showing spraying defects including pores and microcracks. Circle marks residual partial molten particle within plasma-sprayed HACs.

microcracks resulting from thermal contraction during the rapid cooling stage after plasma spraying. The cross-sectional feature of the plasma-sprayed HACs is shown in Figure 6.6b. According to the quantitative calculation by an image analyzer OPTIMAS 6.0 [63,64,101], the spraying defects content (in volume %), including microcracks and pores within the entire cross-sectional area of HACs, is about 4% for plasma-sprayed HACs in the case of Figure 6.6b. Although the plasma-sprayed coatings possess inevitable spraying defects, including pores and thermal-induced microcracks, they can be subjected to high densification due to the unapparent lamellar structure. Since the structural density of plasma-sprayed coatings is significantly affected by the variation of spraying parameters such as plasma gas flow rate (l min^{-1}), plasma power (kW), powder feed rate, surface speed, standoff distance, and so forth, the coating microstructure displayed in Figure 6.6b can be recognized as a dense HA coating (following the definition of the maximum porosity less than 5% by volume [8,9]) obtained from an appropriate spraying parameter. Besides the microstructural defects, a noteworthy feature with a mixture of dark gray and light gray regions is observed within plasma-sprayed HACs, as shown in Figure 6.6b. This distinguishable color contrast is resulted from the difference between amorphous and crystalline area of the coatings [102]. Other phases may be present in small quantities, but they cannot be distinguished from HA. During plasma spraying, the unmolten and partially molten particles are transferred to coatings with a morphology representative of the starting powders. Therefore, these dark gray regions marked by circles can be thought of as the crystalline region from the residual partially molten particles within plasma-sprayed HACs. This phenomenon is important in the performance of the HA coatings because the dissolution of amorphous regions could lead to failure for implants after a period of implantation. Therefore, it is possible to increase the crystallinity and in some cases the bonding strength of plasma-sprayed HACs by performing postheat treatments.

Crystallization of Plasma-Sprayed HACs during Heat Treatments

Referring to the reports about HA, many researchers have investigated the material and medical properties of plasma-sprayed HACs in the past 10 years. Amorphous calcium phosphate (ACP) is thermodynamically metastable and impurity calcium phosphate (including TCP, TP, and CaO, called the impurity phases) is undesirable for its dissolution problems in human body fluids. Therefore, previous studies pointed out that controlling spraying parameters [112] or performing appropriate thermal treatments (in vacuum, in an atmosphere with moisture or steam pressure and the spark plasma sintering (SPS) technique) are available methods that significantly promote the HA crystallization, improve the crystallinity and dissolution behaviors of coatings, and enhance the surface activity to the growth of apatite layers [16,59,65,66,99,113–115]. Additionally, reports have focused on the changes in phase composition, microstructural homogenization, and reduction in residual porosity of HACs [55–59,63,101], as well as the mechanism of crystallization of the coating layers [116].

Figure 6.7 illustrates the XRD patterns of plasma-sprayed HA-coated Ti–6Al–4V specimens with postvacuum and atmospheric heat treatments at 400°C, 500°C, 600°C, 700°C, and 800°C. The three strongest HA main peaks tend to become sharper with increasing heating temperatures, revealing that the plasma-sprayed HACs possess different degrees of crystallization after postheat treatment. For the atmospheric heat-treated HACs, the partial water vapor pressure of atmospheric moisture can help to recover and promote the reconstitution of TCP, TP, and ACP into crystalline HA. However, the vacuum heat-treated specimens possess more TCP and TP than the atmospheric heat-treated specimens.

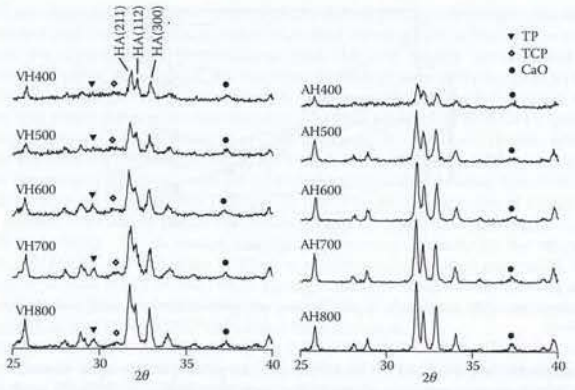

FIGURE 6.7
X-ray diffraction patterns of plasma-sprayed HACs with applying postvacuum heat treatment (VH series) and atmospheric heat treatment (AH-series) at 400°C to 800°C. (From Yang, C.W. and Lui, T.S., *Mater. Trans.*, 48(2), 211–218, 2007. With permission.)

According to the phase diagram of $CaO–P_2O_5$ system as shown in Figure 6.2, since there is a lack of ambient partial water vapor pressure during vacuum heating, TCP and TP phases cannot be eliminated without the replenishment of OH^- groups. In addition, the CaO remained within both of the heat-treated HACs because it cannot easily be converted into HA if the ambient heating atmosphere is without abundant H_2O molecules [54,59].

Heat treatment is recognized as a proven process of controlling the amount of amorphous calcium phosphate and quantification of the amorphous component has also been attempted by many studies [45,60,64,101,108–111,117]. In order to evaluate the content of ACP and other impurity phases displayed in Figure 6.7, the internal standard method [118] is one of the most common methods to quantitatively determine the fluctuation of phase composition within the heat-treated HACs. The integral intensity of known weight percent pure Si powder added in the specimens is taken as the internal standard. Wang et al. [45] and Chou and Chang [117] have established the calibration curves for calculating the content of ACP, TCP, TP, and CaO phases. The main peak integral intensity ratio between TCP, TP, CaO, and HA phase from various XRD patterns of heat-treated HACs are compared to the calibration curves and the concentrations (in wt.%) of these phases in various coatings are calculated. Figure 6.8 shows the impurity phase content at different temperatures for the vacuum heat-treated HACs (VH series). The impurity phases generally tend to decrease when the increased heating temperature reaches 600°C, at which the HACs contains the lowest content (about 20.3 wt.%) of total impurity phases. There is also a continuous decrease in amorphous content with increasing temperatures. However, when the heating temperature rises to a temperature range of 600°C to 800°C in vacuum, a significant increasing trend of impurity phases content (mostly TP and CaO phases) resulting from the decomposition of HA [54,101] can be recognized as the temperature increases further, resulting in greater total impurity phases about 26.1 wt.% at 800°C. For

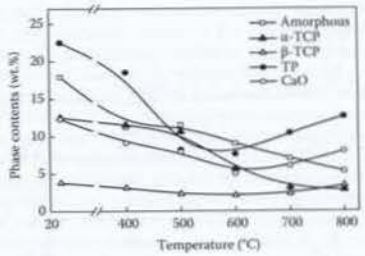

FIGURE 6.8
Phase content (in wt.%) of amorphous and calcium phosphate phases changed with vacuum heating temperatures.

the atmospheric heat-treated HACs (AH series), the partial water vapor pressure of atmospheric moisture can recover and promote the reconstitution of TCP, TP, and ACP into crystalline HA. The residual compound with a phase content of about 5 wt.% for 600°C to 800°C atmospheric heat-treated HACs is thought of as CaO [119]. Referring to the previous presentation in Section 6.2.2, the Rietveld analysis method with QPA is another effective way to determine the phase content of the plasma-sprayed and heat-treated HACs. Since the heat during plasma spraying and crystallization processes is difficult to ascertain, the quantity of ACP is not easy to determine in relation to the heat liberated. Therefore, the Rietveld analysis method with QPA provides a powerful way to completely quantify the associated amorphous component and crystalline phases within a multiphase system for any thermally treated material [60,108,109]. Figure 6.9 illustrates the variation in phase composition of plasma-sprayed powders with changing a series of plate power, which is determined by the QPA technique via Rietveld method [60]. It can be seen that the phase content of crystalline HA, ACP, and other impurity phases, including α-TCP, β-TCP, TP,

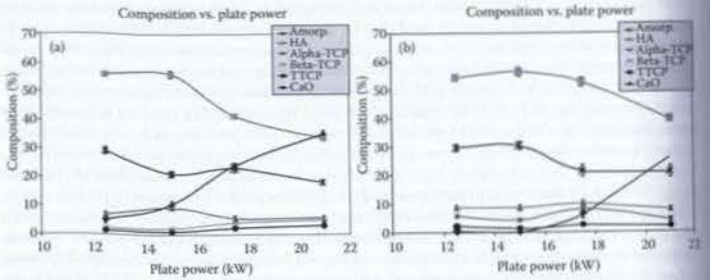

FIGURE 6.9
Phase composition of plasma-sprayed powders determined by quantitative phase analysis (QPA) technique via Rietveld method of (a) 7 wt.% and (b) 14 wt.% HA suspension feedstock for changing a series of plate power.

and CaO, are obtained. The phase decomposition during plasma spraying is quantitatively demonstrated and the amorphous content increased substantially at higher powers.

Because the crystallization of plasma-sprayed HACs is usually accompanied with a change in the coating dimensions, the variation in microstructure during heat treatments can be clarified through thermal dilatometry. In order to exclude the influence of metallic substrate and interfacial reaction between HA/Ti of the HA-coated Ti–6Al–4V specimens, only plasma-sprayed HAC test pieces of dimensions 20 (l) × 3 (w) × 3 (t) mm³ without Ti substrate are used for thermal dilatometry analysis by a dilatometer. The heating conditions are the same as the above-mentioned temperatures with a heating rate of 10°C/min, followed by furnace cooling after holding for 3 h. The dilatation curve of HACs during heating process is shown in Figure 6.10, which can be divided into three regions of markedly different slopes. The increased dilatation approaches linearity in the temperature intervals of 100°C to 400°C (region I). The linear increased dilatation represents that just a thermal expansion effect on the HACs during heating in temperature interval 100°C to 400°C, and the coefficient of thermal expansion (CTE, α) of sprayed HA coating layer can be suggested about 15.6×10^{-6} °C^{-1} calculated from the slope.

Besides thermal expansion effect in region II, however, the dilatation decreases in a nonlinear manner at heating temperatures from above 400°C to 700°C should be correlated with the main temperature interval for the crystallization of plasma-sprayed HACs. When the HA crystallization effect with a fair amount of volume contraction is larger than the thermal expansion of coatings in this region, the dilatation $\delta L/L_o$ (or the slope of the dilatation curve) decreased and even becomes a negative value, especially during the 500°C to 700°C heating interval. Combined with quantitative analysis as shown in Figure 6.8, the evidence is that an apparent change in phase content and crystallinity within this temperature interval. Although the investigations by Feng et al. [61] and Gross et al. [116] indicated that the crystallization has been identified as taking place at about 400°C, but the main HA crystallization region of the HACs should be suggested over 500°C heating temperatures. As the heating temperature approaches to 700°C, there is also a dilatation balance between crystallization and thermal expansion of HACs. Thus, the dilatation curve displays a linear thermal expansion larger than crystallization contraction over 700°C heating temperatures in region III.

Figure 6.11 also illustrates the thermal dilatometry curves for the HACs without Ti–6Al–4V, heating at 400°C, 500°C, 600°C, 700°C, and 800°C, respectively. They all show

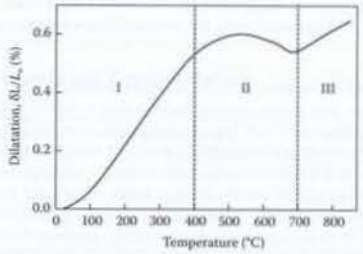

FIGURE 6.10
Dilatation curve of plasma-sprayed HACs for a single heating process through thermal dilatometry.

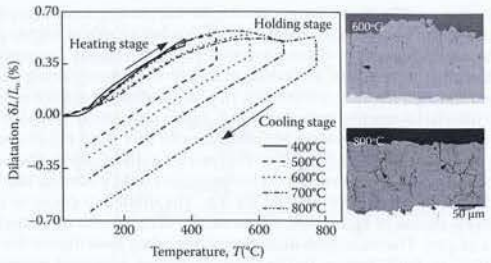

FIGURE 6.11
Dilatation curves of plasma-sprayed HACs obtained from heating, holding to cooling processes at 400°C to 800°C. (From Yang, C.W. and Lui, T.S., *Mater. Trans.*, 48(2), 211–218, 2007. With permission.)

an approximately linear thermal expansion when the heating temperature is in the range from 100°C to 400°C. The CTE of an HAC within this temperature range is also evaluated for about 15.6×10^{-6} °C^{-1}. In addition, it is worth noting that the nonlinear region of the dilatation curves represents a consequence of greater crystallization of plasma-sprayed HACs at 500°C to 800°C temperature interval. Table 6.1 lists the extent of dilatation values that are calculated from the dilatation curves cooling to about 100°C and significant crystallization-induced contraction after heat treatments have been demonstrated. This phenomenon can be recognized as a result of crystallization-induced contraction for these coatings. The CTE data of crystallized HACs at these heating temperatures are calculated from the slope of cooling stages, and the change in the CTE value also means that the effective crystallization temperature of plasma-sprayed HACs by postheat treatments should be higher than 600°C [64,120].

Compared with the as-sprayed HACs (Figure 6.6b), the cross-sectional images obtained from 600°C and 800°C crystallized HACs represent significantly cracking features, as indicated by the arrows in Figure 6.11. Figure 6.12 shows a typical SEM/SEI observation nearby these contraction-induced cracks of the heat-treated HACs in the range of 600°C to 800°C, and there is an obvious contrast within this area. Through the semiquantitative analysis of SEM/EDS, the light gray contrast denoted by "C" with a Ca/P ratio of 1.61 represents the occurrence of HA crystallization close to the contraction-induced cracks, and the dark gray

TABLE 6.1
Coefficient of Thermal Expansion (CTE, α) and Crystallization-Induced Contraction Ratio of Heat-Treated HACs

Heating Temperatures (°C)	α (×10^{-6} °C^{-1})[a]	Contraction Ratio (%)[b]
400	15.1	0.05
500	14.8	0.20
600	13.6	0.28
700	13.9	0.43
800	14.3	0.65

Source: Yang et al., *Mater. Trans.*, 48(2), 211–218, 2007. With permission.
[a] Values are measured from the slope of cooling curves to room temperature.
[b] Data obtained from total dilatation of the sample dimension after cooling.

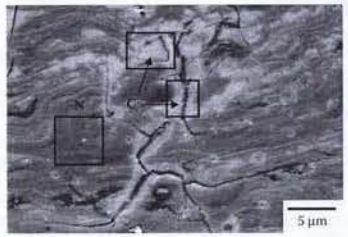

FIGURE 6.12
Enlarged cracks of heat-treated HACs, showing presence of crystallized (denoted by "C") and nonstoichiometric calcium phosphate (denoted by "N") regions that can be recognized by different contrast. (From Yang, C.W. and Lui, T.S., *Mater. Trans.*, 48(2), 211–218, 2007. With permission.)

region "N" with a low Ca/P atomic ratio of 1.35 represents a nonstoichiometric calcium phosphate region away from the "C" region. By incorporating the IOC and the thermal dilatometry results, therefore, it can be recognized that the formation and the propagation of enlarged cracks is due to the coating contraction during crystallization.

For biological applications, the dissolution rate of HA coatings is of interest because a rapidly dissolving coating may not remain on the implant for a sufficient time to allow full stabilization in bone or the desired tissue response in vivo. Ongoing development and optimization of the plasma-sprayed HACs are aimed at higher crystallinity coatings without sacrificing bonding strength. Although it is possible to evidently increase the crystallinity of plasma-sprayed HACs by postdeposition heat treatments in vacuum and in the air, heat treatments with temperatures over 600°C result in the degradation of mechanical properties with the significant formation of crystallization-induced cracks [101,120]. Therefore, it is indispensable to develop a lower-temperature treating process [58,59,63]; for example: a hydrothermal treatment with an abundant water vapor atmosphere that can simultaneously acquire higher crystallinity, good bonding strength, and biological responses without microstructural deterioration [121,122].

Hydrothermal Synthesis and Crystallization

The interest of synthesis of HA is linked with its importance as a major constituent of the inorganic component in human bones and teeth, and the characteristics of HA have significant effects on the subsequent products with HA being in the form of dense or porous structure in coatings or in composites. Since HA has been recognized as the best biocompatible ceramic material, there have been many reports on the biological aspects [6,7,15,123,124], and the fabrication processing of HA has progressed with the growing importance of the biological applications. A number of studies on the preparation of HA by various methods have been reported in the literature. Yoshimura and Suda et al. have reviewed the preparation for HA powders and grouped these methods into three categories, as listed in Table 6.2 [125–127]. Table 6.3 illustrates the chemical reactions of these processes [128]. Two

Exhibit A-4

Wang Yongsheng. Biological and Biomedical Coatings Handbook: Applications. Chapter 1: Sol-Gel Derived Hydroxyapatite Coatings on Metallic Implants: Characterization, In Vitro and In Vivo Analysis. 2017: 1-33.

Debasish Mondal
School of Materials Science and Engineering
Nanyang Technological University
Singapore

Soon-Eng Ong
Temasek Laboratories
Nanyang Technological University
Singapore

Nicholas P. Rhodes
Division of Clinical Engineering
School of Clinical Sciences
University of Liverpool
Liverpool, United Kingdom

Lei Shang
School of Mechanical and Aerospace Engineering
Nanyang Technological University
Singapore

Shree R. Singh
Department of Biological Sciences
Alabama State University
Montgomery, Alabama

Shi Su
Electronic Engineering, School of Engineering and Applied Science
Aston University
Birmingham, United Kingdom

Subbu S. Venkatraman
School of Materials Science and Engineering
Nanyang Technological University
Singapore

A. J. Walton
Scottish Microelectronics Centre
School of Engineering
Institute of Integrated Systems
University of Edinburgh
Edinburgh, United Kingdom

Yongsheng Wang
School of Mechanical and Aerospace Engineering
Nanyang Technological University
Singapore

Haitao Ye
Electronic Engineering
School of Engineering and Applied Science
Aston University
Birmingham, United Kingdom

Huang Yingying
School of Materials Science and Engineering
Nanyang Technological University
Singapore

Xia Yun
School of Materials Science and Engineering
Nanyang Technological University
Singapore

Sam Zhang
School of Mechanical and Aerospace Engineering
Nanyang Technological University
Singapore

James Zhenggui Tang
School of Applied Sciences
University of Wolverhampton
Wolverhampton, United Kingdom

1

Sol–Gel Derived Hydroxyapatite Coatings on Metallic Implants: Characterization, In Vitro *and* In Vivo *Analysis*

Wang Yongsheng

CONTENTS

Introduction

In modern society, the rapid development of biomedical engineering has provided considerable improvement on human quality of life. Biomaterials, as the main part of biomedical engineering, have attracted more and more attention regarding replacing a part or certain function of the body in a safe, reliable, economic, and physiologically acceptable manner

(Bronzino 2000). A vast array of manmade biomaterials, including metals, polymers, ceramics, and composites, have been widely developed during the past 90 years for the requirements of clinical applications. Each biomaterial has its own advantages and disadvantages for a specific application (Ratner et al. 1996; Smallman and Bishop 1998). In other words, the selection of a biomaterial for a specified case depends on the particular repair or replacement situation and the properties of related biomaterials. Herein, this chapter is limited to some issues related to load-bearing implants, such as hip joint replacement and teeth roots repair. The demands for these kind of load-bearing implants have increased enormously in the current industrial era due to increased injuries caused by accidents and the improvement of social awareness about the right of existence. According to the American Academy of Orthopedic Surgeons, for example, more than 120,000 total hip replacement operations are performed each year (Marsha, Leonard, and Randall 2000). As such, the development of reliable high-performance implants is greatly meaningful and valuable.

Many kinds of materials have been developed, including metals and alloys, polymers, ceramics, and composites, and are widely used in biomedical fields. However, no matter what the source, biomaterials must meet several criteria to perform successfully as load-bearing implants in orthopedic and dental applications (Hench 1998; Poitout 2004). First of all, they must be biocompatible, or able to function *in vivo* without eliciting any intolerable response in the body, either locally or systemically. On the other hand, those appropriate biomaterials must be able to withstand the often hostile environment of the body, and show better properties, such as resistance to corrosion and degradation, such that the body environment does not adversely affect material performance over the implant's intended performance lifetime. Furthermore, adequate mechanical properties, such as tensile/compressive strength, elastic modulus, and fatigue endurance, are also critical criteria for the selection of biomaterials to be used as devices intended to replace or reinforce load-bearing skeletal structures. In addition, they must be capable of reproducible fabrication to the highest standards of quality control at, of course, a reasonable cost. Biomaterials that meet these criteria are fundamental to the practice of orthopedic surgery and to ensuring the success of implantation.

Among all the suggested biomaterials, metallic biomaterials, such as Co–Cr–Mo alloys and titanium alloys, may be the most preferred selection for load-bearing implants due to their excellent mechanical properties (Table 1.1). However, all these metallic

TABLE 1.1

Mechanical Properties of Bone and Some Biomaterials

Types of Materials	Young's Modulus (GPa)	Ultimate Tensile Strength (MPa)	Tensile Elongation Rate (%)	Fracture Toughness (MPa $m^{1/2}$)
Alumina	420	282–551	<1	3–5.4
Hydroxyapatite (3% porosity)	7–13	38–48	–	3.7–5.5
Stainless steel	200	1000	10	100
Co–Cr alloys	230	450–1300	10–30	100
Ti–Al–V and c.p. Ti	100–140	500–1150	15–25	80
Mg and Mg alloys	41–45	225	–	–
PMMA	2.8	55	8	1.19
Cortical bone	3.8–11.7	82–114	–	2–12

Source: Leyens, C., Peters, M., *Titanium and Titanium Alloys: Fundamentals and Applications*, Wiley-VCH, Weinheim, 2003; Smallman, R.E., Bishop, R.J., *Modern Physical Metallurgy and Materials Engineering-Science, Process, Application*, Elsevier, 1998; Friedrich, H.E., Mordike, B.L., *Magnesium Technology*, Springer-Velag, Berlin, Germany, 2006; Ben-Nissan, B., Pezzotti, G., *Biomaterials*, 25, 20, 4971–4975, 2004. With permission.

biomaterials are bioinert and would release some undesired metal ions caused by corrosion in the human body's biological environment. Of the bioceramics, alumina, calcium phosphate, and bioglass in use are mainly because of their superior biocompatibility and bioactivity. However, their poor mechanical properties (e.g., tensile strength and fracture toughness) are serious design limitations for these materials when used in load-bearing implants (Table 1.1). Polymers, including polymethyl methacrylate (PMMA), polyethylene, polyurethane, etc., are widely used in plastic surgery, cardiovascular surgery, and other soft tissue surgery due to their properties of resilience and malleability, which are not at all suitable for load-bearing implants. Therefore, none of the three kinds of abovementioned biomaterials meet all the requirements of implants for hard tissue repair and/or replacement.

However, in view of the advantages and disadvantages of each kind of biomaterial, an advisable and practicable solution is to develop bioceramic-coated metallic implants. It is believed that such kinds of implants can do well in combining the desired biological properties of bioceramics and the excellent mechanical properties of metallic substrates. The bioceramic coating can also protect the metallic substrate from corrosion and serve as a barrier for the possible release of toxic metal ions into the human body. Among all these bioceramics, hydroxyapatite (HA) is the most suitable candidate to be used as a coating on the surface of metallic implants due to its chemical and biological similarity to human hard tissues (Boretoes and Eden 1984). HA coating cannot only improve the rate of osseointegration, but can also establish a high bone–implant interfacial strength by forming strong chemical bonds with the surrounding tissues (Vedantam and Ruddlesdin 1996; Roop, Kumar, and Wang 2002).

HA and HA Coating

HA is the main mineral component of human hard tissues (mainly bones and teeth), and provides storage for the control of calcium uptake and release for the human body (Aoki 1994). HA belongs to a class of calcium phosphate-based bioceramics with a chemical formula of $Ca_{10}(PO_4)_6(OH)_2$. The word "hydroxyapatite" consists of "hydroxyl" ion and "apatite," which is the mineral name. The stoichiometric Ca/P molar ratio is 1.67, and the calculated density is about 3.219 g/cm^3. HA crystallite possesses a hexagonal structure with the unit cell dimensions of: $a = b = 0.9432$ nm and $c = 0.6881$ nm (Hench and Wilson 1993; Kay, Young, and Posner 1964). The atomic structure of HA projected along the *c*-axis on the basal plane is shown in Figure 1.1.

It is well known that HA can be used as bone substitutes in orthopedics and dental treatment due to its biocompatibility and osteoconductive properties (Boretoes and Eden 1984). In order to meet the clinical requirements of different applications, HA has been developed well to be fabricated into different forms, such as particulates (solid, porous, or even hollow particles) in different sizes, blocks, and coatings (Wang et al. 2009). As for load-bearing implants, bulk HA seems not suitable because of the limitation of its mechanical properties (Hench and Wilson 1993; Bronzino 2000). There is a wide variation in the reported mechanical properties of synthesized HA, which strongly depended on the process applied with the HA sample preparation. For example, the compressive strength of synthesized HA ranges from 294 to 917 MPa (Park 1984). Other related mechanical properties are listed in Table 1.1. The mechanical properties of HA strongly influence their

FIGURE 1.1
Crystal structure of hydroxyapatite, viewed along *c*-axis. (From Kay et al., *Nature*, 204, 4963, 1050–1052, 1964. With permission.)

applications as implants. Therefore, the application of bulk HA as load-bearing implants is inevitably impracticable because of its poor fracture toughness (too brittle).

The most interesting property of HA in bone repair is its attractive bioactivity and strong ability to form direct chemical bonds with surrounding tissues. Therefore, HA-coated metallic implants could integrate the bioactivity of HA and the mechanical properties of metallic substrates for an ideal combination. Many techniques have been developed for the fabrication of HA coatings onto metallic implant surfaces. Commonly used methods include pulsed laser deposition (PLD) or laser ablation (Koch et al. 2007; Bao et al. 2005; Arias et al. 2003), hot isostatic pressing (HIP) (Onoki and Hashida 2006; Fu, Batchelor, and Khor 1998), thermal spraying techniques, including plasma spraying (Wang, Lu et al. 2007; Yan, Leng, and Weng 2003; Gu, Khor, and Cheang 2003), flame spraying (Cheang and Khor 1995; Oguchi et al. 1992), and high-velocity oxy-fuel combustion spraying (HVOF) (Lima et al. 2005; Khor et al. 2003), electrophoretic deposition (Wei et al. 2001; Xiao and Liu 2006), biomimetic coating (Reiner and Gotman 2009; Bharati, Sinha, and Basu 2005), sputtering coating (Pichugin et al. 2008; Ding 2003), and the sol–gel method (Haddow, James, and Van Noort 1999; Ak Azem and Cakir 2009; Avés et al. 2009). Each method has its own advantages and disadvantages in the coating properties, such as coating chemistry, phase composition, crystallinity, and mechanical properties, as well as biological properties. A comparison of these coating techniques is summarized in Table 1.2. Among all these

TABLE 1.2
Comparison of Different Methods for HA Coating Preparation

	Method	Coating Thickness	Advantages	Disadvantages	References
High temperature deposition techniques	Pulsed laser deposition	<5 μm	Coating crystalline and amorphous; dense or porous; active atmosphere conditions	Expensive; time-consuming; multiphase coating including α-TCP, β-TCP, TTCP besides HA and amorphous HA	(Koh et al. 2007; Bao et al. 2005; Arias et al. 2003; Katto et al. 2002)
	Hot isostatic pressing	0.2–2.0 mm	Produces dense coatings	Cannot coat complex substrates; high temperature required; thermal expansion mismatch; elastic property differences; expensive	(Onoki and Hashida 2006; Fu, Batchelor, and Khor 1998)
	Thermal spraying	30–200 μm	High deposition rates; can obtain various coating thickness and can be used for complex substrate shapes; low cost	High temperature induces decomposition; rapid cooling produces amorphous coatings	(Wang, Lu et al. 2007; Yan, Leng, and Weng 2003; Gu, Khor, and Cheang 2003; Cheang and Khor 1995; Oguchi et al. 1992; Lima et al. 2005; Khor et al. 2003)
Low temperature deposition techniques	Electrophoretic deposition	0.1–2.0 mm	Rapid deposition rates; can coat complex substrates	Non-uniform thickness; impurity; poor biological fixation to the metal substrates	(Wei et al. 2001; Xiao and Liu 2006; Ma, Liang et al. 2003; Stoch et al. 2001)
	Biomimetic coating	<30 μm	Low processing temperatures; can form bonelike apatite; can coat complex shapes; can incorporate bone growth stimulating factors	Time-consuming; requires replenishment and a constant pH of simulated body fluid	(Reiner and Gotman 2009; Bharati, Sinha, and Basu 2005; Barrere et al. 2001; Rigo et al. 2004)
	Sputter coating	<3 μm	Uniform coating thickness on flat substrates; dense coating	Ca/P ratio of the coating is higher than that of synthetic HA if RF magnetron sputtering is used; expensive; time consuming; producing amorphous coatings	(Pichugin et al. 2008; Ding 2003; Nelea et al. 2003; Nieh, Jankowsk, and Koike 2001; Cooley et al. 1992)
	Sol-gel method	<1 μm	Low processing temperature; can coat complex shapes; can obtain very thin coatings; higher purity and homogeneity; low cost	Some processes require controlled atmosphere and high sintering temperature	(Haddow, James, and Van Noort 1999; Ak Azem and Cakir 2009; Avés et al. 2009; Duran et al. 2004; Tkalcec et al. 2001; Montenero et al. 2000; Gross et al. 1998; Kim et al. 2005)

Source: Y. Yang et al., *Biomaterials*, 26, 3, 327–337, 2005. With permission.

coating techniques, the sol–gel method is commonly used for its advantages of composition homogeneity, low cost, and ease in operation (Zhang et al. 2006).

Sol–Gel Derived HA Coating

Brief Introduction of the Sol–Gel Technique

The sol–gel process is a chemical synthesis method generally used for the preparation of ceramics, glasses, and composites at much lower temperatures than other traditional methods, such as hot pressing and sintering (Hench and Wilson 1993). The use of the sol–gel method can be traced back to as early as the mid-1800s, and a fast-growing development of sol–gel applications has been achieved within the past three decades (Gupta and Kumar 2008; Wang and Bierwagen 2009). In the sol–gel process, the solution system involves a transition from a liquid "sol" into solid "gel" phase. The starting materials used in the preparation of "sol" are usually inorganic metal salts or metal organic compounds such as metal alkoxides. After a certain process with the sol (e.g., the coating of "sol" onto a substrate), followed by drying to remove residual organics and heat treatment, the "gel" is converted into dense materials (Klein 1988). Since the design of the sol–gel system and related sol–gel process can be controlled easily, this method has been employed to produce various products of desired sizes, shapes, and formats (e.g., particle, fiber, coating, bulk). The main advantages and important features of the sol–gel method can be summarized as (Wang and Bierwagen 2009; Klein 1988):

- Increased homogeneity due to the mixing at the molecular level
- Reduced processing temperature, frequently close to room temperature
- Substrate/mold shape-independent, since liquid precursors are used (such that complex shapes of products can be successfully fabricated)
- Easy mixing for multicomponent systems
- Use of different chemical routes (precursor selection)
- Possibility of producing materials with special properties (e.g., composition, crystallinity, morphology, and even composites)
- Low cost and easy operation

Today, sol–gel technology is widely used in the development of catalyst (Blum, Avnir, and Schumann 1999), nanomaterials (Răileanu et al. 2009), chemical sensors (Lin and Brown 1997), biosensors (Pastor et al. 2010), and electrochemical devices in diverse scientific and engineering fields, including the ceramic industry (Klein 1988), optical engineering (Gvishi et al. 1997), biomedical field (Gupta and Kumar 2008), and electronic industry (Dulay et al. 2002). Sol–gel technology shows great potential for the development of novel materials and devices in a broad range of applications.

Metallic Substrates

Because of the preliminary requirement of biocompatibility for a biomaterial, the number of metallic materials that can be considered for implants is limited. Metals and alloys used in clinical applications mainly include stainless steel, Co–Ni–Cr alloy, cast and

wrought Co–Cr–Mo alloy, commercially pure titanium (c.p. titanium), and titanium alloy (Ratner et al. 1996). Compared with other metals and alloys, however, c.p. titanium and titanium alloy–Ti6Al4V have been used as implant materials only for a short time. They have been widely used in clinical application and have a great potential prospect for medical applications due to their good biocompatibility, superior mechanical properties, and corrosion resistance (Leyens and Peters 2003). In the case of other metals as implants, the accumulation of toxic metal ions caused by dissolution and corrosion in the body's physiological environment often leads to severe pathological problems (Jaffe and Scott 1996). Furthermore, in comparison with cobalt chromium alloys, titanium and its alloy demonstrate a 33% increase in bonding strength to HA coating *in vitro*. Moreover, concerning the costs of semiproducts, Ti and its alloys belong to the same groups as stainless steel, whereas Co–Cr alloys are more expensive (Leyens and Peters 2003). Thus, titanium and its alloys with their favorable properties are more preferable for medical applications compared to other metallic materials.

Recently, magnesium and magnesium alloys, as the lightweight metals (density ~1.75g/cm^3), have been proposed as biodegradable implants for orthopedic and trauma surgery due to their outstanding biocompatibility, biodegradability, and mechanical properties (Witte 2010; Friedrich and Mordike 2006). According to Wolff's law, Mg alloys are most preferred because of the similarity of Young's modulus between Mg alloys and human bones (cf. Table 1.1). Such kind of similarity can effectively avoid the stress shielding effect, leading to enhanced stimulation of new bone growth and remodeling (Zberg, Uggowitzer, and Löffler 2009). Noticeably, because of the bioresorbable characteristic, Mg alloy-based implants are strongly expected as biodegradable implants (e.g., coronary stent) rather than the permanent ones. Therefore, it is still questionable for Mg alloys to be used as load-bearing implants for hard tissue repair or replacement.

Precursors for Sol–Gel Derived HA Coating

Theoretically, any precursor able to form reactive inorganic monomers or oligomers can be used for sol–gel process to synthesize the corresponding inorganic products. However, in order to obtain sol–gel derived coatings with the desired quality, the selection of related precursors (as well as the designed sols) should satisfy some basic requirements (Klein 1988; Gupta and Kumar 2008):

(1) Must be soluble in the selected reaction media and reactive enough to participate in the gel forming process.
(2) The precursors should be stable (do not produce any unwanted by-product).
(3) The sols containing precursors should have certain viscosity and can wet the substrate well to produce an overall homogeneous deposited layer.
(4) Uniform and long-term stability of the sols is possible.
(5) Easy removal of unused ions or organic groups to obtain a coating with pure phase and uniform surface morphology.

A number of calcium and phosphate precursors have been employed for sol–gel synthesis of HA coatings on metallic implant surfaces at a low temperature. An overview of different calcium and phosphate precursors commonly used for the preparation of HA coatings is listed in Table 1.3. Due to the difference in chemical activity of different precursors, the temperature required to produce the apatite structure depends largely on the chemical

TABLE 1.3

Overview of Different Calcium and Phosphate Precursors for Preparation of HA Coatings

Calcium Precursor	Phosphate Precursor	References
Calcium nitrate tetrahydrate ($Ca(NO_3)_2 \cdot 4H_2O$)	Diphosphorous pentoxide (P_2O_5); Ammonium hydrogen phosphate ($(NH_4)_2HPO_4$); Ammonium dihydrogen phosphate; Triethyl phosphite; Triethyl phosphate (TEP); Phosphoric acid (H_3PO_4); *n*-Butyl acid phosphate (*n*-BAP); Triethyl phosphate	(Weng, Han et al. 2003; Montenero et al. 2000; Hsieh, Perng, and Chin 2002; You, Oh, and Kim 2001; Cavalli et al. 2001; Liu, Yang, and Troczynski 2002; Kim et al. 2004; Manso, Ogueta et al. 2002; Manso, Langlet et al. 2002; Hwang et al. 2000; Wang, Chen, and Wang 2009; Gan and Pilliar 2004; Weng and Baptista 1998)
Calcium acetate monohydrate ($Ca(OA\text{-}c)_2 \cdot H_2O$)	Diethyl hydrogen-phosphonate ($(C_2H_5)_2HPO$);	(Ben-Nissan, Milev, and Vago 2004; Balamurugan, Kannan, and Rajeswari 2002)
Calcium diethoxide	Triethyl phosphite; Diethyl hydrogen-phosphonate ($(C_2H_5)_2HPO$); Phosphoric acid (H_3PO_4)	(Ben-Nissan, Milev, and Vago 2004; Haddow, James, and Van Noort 1999; Chai and Ben-Nissan 1999)
Calcium hydroxide ($Ca(OH)_2$)	2-Ethylhexyl-phosphate	(Metikos-Hukovic et al. 2003; Tkalcec et al. 2001)

nature of the precursors (Haddow, James, and Van Noort 1996; Liu, Troczynski, and Tseng 2001). With the use of different precursors and processing conditions, the expected properties (chemical composition, phase components, crystallinity, thickness, morphology, porosity, etc.) of these HA coatings can be successfully achieved and well controlled.

Chemical and Physical Properties of Sol–Gel Derived HA Coating

Phase Composition

According to the processing temperature, all coating methods can be classified into two groups, low-temperature and high-temperature deposition techniques, as shown in Table 1.2. Even though the sol–gel method is classified into the low-temperature group, almost all the HA coatings prepared with this method must be treated with an essential sintering or heat treatment step at an elevated temperature. (Generally, the temperature is lower than 1000°C.) (Chen et al. 2005). Such a heat treatment process is usually required to remove the unwanted chemical components (to obtain the final HA coating) or to increase the coating crystallinity. However, the following decomposition reactions may also occur during the heat treatment (Ogiso, Yamashita, and Matsumoto 1998; Senamaud et al. 1997):

$$Ca_{10}(PO_4)_6(OH)_2 \rightarrow 2Ca_3(PO_4)_2 + Ca_4(PO_4)_2O + H_2O\uparrow$$

$$Ca_{10}(PO_4)_6(OH)_2 \rightarrow 3Ca_3(PO_4)_2 + CaO + H_2O\uparrow$$

Generally, the final coating is a pure HA coating or with a small amount of impurity phases, such as CaO, and/or TCP, OCP, carbonated HA, $CaCO_3$ (Montenero et al. 2000; Hsieh, Perng, and Chin 2002; Wang, Chen, and Wang 2009; Weng and Baptista 1998). Figure 1.2 shows a typical HA phase with small amount β-TCP (less than 5%) of sol–gel

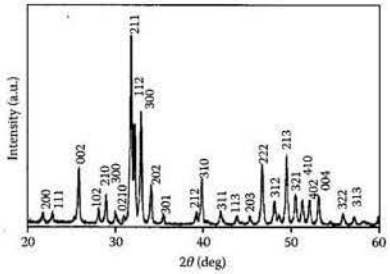

FIGURE 1.2
Phase composition of sol–gel derived HA coatings on Ti6Al4V substrate after calcination at 900°C. (From Montenero et al., *Journal of Materials Science*, 35, 11, 2791–2797, 2000. With permission.)

derived HA coatings on Ti6Al4V after being calcined at 900°C by using $Ca(NO_3)_2 \cdot 4H_2O$ and $(NH_4)_2HPO_4$ as corresponding precursors (Montenero et al. 2000).

On the other hand, the phase purity and the degree of crystallinity of sol–gel derived HA coatings is reported to depend on the kind of precursors used for the preparation of HA coatings (Haddow, James, and Van Noort 1996). For instance, Gan and Pilliar (2004) pointed out that the HA coating prepared with an organic route (precursors: calcium nitrate tetrahydrate and triethyl phosphite) possesses higher crystallinity than that obtained with an inorganic route (precursors: $Ca(NO_3)_2 \cdot 4H_2O$ and ammonium dihydrogen phosphate). Moreover, besides the selection of temperature, some other factors, including time of heat treatment, heating rate, and surrounding atmosphere, are also quite important to control the final phase composition and crystallinity (Chen et al. 1997; Wang, Chen, and Wang 2009; Hsieh, Perng, and Chin 2002). For instance, water molecules in the firing atmosphere could promote HA crystallization, whereas in a dry atmosphere TCP and TTCP are more stable than HA in a higher temperature (Chen et al. 1997). Comparatively, the phase composition of HA coatings produced by the sol–gel method is simpler than those coatings obtained by using high temperature deposition methods, which usually contain a certain amount of other impure phases, such as amorphous hydroxyapatite (ACP), oxyapatite, tricalcium phosphate (TCP), tetracalcium phosphate (TTCP), and calcium oxide (CaO) (Ong et al. 2006; Yan, Leng, and Weng 2003; Lima et al. 2005).

No matter the impure phases, all have crucial effects on the performance of coated implants, especially on the dissolution behavior of the coatings (Sun et al. 2001; You, Oh, and Kim 2001; Yang, Kim, and Ong 2005). All of the others' phases in the coating have larger solubility than that of HA (Ducheyne, Radin, and King 1993; Wang, Lu et al. 2007; Khor et al. 2003). Although the faster dissolution produces a supersaturated environment, which allows physiologically produced HA to precipitate on the coating and enhance the bone ingrowth, it also leads to the serious resorption or degradation of the coatings, and even to the failure of the implants (Cheng, Zhang, and Weng 2007; Kim, Kim, and Knowles 2005). On the other hand, the impure phase, CaO, has no biocompatibility and dissolves significantly faster than TCP. Thus, it is a detrimental phase that should be avoided (Wang, Chen et al. 2008; Sun et al. 2001). As such, both the purity and the crystallinity of the coating should be strictly controlled in order to obtain the expected effective HA coating layers.

The smaller amount of other phases, the higher degree of crystallinity, and the lower the dissolution rate, the better the performance of the implants, and vice versa. Thereby, from the viewpoint of phase purity, the sol–gel method is preferred in depositing the expected HA coatings on metallic substrates.

X-ray diffraction (XRD) is a powerful, nondestructive analysis tool and has been widely used as a means of determining the phase composition and crystallinity of the HA coatings. That is, it estimates the percentage of crystallinity and identifies the secondary phases generated during the preparation of HA coatings from the relative peak intensity of different phases (Löbmann 2007). The new phases can be identified from the plot of the intensity vs. 2θ, or from the lattice parameter change determined by XRD results. Also, other analytical techniques, such as differential thermal analysis (DTA)/differential scanning calorimetry (DSC), Fourier transform infrared spectroscopy (FTIR), can help in this analysis.

Surface Chemistry and Composition

The surface chemistry of sol–gel derived HA coatings, as one of the most significant factors for the coating in a clinical application, has received considerable attention because of its dominant role in osseointegration (Hench and Wilson 1993; Kačiulis et al. 1998). X-ray photoelectron spectroscopy (XPS) or electron spectroscopy for chemical analysis (ESCA) is the most famous technique for the analysis of surface chemistry, since it can detect all elements except hydrogen and helium with high sensitivity even for the trace amount of contaminants in the materials (Briggs and 2003; Brundle, Evans, and Wilson 1992). XPS is an important analytical tool in the area of coatings/thin films, and it can provide useful information, including compositions (elements), chemical states, and coating thickness. Based on the survey and narrow scan, the possible elements can be accurately ascertained since each element has its own characteristic binding energy. The chemical state (valence) or bonding information of each element can be determined through the shift of corresponding peak position (binding energy).

There are two main properties of concern regarding surface chemistry: the composition of the HA coating and the chemical status of the elements existing in the HA coating (Kačiulis et al. 1999). As for the composition of HA coatings, it is mainly the three elements of Ca, P, and O and their concentration (commonly described as Ca/P and O/Ca molar or weight ratio). The Ca/P and O/Ca peak ratios can help distinguish and quantify different Ca/P phases in the mixtures. With respect to the stoichiometry of the HA coatings, the Ca/P ratios for the sol–gel samples were in good agreement with the stoichiometric values compared with other coating techniques (Massaro et al. 2001; Metikos-Hukovic et al. 2003). However, as Haddow, James, and Van Noort (1996) have pointed out, the Ca/P ratio could have a great difference in response to different precursors selected. For example, the Ca/P ratio was 1.46 for the inorganic-route precursors and 2.10 for the organic-route precursors in the work of Gan and Pilliar (2004). All these changes on the Ca/P ratio can be demonstrated by other analytical methods, such as XRD and FTIR. As for the chemical states analysis, it is becoming more and more important in the biological development. Each element has the "fingerprint" characteristics that can be determined by some analytical techniques (Kačiulis et al. 1998). According to the analysis, some new phases can be determined. For HA coatings, many studies have been done on this point. Generally, Ca2p (or $Ca2p_{1/2}$ and $Ca2p_{3/2}$), P2p, and O1s are the most studied for determining the chemical properties of the coating. For example, in Figure 1.3, the O1s peaks of the HA coatings deposited by different methods are presented (Massaro et al. 2001). As indicated, peak 1 is the characteristic O1s peak in HA structure with a binding energy of 531.4eV; peak 2 is

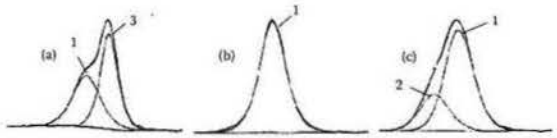

FIGURE 1.3
O1s spectra (XPS) of HA coatings prepared by different methods ([a] sol–gel coating; [b] sputtered coating; [c] plasma-sprayed coating). Peak 1 is the characteristic O1s peak in HA structure with a binding energy of 531.4eV; peak 2 is attributed to the O1s in adsorbed water; peak 3 is the O1s coming from TiO_2. (From Massaro et al., *Journal of Biomedical Materials Research*, 58, 6, 651–657, 2001. With permission.)

attributed to the O1s in adsorbed water, whereas peak 3 is the O1s coming from TiO_2. As such, according to the binding energy of a specified element, it is quite easy to find out what kind of phase/compound of this element is in. Table 1.4 summarizes the binding energy levels of core elements in some calcium-containing salts. Importantly, based on the XPS analysis (especially the narrow scan screening), the determination of trace elements in the coating is critical for the investigation and evaluation of new biomaterials (Kačiulis et al. 1999).

Surface chemistry and composition can also be analyzed by FTIR. The FTIR technique is rapid and nondestructive, requires no vacuum, and is applicable to samples of any dimension and even to those with curvature (Kazarian et al. 2004). The chemically specific information contained in the unique "fingerprint" region of the IR spectrum allows one to distinguish different chemical groups and even different materials. In HA, compound groupings, such as hydroxyl bands (OH groups), carbonate bands (CO_3 groups), and phosphate bands (PO_4 groups), are usually quantified by FTIR (Stoch et al. 2005; Vijayalakshmi, Prabakaran, and Rajeswari 2008). Crystalline HA generates two characteristic OH bands at about 3570 and 630 cm^{-1} (Weng and Baptista 1999; Stoch et al. 2000). Sometimes they are absent in FTIR spectra, and some authors attribute this missing OH modes to a perturbation of hydroxyl stretching and bending modes on the apatite surface by the hydrogen

TABLE 1.4

XPS Binding Energy Values of Main Elements in Some Calcium-Containing Salts

	Binding Energy (eV)			
Phase	**Ca $2p_{1/2}$**	**Ca $2p_{3/2}$**	**P 2p**	**O 1s**
HA	351.0–351.2	347.2–347.5	133.3–133.5	531.3–531.6
α-TCP[a]	350.7	347.2	133.3	531.0
β-TCP[a]	350.6	347.0	133.1	530.9
ACP[a]	350.6	347.1	133.1	531.1
$CaCO_3$[b]	350.1	346.5	–	533.9 (O_I) 535.6 (O_{II})

Source: Amrah-Bouali et al., *Biomaterials*, 15, 4, 269–272, 1994; Lu et al., *Anal. Chem.*, 72, 13, 2886–2894, 2000; Chusuei, C.C., *Anal. Chem.*, 71, 1, 149–153, 1999; Yan et al., *Biomaterials*, 24, 15, 2585–2592, 2003; Battistoni et al., *Surf. Interface Anal.*, 29, 11, 773–781, 2000. With permission.

[a] Peak positions are calibrated by setting the adventitious C1s to 284.7eV.

[b] Powder form in calcite phase.

bonding of water molecules to the surface OH ions. The adsorbed water yields a broad band in the 3000–3500 cm^{-1} range and at about 1650 cm^{-1} (Stoch et al. 1999).

The phosphate group has a T_d symmetry resulting in four internal modes' being IR active: v_3 asymmetric stretching mode of vibration characterized by a strong, complex band in 1000–1150 cm^{-1} range and a medium intensity band at about 963 cm^{-1} due to v_1 symmetric stretching vibration (Tkalcec et al. 2001). The v_4 bending vibration of PO_4 is characterized by bands located at 560–610 cm^{-1}. A weak band at 430–463 cm^{-1} corresponds to v_2 bending vibration (Stoch et al. 1999).

The FTIR spectrum is very sensitive to the carbonate (CO_3^{2-}) group; even a very small amount of carbonate can be detected. Generally, carbonate can be incorporated into the HA structure by replacing the OH group (type A substitution) or by replacing PO_4 groups (type B substitution) (Stoch et al. 1999). The presence of CO_3^{2-} as well as its position can be well determined by FTIR: type A substitutions have a singlet band at ~880 cm^{-1} (out-of-plane deformation, *v2*) and a doublet band at about 1450 and 1545 cm^{-1} (asymmetric stretching vibration, *v3*); the co-occurrence of CO_3^{2-} absorption peaks recorded at 873 cm^{-1} (*v2*), 1412 and 1465 cm^{-1} (*v3*) indicates the incorporation of CO_3^{2-} groups into HA lattice structure through the B-type substitution (Tkalcec et al. 2001).

Along with FTIR, Raman spectroscopy (RS) is another powerful analytical technique for the determination of molecular vibrations. The vibration activity is different in FTIR and RS due to the symmetry dependence of some chemical groups. In other words, some vibrations are both FTIR and RS active, but others are only FTIR or RS active. Therefore, complementary detailed information about the molecular vibrations could be well characterized by combing the FTIR and RS analysis. A detailed report about the application of RS in characterizing HA samples can be found in some related references (Mihály et al. 2009; Silva and Sombra 2004).

Surface Morphology

Surface morphology is another important coating characteristic that influences its performance. Surface morphology of the HA coating also affects the dissolution and bone apposition on the coating or bone ingrowth, because the coating surface, once implanted, is directly in contact with the bone and body fluid, thus playing a major role in the formation and maintenance of tissue integrity (Ben-Nissan, Milev, and Vago 2004). Scanning electron microscopy (SEM) and atomic force microscopy (AFM) are the most widely used techniques to characterize the surface morphology of HA coatings in practice.

In sol–gel technology, the solvent can be evaporated to leave a solid with a certain level of fine porosity. So, generally, according to the process characteristics of sol–gel technique, it is a common phenomenon that the sol–gel derived HA coating is a homogeneous, but rough with micro pores (about a few hundred microns) and even micro cracks (Massaro et al. 2001; Montenero et al. 2000). Figure 1.4 shows a typical SEM micrograph (Figure 1.4a, precursors: $Ca(NO_3)_2{\bullet}4H_2O$ and P_2O_5) and AFM image (Figure 1.4b, precursors: $Ca(NO_3)_2{\bullet}4H_2O$ and $(NH_4)_2HPO_4$)) about the surface morphology of sol–gel derived HA coating on the titanium and titanium alloy substrates. The coating looks quite uniform with a certain degree of porosity. The surface morphology of sol–gel derived HA coatings can be controlled by sol–gel parameters, such as different precursors (Guo and Li 2004; Gan and Pilliar 2004), post heat treatment (Hwang et al. 2000), the addition of chemical additives (Weng, Han et al. 2003), and surface roughness of the substrates as well as the thickness of the coating (You, Oh, and Kim 2001). Therefore, a customized surface morphology can be obtained according to the different requirements in practical application.

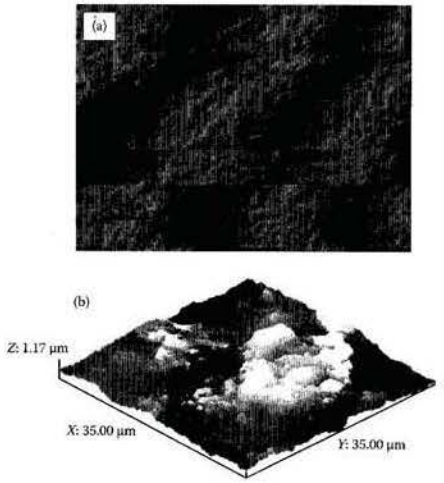

FIGURE 1.4
Surface morphology of sol–gel derived HA coating on Ti and Ti-alloy substrates: (a) SEM micrograph; (b) AFM image. (From *Massaro et al., Journal of Biomedical Materials Research*, 35, 11, 2791–2797, 2000. With permission.) The surface is uniform with certain degree of porosity.

Interfacial Analysis

Interfacial failure is reported to be one of the most predominate failure modes of HA-coated implants (Cheng et al. 2005). Generally, the interfacial adhesion of a sol–gel derived coating–substrate system comes from two aspects: the mechanical interlock and the chemical bonding. As for the mechanical interlock, surface pretreatment of metallic substrate is commonly applied, such as surface polishing and chemical treatment (Balakrishnan et al. 2007). However, it is believed that the contribution of mechanical interlock to adhesion is quite limited. The formation of certain chemical bonds at/near the coating substrate is strongly desired to improve the adhesion properties. Interfacial analysis (usually, the distribution of elements at/near the interface between the coating and substrate) is always carried out to provide the necessary bonding information about adhesion property. Time-of-flight secondary ion mass spectrometry (ToF-SIMS) (Cheng et al. 2005), glow discharge optical emission spectroscopy (GDOES) (Qi et al. 2008), and electron dispersive x-ray spectroscopy (EDS/EDX) (Zhang et al. 2006) are commonly used techniques for determining element distribution near the coating–substrate interface.

As a typical result, Figure 1.5 shows the SIMS composition depth profiles analysis of a sol–gel derived HA coating on Ti6Al4V substrate (precursors: $Ca(NO_3)_2{\bullet}4H_2O$ and P_2O_5). According to the distribution of the concerned elements along the cross section (i.e., Ca, O, P, and Ti), the cross section can be divided into three regions at/near the interface: the substrate (Rs) region, the transitional region (Rt), and the coating region (Rc). The transitional

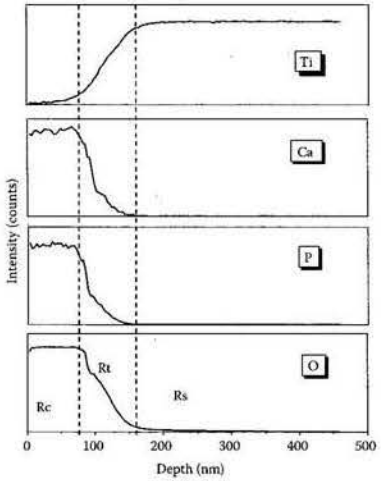

FIGURE 1.5
SIMS composition depth profile analysis of HA–Ti6Al4V interface. Three regions can be divided for cross sections: coating region (Rc), a transitional region (Rt), and substrate region (Rs). Within the transitional region, Ca and P concentrations decrease drastically from the coating toward the substrate, while the O concentration decrease gradually toward the substrate; Ti concentration increases gradually from transitional region to the substrate.

region (Rt) has a thickness of about 85 nm, and within the transitional region, the Ca and P concentrations decrease drastically toward the substrate, whereas O element decreases gradually from the coating region (Rc) to the substrate region (Rs), and the concentration of Ti element increases gradually from the transitional region (Rt) to the substrate region (Rs). It can be speculated from the existence of the transitional region and the distribution of the elements along the cross section that certain Ti–P–Ca–O compounds have formed at/near the interface (Montenero et al. 2000; Hsieh, Perng, and Chin 2002).

Mechanical Properties of Sol–Gel Derived HA Coating

Pull-Out Tensile Adhesion Strength and Interfacial Shear Strength

In view of the successful implantation as well as long-term stable performance, mechanical properties are important for HA-coated metallic implants. Among all the mechanical properties required, adhesion strength (or bonding strength) between the coating and metallic substrate is the most important property for those load-bearing implants. Two kinds of pull-out based methods are widely used to evaluate the adhesion strength: uniaxial pull-out tensile test method (as shown in Figure 1.6a) for the determination of tensile adhesion strength and shear pull-out test (Figure 1.6b) for the measurement of shear adhesion strength (Zhang et al. 2008; Ma, Wong et al. 2003; Implants for Surgery-

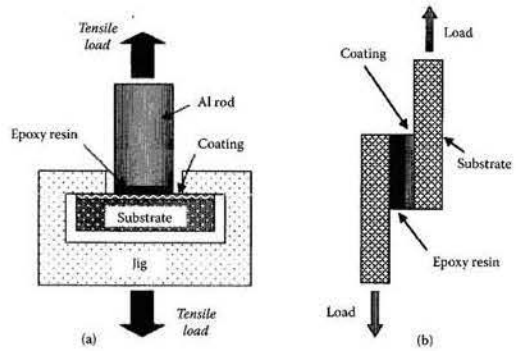

FIGURE 1.6
Schematic diagrams of pull-out testing methods for assessing of adhesion strength: (a) tensile adhesion strength test (from Zhang et al., *Thin Solid Films*, 516, 16, 5162–5167, 2008; with permission); (b) shear adhesion strength test.

Hydroxyapatite—Part 4: Determination of Coating Adhesion Strength 2002). Both of these two methods are tested using epoxy or super glues to fix the coating onto the counterpart. Accordingly, the bonding strength will be highly influenced by many factors, such as the uniformity of the epoxy layer, penetration depth of the glues, porosity and thickness of the coating, and alignment of the applied force. Therefore, it could be imagined that a wide range (large deviation) of adhesion strengths would be obtained, even for the coatings deposited with the same deposition method. According to the documented results, the adhesion strengths of HA coatings on metallic substrates prepared with different deposition techniques were summarized in Table 1.5. As stipulated by ISO standards (ISO13779), the recommended bonding strength (pull-out tensile test) should be not less than 15 MPa (Implants for Surgery-Hydroxyapatite—Part 2: Coatings of Hydroxyapatite 2000). The sol–gel method is thus acceptable for the preparation of HA coatings from the standpoint of adhesion (cf. Table 1.5).

More importantly, the adhesion strength after *in vitro* or even after *in vivo* tests is quite crucial in estimating the survivability of HA coating on implant surfaces. As reported, *in vivo* studies suggested that the failure of plasma sprayed HA-coated metallic implants mainly occurs at the coating–substrate interface, and the failure probability at this interface increased with the period of implantation because the strength of the coating–bone interface tends to increase with more healing time (Sun et al. 2001; Albrektsson 1998). Such degradation of adhesion is generally attributed to the dissolution behaviors related to the coating properties (e.g., impurity phases [TCP, CaO, etc.], crystallinity, cracks) (Lima et al. 2005), which would impair the mechanical properties (especially, adhesion strength) of the coating. Detailed description and discussion about the adhesion properties after *in vitro* and/or *in vivo* tests can be found in some related reports (Aksakal, Gavgali, and Dikici 2009; Zhang et al. 2008; Kim et al. 2005; Albrektsson 1998).

Noticeably, cohesion failure (failure within the coating layer) was always observed in those pull-out based tests (Figure 1.7), indicating that the obtained results are not the actual

TABLE 1.5
Adhesion Strength of HA Coatings Deposited with Different Deposition Methods

	Pulsed laser Deposition	Hot Isostatic Pressing	Thermal Spraying	Electrophoretic Deposition	Biomimetic Coating	Sputter Coating	Sol–Gel Method
Tensile adhesion strength (MPa)	30–58	–	10–60	<14	<15	>60	15–60
Shear adhesion strength (MPa)	–	4.0–5.5	11–26.8	8–23	<9.5	–	<17
References	(Wang et al. 1997; García-Sanz et al. 1997)	(Onoki and Hashida 2006)	(Li, Khor, and Cheang 2002; Ding et al. 2001; Gu, Khor, and Cheang 2003; Yang, Chang, and Lee 2003; Li, Khor, and Cheang 2002; Kweh, Khor, and Cheang 2000)	(Han et al. 2001; Xiao and Liu 2006; Wei et al. 2001)	(Ma, Wong et al. 2003; Pena et al. 2006)	(Ding, Ju, and Lin 1999; Ding 2003)	(Balamurugan et al. 2006; Kim et al. 2004; Hsieh, Perng, and Chin 2002)

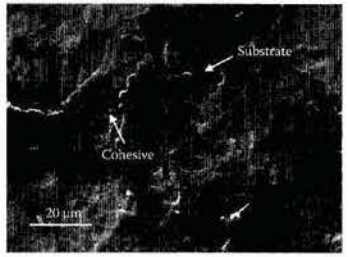

FIGURE 1.7
Typical fracture surface of fluoridated HA coatings after pull-out tensile test: a mixed failure mode is commonly observed, which consists of adhesion failure occurring at the coating–substrate interface, cohesion failure occurring within the coating, and gluing failure occurring at the epoxy-coating interface. (From Zhang et al., *Thin Solid Films*, 516, 16, 5162–5167, 2008. With permission.)

adhesion strengths between the coating and substrate (Zhang et al. 2008). In other words, those pull-out based testing methods are highly influenced by the coating characteristics and infiltration of epoxy, resulting in limited information about the adhesion properties at the coating–substrate interface. Therefore, other evaluation techniques/methods (e.g., scratch test) are necessary to get a sound evaluation of adhesion properties.

Evaluation of Interfacial Shear Strength

Generally, for bioceramic-coated, load-bearing implants, the adhesion behaviors of coating–substrate interface can be roughly classified into tensile and shear adhesion. Therefore, besides the tensile strength, the interfacial shear strength also serves as a crucial factor for those implants used as tooth root and hip joint replacement. Although certain quantitative evaluations have been done with the commonly used pull-out shear test, in viewing the intrinsic drawbacks of the "pull-out test," those obtained shear strength should be the "cohesive shear strength" rather than the "interfacial shear strength" (Li, Khor, and Cheang 2002). However, the shear lag strain approach described by Agrawal and Raj (Agrawal and Raj 1989, 1990), which utilizes the regular crack patterns obtained through the designed tests, appears useful and relatively straightforward for the determination of interfacial shear strength. Basically, this method relies on the development of transverse crack patterns in a brittle coating when the relatively ductile supporting substrate is plastically deformed under an applied uniaxial load. This crack behavior can be adequately described by a shear-lag analysis that directly relates crack density to the load transfer capabilities of the interface, and this shear lag theory predicts the establishment of a steady state of constant crack density observed at relatively high strain levels. For a coating of thickness t, the interfacial shear strength τ_{max} can be determined by a simplified expression (Agrawal and Raj 1989):

$$\tau_{max} = \sigma_f \frac{\pi t}{1.5\lambda}$$

where λ is the average steady-state crack spacing and σ_f is the tensile strength of the film (i.e., the coating). σ_f can be determined experimentally by measuring the maximum elastic strain, ε_f, of the coating (at which the initial formation of cracks is detected):

$$\sigma_f = \varepsilon_f E_f$$

where E_f is the Young's modulus of the coating.

The interfacial shear strength evaluated with the shear lag strain method are reported to be at least an order of magnitude greater than the pull-out shear strengths reported for plasma-sprayed and high-velocity oxy-fuel sprayed HA (Li, Khor, and Cheang 2002; Brossa et al. 1994; Gan, Wang, and Pilliar 2005). On the other hand, the reported interfacial shear strength between the coating surface and surrounding tissues *in vivo* was about 16.65 MPa after a 24-implantation (Yang et al. 1997). Therefore, from the standpoint of interfacial shear strength, sol–gel derived HA coatings appear quite promising for long-term load-bearing implants. However, it should be noted that the determination of interfacial shear strength using the shear lag analysis requires a limited film thickness, hence the low transverse residual stress within the coating.

Scratch Test

The scratch test is generally accepted as one of the simple and popular methods in assessing the adhesion properties of coating–substrate interface (Arias et al. 2003; Zhang et al. 2006). Basically, it is carried out by drawing a diamond tip over the coating surface to produce a scratch. The applied normal load is increased linearly until a critical load is reached at which the adhesion failure is induced at the coating–substrate interface. Thus, the critical load can be taken as a semiquantitative measurement of the coating–substrate adhesion strength, and the failure mode can provide further qualitative information upon the coating–substrate interface (Zhang et al. 2006). Figure 1.8 shows a typical scanning scratch

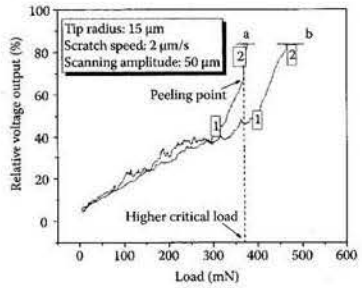

FIGURE 1.8
Coefficient of friction in terms of relative output voltage as a function of normal load in the scratch test of sol–gel derived coating: (a) HA coating, (b) fluoridated HA coating. At point 1, the indenter starts to plough into the coating, resulting in a steeper increase in coefficient of friction; at point 2, the indenter completely peels off the coating and scratches onto the substrate causing an abrupt increase in friction. (From Zhang et al., *Surface and Coatings Technology*, 200, 22–23 Spec. Iss., 6350–6354, 2006. With permission.)

curve of sol–gel derived HA and fluoridated HA coatings. The curves indicate a good adhesion between the coating and substrate, and reveal that the coating–substrate interfacial failure mode changes from brittle to ductile with fluorine ion were incorporated into the HA lattice structure (Zhang et al. 2006). That is to say, the scratch test can provide a lot of remarkable information about the coating–substrate interface, even though some of the data are just qualitative. Therefore, by considering the features of the pull-out tensile test, shear lag strain method, and scratch test, the combination of these three testing methods could be more helpful in getting a comprehensive understanding of the coating–substrate adhesion properties.

Toughness of Sol–Gel Derived HA Coating

Fracture toughness serves as a decisive factor in evaluating the functionality of coated implants and determines the level to which the material can be stressed in the presence of cracks, or equivalently, the magnitude of cracking that can be tolerated at a specific stress level. Regarding the interfacial fracture toughness of HA-coated Ti6Al4V implants, Filliaggi, Coombs, and Pilliar (1991) used a short bar chevron notch test and obtained the K_R values of 0.6–1.41 MPa $m^{1/2}$. By using a single-edge notch-bend test, Tsui, Doyle, and Clyne (1998) reported some similar values of K_{IC} of about 0.28–1.1 MPa $m^{1/2}$. In addition, an indentation based method was also employed by Li, Khor, and Cheang (2002), and the corresponding value was reported as 0.48 MPa $m^{1/2}$ for K_{IC}.

However, for HA coatings prepared with the sol–gel method, indentation-based energy analysis method is preferred due to the limitation of the thickness of HA coating. Theoretically, the energy approach examines the energy difference before and after the cracking, which is responsible for the fracture of the coating. The energy difference would then be the energy release in the through-thickness cracking in the coating. The energy release can be obtained from a "step" that would be observed in the load–displacement curve for the indentation. Therefore, based on the energy difference before and after the crack generation, the fracture toughness of the coating can be determined as (Li, Diao, and Bhushan 1997):

$$K_{IC} = \left[\frac{\Delta U}{t} \frac{E_f}{2\pi C_R\left(1-\nu_f^2\right)}\right]$$

where ν_f is the Poisson's ratio of the coating, $2\pi C_R$ is the crack length in the coating plane, t and E_f are the coating thickness and elastic modulus, respectively, and ΔU is the strain energy difference before and after cracking. Figure 1.9 displays a typical load–displacement curve of indentation together with the corresponding SEM micrograph, which can be used readily for toughness evaluation of the HA coating (Zhang et al. 2008).

Residual Stress Measurement

Residual stress is inherently induced in any coating deposited by a method with a high temperature process due to the differences in the thermal properties between the coating and the substrate. Residual stress in the coating might vary with coating thickness, deposition parameters, etc. Therefore, both tensile and compressive residual stresses have been

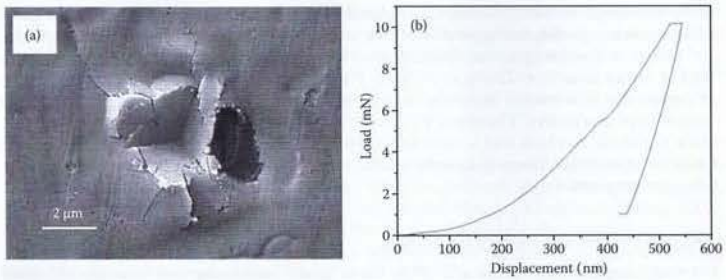

FIGURE 1.9
(a) SEM micrograph of nanoindentation of sol–gel derived HA coating and (b) its corresponding load–displacement curve.

reported with different values. For instance, tensile residual stresses of 200–450 and 20–40 MPa were reported by Brown, Turner, and Reiter (1994) and Tsui, Doyle, and Clyne (1998), respectively. In contrast, a compressive residual stress of about 35–78 MPa was reported by Yang, Chang, and Lee (2003), and Yang and Chang (2005). The differences may result from the coating preparation method and process, as well as the method employed for the measurement of residual stress.

Considerable efforts have been made in recent years to understand and measure the residual stresses developed during the preparation of HA coatings (Tsui, Doyle, and Clyne 1998; Yang and Chang 2005). Popular among the various methods is the XRD method, which is a nondestructive and simple technique for residual stress measurement. However, since this method is based on the shift of the peaks in XRD patterns, the use of this method is limited by some factors of the coating, such as surface roughness, phase composition, and especially the doping of some expected ions. Considering the intrinsic characteristic of residual stress, a "wafer curvature method" was developed to evaluate residual stress, especially for sol–gel derived coatings (Watanabe et al. 2002; Xie and Hawthorne 2003): on a relatively thin substrate, the residual stress distributed in the coating layer will cause the substrate to bend, and the induced curvature for the coated substrate depends on the force, the elastic properties, and the thickness for both substrate and coating. By measuring the curvature difference before and after the removal of the coating (Δk), the residual stress, σ_R, in the coating, can be calculated:

$$\sigma_R = \frac{\Delta k E_f \left[h^2 + \left(E_S h_T^3 \right) / \left(E_f h \right) + \left(E_f h^3 \right) / \left(E_S h_T \right) + h_T^2 + 3(h + h_T)^2 \right]}{6(h + h_T)(1 - v_S)}$$

where h_T is the total thickness of the substrate plus coating, h is the coating thickness, v_S is the Poisson's ratio of the substrate, and E_S and E_f are the Young's modulus of the substrate and the coating, respectively. Detailed description about the curvature measurement has been reported by Xie and Hawthorne (2003). Figure 1.10 depicts the typical profiles of measured curvatures for sol–gel derived fluoridated HA coatings (Zhang et al. 2007). A larger

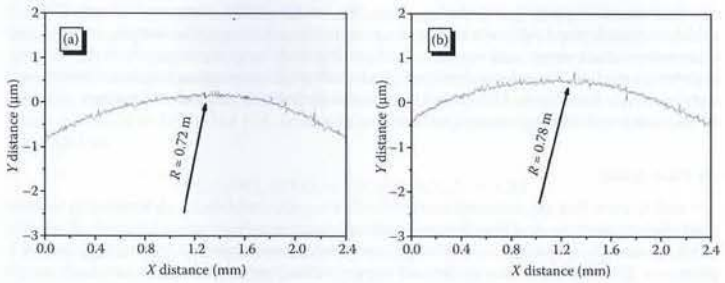

FIGURE 1.10
Typical profilometry results of measured curvatures for sol–gel derived fluoridated HA coating: (a) before removing the coating and (b) after removing the coating. The reduction of curvature caused by the removal of fluoridated HA coatings indicates a tensile residual stress existing in the coatings. (From Zhang et al., *Engineering Fracture Mechanics*, 74, 12, 1884–1893, 2007. With permission.)

curvature radius after removing the coating indicates a tensile residual stress existed in the coating.

A great number of possible parameters can cause residual stresses, depending on the deposition technique. Structure-related residual stress results from the following three aspects: thermal stress, growth-induced stress, and structural mismatch-induced (including lattice distortion) stress (Zhang et al. 2004). In a sol–gel deposition process, the thermal stress comes from the drying and firing process coupled with the difference in the coefficient of thermal expansion (CTE) between the coating and the substrate, the growth-induced stress comes from the coating shrinkage driven by capillary stresses during the drying and firing process, and the structural mismatch-induced stress comes from the difference in crystal structure between the coating and the substrate as well as the lattice distortion within the coating as a result of defects or incorporation of foreign molecules or molecule groups. Mainly, thermal stress, σ_{Rt}, always contributes more to the total residual stress in the coating, and it can be calculated by (Watanabe et al. 2002):

$$\sigma_{Rt} = \frac{\Delta\alpha \Delta T E_f}{1 - v_S}$$

where $\Delta\alpha$ is the difference of CTE between the interested coating and the metallic substrate and ΔT is the temperature variation during drying or firing. For example, CTE of HA is 15×10^{-6}/K, whereas that of Ti6Al4V substrate is about 8.9×10^{-6}/K (Zhang et al. 2006). Thereafter, the residual stress caused by thermal mismatch between HA coating and Ti6Al4V substrate should be tensile.

The presence of residual stress in the coating serves as an important influencing factor in determining the durability of the coated implants. Previous work has demonstrated that the existence of residual stress in HA coatings can alter the concentration of supernatant species in solution: tensile residual stresses enhancing dissolution and compressive

residual stress impeding dissolution (Han, Xu, and Lu 2001; Yang and Chang 2001). In addition, tensile residual stress will promote multiple cracking of the coating, and the compressive residual stress can weaken the bonding and bonding strength at the coating–substrate interface. Therefore, since both the tensile and compressive residual stresses exert detrimental influences on HA-coated implants, it is desirable to produce coatings on metallic implants without any unexpected residual stress.

In Vitro Assay

It is well known that any biomaterial must be thoroughly evaluated to determine its biocompatibility/bioactivity and whether it functions appropriately in actual biomedical applications. Generally, two kinds of evaluation techniques are employed for such purposes: *in vitro* (in a glass tube) and *in vivo* (in a living organism) tests. Although *in vivo* tests are the most direct and reliable evaluation methods for biomaterials, their results are normally difficult to obtain and interpret due to a lack of animal sources and the complexity of different cellular responses. (During *in vivo* tests, the cells that migrate to the implant surface contain different cell lineage, and the final results are demonstrated by the fact that the progeny of these cells may form a variety of tissue types adjacent to the implant.) (Boyan et al. 2001). *In vitro* testing can provide more rapid and relatively inexpensive data compared with *in vivo* testing. Moreover, *in vitro* testing can provide useful initial screening of materials and can aid in understanding the performance of a material *in vivo*. These valuable insights could also help to determine whether an implant/device needs further evaluation in expensive *in vivo* experimental models and minimize the amount of animals required in *in vivo* testing (Ratner et al. 1996). *In vitro* tests of biomaterials can be carried out in any cell-free or cell-containing environment to study their biocompatibility and bioactivity. In particular, cell-free solutions allow the study of chemical and mineralogical changes of the material under conditions that simulate the physiological interactions between the material surface and the surrounding tissues.

Dissolution Behavior

A prerequisite for any implant used in orthopedic or dental treatment is permanent fixation to the surrounding tissues with no intervening gaps or fibrous tissues (Vedantam and Ruddlesdin 1996). According to the *in vivo* and *in vitro* studies as well as more than a decade's clinical practice with HA-coated prostheses, there is general agreement that the originally desired benefits of HA coatings, that is, earlier fixation and stability with more bone ingrowth or outgrowth, can be achieved. However, doubts still exist concerning the durability of the fixation (Greenspan 1999). One of the most important events occurring at the bone–implant interface is the resorption of the HA coatings, also called degradation or coating loss (Bloebaum et al. 1994; Dalton and Cook 1995). Although some resorption or dissolution is, of course, essential to trigger bone–implant bonding, the fast resorption could lead to disintegration of the coating, with rapid loss of the bonding strength between it and the substrates, resulting in delamination, the production of particles, and loss of mechanical fixation. It is reported that a decrease as high as 31.6% was observed for plasma-sprayed HA coatings after only 2 weeks' immersion in SBF (Gu, Khor, and Cheang 2003). Other studies have shown resorption of HA coatings up to 2 years after implantation and a complete loss of a 60-μm-thick HA coating after 4 years (Sun et al. 2001). Aebli et al. (2003) carried out a histological study of a proximally HA-coated femoral component and found that the HA coating had completely degraded after 9.5 years' implantation.

Generally, the dissolution behavior of HA coatings are investigated in some Ca^{2+} ion free simulated physiological saline solution, such as Tris-buffered physiological saline solution (TPS) (Wang, Zhang et al. 2007) or citric acid-modified phosphate buffer solution (CPBS) (Weng, Zhang et al. 2003). Two competitive processes are commonly used to describe the surface reactions during the dissolution progress, dissolution and reprecipitation (Dorozhkin 1997). For HA coating, the dissolution/reprecipitation process can be described as:

$$Ca_{10}(PO_4)_6(OH)_2 \Leftrightarrow 10Ca^{2+} + 6PO_4^{3-} + 2OH^-$$

If the dissolution process is predominant, the coating will be dissolved continuously until a thermodynamic equilibrium is established for these two concurrent processes, and vice versa. Therefore, after incubating the coatings in the testing solutions, they will inevitably be dissolved quickly at first in such an unsaturated environment, and a thin Nernst layer will be formed in the solution near to the coating surface, which results in a certain reduction of coating dissolution rate.

The degradation of HA coating is strongly influenced by the coating phase composition (phase purity and crystallinity). Accordingly, using different solubilities of CaPs, the *in vivo* degradation rates of CaPs can be predicated and follow the order of (Yang, Kim, and Ong 2005; Ducheyne, Radin, and King 1993):

$$ACP >> TTCP \approx \alpha\text{-}TCP > DCPD > DCP > OCP > \beta\text{-}TCP >> HA$$

where ACP denotes amorphous calcium phosphate, TTCP is tetracalcium phosphate, α-TCP id α-tricalcium phosphate, DCPD is dicalcium phosphate dehydrate, DCP is dicalcium phosphate, OCP is octocalcium phosphate, and β-TCP is β-tricalcium phosphate.

Therefore, the presence of ACP (related to crystallinity) or other impurity phase (e.g., TCP) can cause a higher degradation rate at the initial stage after the immersion of HA-coated implants into the testing solution, followed by a "constant rate" dissolution of the remaining coating (Figure 1.11).

On the other hand, it is well known that actual human body fluid contains various kinds of organic components (such as carbohydrates and proteins), and these organic components are thought to exert certain influences on the degradation of HA coating (Dorozhkin, Dorozhkina, and Epple 2003; Liu et al. 2003). As a typical result, Figure 1.11 indicates the dissolution behaviors of sol–gel derived HA coating in glucose-modified TPS solution and in albumin-containing TPS solution. The results indicate that the addition of glucose has no significant influence on dissolution behaviors of FHA coatings in comparison with the tests in TPS. However, in comparison with the testing in TPS or G-TPS, the presence of albumin results in a significantly higher Ca^{2+} concentration released in the solution during the whole testing period.

Moreover, residual stress may affect the thermodynamics of dissolution behaviors by altering the chemical potential of the coatings. For those stress-free coatings, the unit free energy change of an equilibrium status, ΔG^0, can be described as (Han, Xu, and Lu 2001; Sergo, Sbaizero, and Clarke 1997):

$$\Delta G^0 = -RT \ln K_{sp}$$

where R is the gas constant, T is the temperature, and K_{sp} is the solubility product of the corresponding coating. If the constraint of a stress-free solid is removed and a stress, σ_{ss},

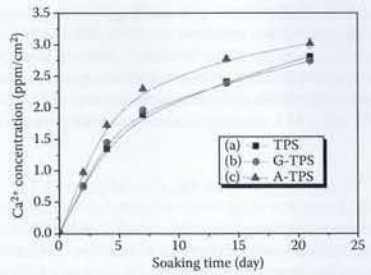

FIGURE 1.11
Dissolution behavior of sol–gel derived HA coatings in different testing conditions: (a) Tris-buffered physiological saline solution (TPS), (b) glucose-modified TPS (G-TPS), and (c) albumin-containing TPS (A-TPS).

is applied, such as a residual, the system is no longer in equilibrium because the chemical potential of the coatings is altered by an amount proportional to the stress, namely, $\sigma_{ss}\Omega/3$ per unit volume. (Ω is the unit volume of the species under consideration.) As a result, according to the thermodynamic analysis, with the presence of residual stress, additional free energy for the dissolution equilibrium becomes available in the form of elastic strain energy stored in the coatings, and the new equilibrium condition is represented by an altered value of the solubility product, K^{σ}_{sp}:

$$\Delta G^0 - \frac{\sigma_{ss}\Omega}{3} = -RT \ln K^{\sigma}_{sp}$$

The negative sign implies that a compressive residual stress will hinder, whereas a tensile residual stress will enhance the dissolution. Therefore, the ratio of the solubility product under different stresses (e.g., σ_1 and σ_2) is:

$$\frac{K^{\sigma_1}_{sp}}{K^{\sigma_2}_{sp}} = \exp\left[\left(\sigma_1 - \sigma_2\right)\frac{\Omega}{3RT}\right]$$

This expression can be used to estimate the change of solubility product owing to the presence of different residual stresses. Therefore, if the residual stresses in the sol–gel derived HA coatings are tensile stresses, a higher dissolution rate would be observed than the stress-free coatings correspondingly.

All in all, even though the mass loss caused by dissolution is somehow detrimental to the adhesion, it is still believed that the initial dissolution behaviors are quite beneficial to the healing process as well as the long-term successful osteointegration (Martini et al. 2003). First, the initial fast dissolution of the coating will result in a local super saturated environment (e.g., Ca^{2+}), which is more favorable for the nucleation and growth of bonelike apatite, speeding up the formation of chemical bonds between the implant and

surrounding tissues. On the other hand, a rough implant surface appears to be favorable for cell attachment and particularly suitable for primary implant stability as compared to a smooth implant surface. HA coatings with controllable degradation rate are much desired and can be realized by altering the phase composition, doping of other ions (F^-, Mg^{2+}, Zn^{2+}, etc.) (Cai et al. 2009; Wang, Sam et al. 2007; Miao et al. 2005), and controlling the residual stress.

In Vitro Test in Acellular Simulated Body Fluid

Currently, Simulated Body Fluid (SBF), which was first developed by Kokubo et al. in 1991, has been routinely used as an effective *in vitro* testing method to predict the *in vivo* bone bioactivity of various biomaterials (Kokubo and Takadama 2006). The development of SBF is based on the concept that the essential requirement for an artificial material to bond to living bone is the formation of bonelike apatite on its surface when implanted into the living body. The acellular SBF has similar inorganic ion concentrations to those of human blood plasma (as shown in Table 1.6) and can reproduce the formation process of bonelike apatite on biomaterials *in vitro*. Furthermore, this test can be used for the determination of the number of animals used during *in vivo* testing, as well as the duration of animal experiments. For a material to be bioactive *in vivo*, it must possess the capability to induce bonelike apatite formation on its surface in SBF. Many studies have been done on HA-coated metallic implants in SBF, which verified the intrinsic bioactivity of HA to be used as coatings (Gu, Khor, and Cheang 2003; Nagarajan, Raman, and Rajendran 2010; Stoch et al. 2005). On the other hand, the response of HA coatings in SBF was observed to be highly affected by coating phase composition, crystallinity, morphology, etc. (Ducheyne, Radin, and King 1993; Khor et al. 2003), and the precipitation rate of bonelike apatite was directly dependent on the Ca^{2+} ion concentration in the SBF at the vicinity of the coating surface (Lee et al. 2005; Montenero et al. 2000). As mentioned above, besides the HA phase, there also exists some other phases, including TCP, TTCP, and CaO, which possess higher solubilities than that of the HA phase. Therefore, in SBF testing, the dissolution of such impure phases will accelerate the precipitation rate of bonelike apatite through significantly enhancing the Ca^{2+} ion concentration at a localized area near to the implant surface (Gu, Khor, and Cheang 2003; Khor et al. 2003). To some extent, this indicates that the existence of impure phases in HA coating could improve the bioactivity of HA-coated metallic implants.

However, actual body fluid contains not only the inorganic components, but also various kinds of organic components (Table 1.6), and the organic components would exert noticeable influence on the implants (Dorozhkin, Dorozhkina, and Epple 2003; Wang, Sam et al. 2007). Therefore, it is unwise to neglect the influences of organic components in *in vitro* tests. Jaou et al. (2000) and Balint et al. (2001) reported that although sugar and/or glucose have a minor influence on crystallization of HA, they significantly inhibit the crystallization process of fluoridated apatite (FA). This effect was attributed to the formation of nonstoichiometric apatite in the presence of sugar. The inhibition effects of carbohydrates on the bone mineralization were also reported by other researchers (Pearce, Hancock, and Gallagher 1984; Balint et al. 2001). Dorozhkin, Dorozhkina, and Epple (2003) concluded that glucose exhibited negligible influence on crystallization of calcium phosphate based on *in vitro* tests with the glucose-modified SBF solution. On effects of proteins, extensive investigations have been done on CaP biomaterials, especially on HA (Luo and Andrade 1998; Xie, Riley, and Chittur 2001). It has been reported that plasma proteins would adsorb immediately on the surface of HA after it was implanted *in vivo*, and the initial cellular

TABLE 1.6
Chemical Composition of Human Blood Plasma Compared to Ion Concentration of Kokubo's SBF

	Inorganic Ion Concentration (mM)							Organic Composition (mg/dL)			
	Ca^{2+}	HPO_4^{2-}	Na^+	Cl^-	Mg^{2+}	K^+	HCO_3^-	SO_4^{2-}	Albumin	Globulin	Fibrinogen	Glucose
Blood plasma	2.5	1	142	103	1.5	5	27	0.5	3300–4000	880–3530	340–430	100
Kokubo's C-SBF	2.5	1	142	148	1.5	5	4.2	0.5	–	–	–	–

Source: Wang et al., *Materials Science and Engineering C*, 27, 2, 244–250, 2007. With permission.

response was partly dependent on the proteins adsorbed by the implant surfaces (Bender et al. 2000). The first protein layer adsorbed on the implant surface affects the cellular adhesion, differentiation, and production of extracellular matrix production (Combes and Rey 2002; Ducheyne and Qiu 1999). It also affects dissolution (Bender et al. 2000), nucleation, and crystal growth of HA as well as the final fixation between the implant and surrounding tissues (Xie, Riley, and Chittur 2001). Albumin is usually selected for this kind of study due to its high concentration in blood plasma, favorable diffusion coefficient, and ability to bind other ions and molecules (Jenney and Anderson 2000). It has been reported that albumin could slow down the nucleation rate and growth rate of new bonelike apatite in albumin-containing SBF.

Cell Response to HA Coating

Cell culture methods have been used to evaluate the biological compatibility of a material for more than two decades. Investigations on cell responses to materials can provide more details of understanding cell–materials interactions and can aid in establishing actual biological responses to artificial materials (Knabe et al. 2000). Because HA-coated metallic implants are used for hard tissue replacement/repairing, *in vitro* models using osteoblastic cells are essential and valuable tools for the initial assessment of candidate implants. Osteoblastic cells, which arise from pluripotential mesenchymal stem cells, have a set of distinguishing characteristics that include the ability to synthesize osteoid or bone matrix and to mineralize the osteoid to get the calcified bone (Aubin et al. 1995). Since then, osteoblastic cell lines are commonly employed for *in vitro* cellular assessments of hard tissue implants.

Initial Cell Attachment on HA-Coated Implant

The fixation of implants to bone is based on the process of osteointegration, which leads to direct apposition of mature living bone onto the implant surface (Menezes et al. 2003; Dorota et al. 2005). Since that osteointegration process is strictly mediated by osteoblastic cells, the fate of such implants is thus determined by the response of cells to the material's surface. Therefore, the implant should create favorable conditions for osteoblast attachment, spreading, growth, differentiation, and functionalization. Virtually, in a physiological environment, all implant surfaces become immediately coated with a 1- to 10-nm-thick adsorbed protein layer before cells can adhere to the material (Kasemo 1998; Tengvall 2003). The rapid adsorption of proteins effectively translates the structure and composition of the foreign surface into a biological language, which is also a response to the following host responses (Wilson et al. 2005). As such, when the cells arrive at the implant surface, they can only "see" a protein-covered surface. Those adsorbed proteins offer necessary binding sites to those anchorage-dependent cells, leading to the initial cell attachment onto the surface of biomaterials. For anchorage-dependent cells (e.g., osteoblastic cells), initial cell attachment and spreading are crucial prerequisites in determination of long-term viability of cells on the implant surface, involving DNA synthesis and cell growth (cell proliferation), differentiation, mineralization, and successful osseointegration (Folkman and Moscona 1978; Baxter et al. 2002). Therefore, a quick attachment of a certain amount of osteoblastic cells and the following rapid cell spreading are strongly expected.

Figure 1.12 shows the typical morphological change sequences of osteoblastic cell (MG63) spreading on sol–gel derived HA coatings during the first 4 h of incubation (Wang, Zhang et al. 2008). The process of cell attachment and spreading can be described by the following steps: (1) adsorption of proteins on coating surface (surface roughness plays a positive

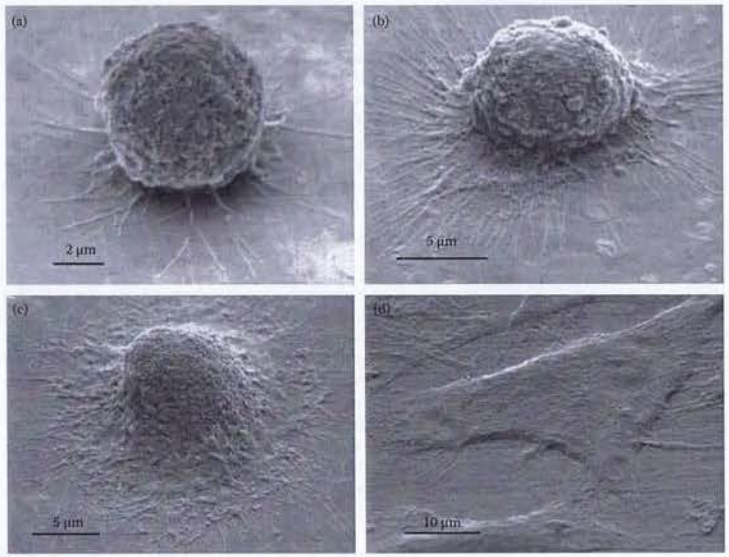

FIGURE 1.12
Morphological changes of osteoblastic cells after incubating on HA coatings for up to 4 h: (a) 0.5 h, (b) 1 h, (c) 2 h, (d) 4 h. The process of initial cell attachment and spreading can be described as the following continuous steps: contact and attachment of cells (a), centrifugal growth of filopodia (b), cytoplasma spreading (c), and cell flattening (d). (From Wang et al., *Journal of Biomedical Materials Research Part A*, 84, 3, 769–776, 2008. With permission.)

role); (2) contact and attachment of cells onto the protein layer (surface roughness does not have an effect unless very rough—a difference of more than a few microns); (3) centrifugal growth of filopodia; (4) cytoplasma spreading; and finally (5) cell flattening. It should be emphasized that these different stages are not discretely separable but are different phases of a contiguous progress. Recognition and studies of these different morphological events during initial cell adhesion and spreading on HA-coated implants would be of great value in understanding the behavior of osteoblastic cells *in vitro* and *in vivo*.

Cell Morphology

Along with the initial cell attachment and spreading, further cell spreading and the corresponding morphology also should be investigated in order to evaluate cell viability on the coating surface (Folkman and Moscona 1978). Figure 1.13 shows typical SEM micrographs of MG63 cells after a culture duration of 3 days on sol–gel derived HA coating surface. All cells spread well and grew favorably throughout the coating surface (Figure 1.13a). Under higher magnification (Figure 1.13b), the cells are seen flattened and attached tightly on coating surface with their filopodium and lamellipodium, suggesting good cell viability

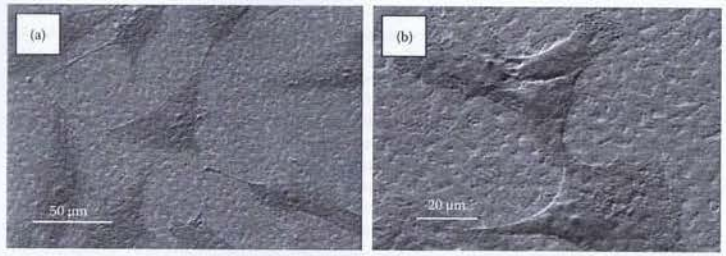

FIGURE 1.13
Morphology of MG63 cell after 3 days on sol–gel derived HA coating at (a) low magnification and (b) high magnification. All cells spread well and grow favorably throughout the coating surface, suggesting good cell viability of the HA coating. (From Wang et al., *Materials Science and Engineering C*, 27, 2, 244–250, 2007. With permission.)

on the fabricated HA coating (Wang, Zhang et al. 2007). As reported, the well-spread cells on the fabricated HA coating surface are believed to be favorable for the following DNA synthesis and cell growth.

Cell Proliferation and Differentiation

Following the initial cell attachment and spreading, those well-spread cells will step into the stages of proliferation and functionalization. Roughly, the progress from an initially attached osteoblastic cell to well-differentiated mature osteoblast (osteocyte) can be divided into three stages: proliferation, differentiation or extracellular matrix synthesis and maturation, and mineralization (Stein and Lian 1993).

During the first several days following cell attachment and spreading, cells try to reproduce, and an active cell proliferation is directly reflected by the exponential increase of cell number as well as the deposition of type I collagen. On the other hand, several genes related to cell cycle (e.g., histone) and cell growth (e.g., *c-myc*, *c-fos*, and *c-jun*) are actively expressed and can be used to monitor those mitotic activities (Stein and Lian 1993). Commonly, cell proliferation (increase in cell number) is directly monitored through the following two quantitative methods: cell counting under a microscope (with a hemocytometer) and MTT assay (Kim et al. 2005; Wang, Zhang et al. 2007). These two methods are much easier than other protein- or gene-based methods. Noticeably, the variation in cell numbers is sometimes employed to assess and screen the cytotoxicity of a biomaterial (cell viability). Roughly, a decrease in cell number during the culture span reveals a cytotoxic environment caused by the biomaterial, or the material itself is toxic to the cells.

Immediately after the down-regulation of proliferation, cell phenotypes associated with osteoblastic cell differentiation can be detected, indicating that the cells step into the differentiation stage (Stein and Lian 1993). The most frequently used markers of osteoblast differentiation are alkaline phosphatase (ALP), and osteocalcin (OC). As an early differentiation marker, ALP is an enzyme associated with calcification. This is an early marker of osteoblastic cell differentiation because activity is greatest just before mineralization actually begins. It is reported that an enhanced expression of this enzyme is apparently needed just before the onset of matrix mineralization, providing localized enrichment of inorganic phosphate, one of the components of apatite (the mineral phase of bone) (Boyan et

al. 2001; Kartsogiannis and Ng 2004). High levels of bone ALP are usually detected in both preosteoblasts (osteoblastic cells) and osteoblasts *in vivo* and in differentiating osteoblastic cells *in vitro*. Along with ALP, OC, known as a late marker of cell differentiation, is a small molecular weight protein (5.7 kDa) produced by osteoblasts and has the ability to chelate Ca^{2+} to form bone minerals (Stein and Lian 1993; Gerstenfeld et al. 1987). For this reason, it is a particularly effective marker of a well-differentiated osteoblastic cell. Generally, once mineralization is initiated, ALP will decrease, whereas osteocalcin accumulation continues, reflecting an expression related to deposition of mineral for the latter.

As one of calcium phosphate ceramics, sintered HA has been well established as a bioactive material that enhances osteoblastic cell viability and osteointegration with host bone (Hench 1991; Greenspan 1999). Those valuable biological properties are well maintained when HA is used as coatings on metallic implants. In comparison with those bioinert metallic implants, many studies reported that the fabricated HA coatings on their surface not only can help to stimulate cell growth and DNA synthesis, but also can enhance the ALP and OC activities and the mineralization of extracellular matrix (Massaro et al. 2001; Yang, Kim, and Ong 2005; Li et al. 2005). However, these desired biological properties of HA coatings are highly dependent on coating surface roughness. Lee et al. (2002) investigated the cell responses to HA coatings with different roughness values (R_a), 0.67 and 10.37 μm, and concluded that the smoother surface was more favorable for cell attachment than the rougher one. Moreover, Kim et al. (2005) reported that the higher surface roughness (R_a = 0.84 μm) could significantly enhance the number of attached cells compared with the lower surface roughness (R_a = 0.22 μm), but there was no significant difference regarding cell proliferation and differentiation. An enhanced effect on cell differentiation activities and the formation of bone nodules was observed in other researchers' studies (Li et al. 2005; Perizzolo et al. 2001; Borsari et al. 2005).

On the other hand, several other studies also indicated that the behavior of cultured osteoblastic cells are affected by the crystallinity and phase composition of the prepared HA coatings (Yang, Kim, and Ong 2005). Kim et al. (2005) claimed that on the coatings with higher crystallinity (>76%), the cells attached and proliferated well and expressed ALP and OC to a higher degree as compared to the poorly crystallized coatings (~43% crystallinity). Chou, Marek, and Wagner (1999) reported that the lower crystalline coatings with some other impure phases (CaO, TCP, etc.) were favorable to cell attachment but exerted inhibiting effects on cell proliferation due to the elevated medium pH value caused by the dissolution of the impure phase. However, other studies illustrated insignificant influences on cell attachment, proliferation, and differentiation or mineralization with respect to different crystallinity and/or phase compositions (Siebers et al. 2006).

Although it is commonly accepted that the HA coatings could improve the *in vitro* biological properties for those metallic implants, there still exist some inconsistent or even conflicting viewpoints regarding the influences of coating properties on cell responses. Considering those differences in coating preparation, experimental setup, testing methods, etc., it is hard to judge which one is more acceptable.

In Vivo Animal Trial

Practically speaking, the goal of *in vivo* animal trial of implants or devices is to determine and predict whether such implants/devices possess potential harm to the human body by evaluations under conditions simulating clinical end-use applications (Anderson 2001). *In vivo* models allow the direct evaluation of toxicity of a biomaterial and the efficacy of a biomaterial as implant/device within a therapeutic application. Therefore, those

osteointegration (the close apposition of bone to implant surface) examinations during *in vivo* studies are essential for further analysis about the effect of the implant on the expression of osteoblast phenotype and even for future clinical application.

Histological analysis of HA-coated implants has shown that bone ingrowth with osseous integration occurs as early as 10 days following implantation (Furlong and Osborn 1991). Thereby, HA coating could provide the crucial initial fixation requirement for the success of an implant. Furthermore, a histomorphometric study by Moroni et al. (1994) comparing the percentage of bone bonding to plasma sprayed HA-coated and uncoated implants in dogs revealed a significant increase in bone amount in the HA-coated implants. They also showed enhancement of bone-to-pin osseointegration and interfacial strength in HA-coated pins as compared to uncoated pins in a sheep study (Moroni et al. 1998). Figure 1.14 shows the typical histological micrograph on the enhancing effect of HA coating on bone–implant fixation (Hirai et al. 2004): after 4 weeks' implantation in the transfemoral drill hole on a rat, the area of the new bone of the cross-sectional implants was 0.108 mm^2 for sol–gel HA-coated titanium and only 0.087 mm^2 for uncoated samples. That is to say, the implant with HA coating had comparatively higher bone apposition ability than the uncoated implant. Similar results have been reported in other studies (Ramires et al. 2003; Gerber et al. 2003; You, Yeo et al. 2005).

Along with the histological analysis, extensive investigations have been conducted on the bonding strength of HA-coated implants during *in vivo* animal trials. For instance, in the studies of Oonishi et al. (1989), the adhesion strength between the implant and bone was ~0.53 and ~1.35 MPa for uncoated and HA-coated implants, respectively, at 2 weeks after implantation, whereas those bonding strengths increased to ~7.5 and ~14.15 MPa at 6 weeks, correspondingly. Other short-term *in vivo* trials also elucidated the similar trend regarding the bone-implant bonding property (Yang, Lin et al. 1997; Chang et al. 1997; Dalton et al. 1995). Essentially, it is revealed that those rapid and positive responses of HA coatings *in vivo* benefit significantly from the fast dissolution of related impure phases (e.g., amorphous phase, TCP), which results in an increase in Ca^{2+} and PO_4^{3-} ion concentrations in local areas around the implant–bone interface. Nevertheless, from the viewpoint of long-term stability, whether the loss of HA coating could maintain such a desired bonding strength between the implant and surrounding tissue is questioned.

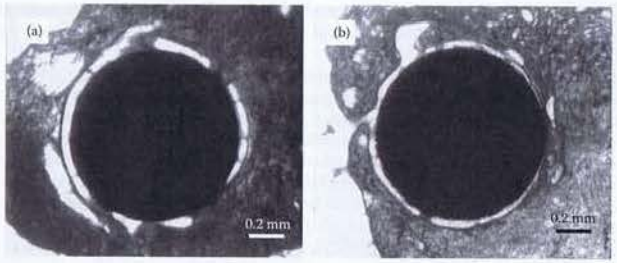

FIGURE 1.14
Histological sections of the nondecalcified sections after 4 weeks' implantation in a transfemoral drill hole on a male Wister rat: (a) sol–gel coated titanium, (b) uncoated titanium. The area of the bone of the cross-sectional implants was 0.108 mm^2 for sol–gel HA-coated titanium and 0.087 mm^2 for uncoated titanium. (From Hirai et al., *Journal of the American Ceramic Society*, 87, 1, 29–34, 2004. With permission.)

Recent Trends Related to Sol–Gel Derived HA Coatings

Even though previous studies on HA-coated metallic implants have shown good fixation to the host bones and increased bone ingrowth into the implants, there are still many concerns about the application of HA coatings, especially the related long-term stability of HA coating (Greenspan 1999). One of the most serious concerns raised is the resorption or degradation of HA coating in a biological environment. Faster resorption or degradation rate is likely to result in faster and stronger fixation in the initial stage of implantation, but could also lead to disintegration of the coating, including rapid loss of interface bonding strength of the coating–substrate and implant-surrounding tissue, delamination of HA coating, etc. (Bloebaum et al. 1994). Hence, the stability and integrity of the coating on metallic implants should be carefully considered prior to any clinical application. By contrast, a controlled resorption or degradation rate may allow the surrounding bone the opportunity to replace the resorbed coating at the similar rate and achieve the desired long-term stability.

Unfortunately, particles or particulates, as the products of HA degradation, may cause severe damage or complications to the bone–implant system. It is reported that the HA particles can be resorbed by macrophages if their size is sufficiently small compared to the macrophages (approximately 30 μm) (Mullermai, Voigt, and Gross 1990). When a macrophage phagocytizes the particles, the cells release cytokines, prostaglandins, and collagenases almost immediately. If the particles do not dissolve within the life span of the macrophage, more macrophages will accumulate at the site in response to the release of cytokines to digest the dead macrophages and those undissolved HA particulates. As well, particles larger than a macrophage (>30 μm), will not be digested by macrophages and will probably become engulfed by a giant cell. The excessive cellular reaction to HA particulates and the stimulation of a foreign-body response could lead to a decrease in local pH value, which disrupts the bone remodeling process, causing the dissolution/resorption of both HA coating and bone (Gross, Walsh, and Swarts 2004). Additional problems could arise if particulate debris travels to the implant–bone interface, producing third-body wear and component loosening/failure. Morscher, Hefti, and Aebi (1998) investigated six revisions of HA-coated implants follow-up over 10 years after successful primary implantation. They found that HA granules had embedded in all of the examined implants, and as high as 66.7% of them had loosened and 50% of them showed severe osteolysis of the proximal femur.

Understanding that the essential issue of the above problems is the high rate of biodegradation, a possible solution has been proposed: fabrication of macro- and micro-textured porous surfaces to overcome the problems of dissolution and micromotion. Overgaard et al. (1998) compared the influences of different surface textures (microporous and grit-blasted) of plasma sprayed HA-coated implants on the mechanical fixation, bone ingrowth, bone remodeling, and gap healing after implanting the implants in dogs for 16 weeks. It was concluded that the microporous HA-coated surface could provide better fixation for both interfaces of coating–substrate and implant-surround tissues. What's more, more new bone was generated on the microporous HA-coated implants to replace and/or compensate the resorption of HA coating, suggesting a possible long-term fixation for this kind of implant. However, this kind of HA coating commonly possesses a larger thickness, which could cause the potential risk of generating large particulate debris. Another possible way is the incorporation of F^- into HA lattice structure through the $F^- \leftrightarrow OH^-$ exchange to form a fluoridated HA coating ($Ca_{10}(PO_4)_6F_x(OH)_{2-x}$, where x is the degree of fluoridation: $x = 0$, pure HA; $x = 2$, pure FA; $0 < x < 2$, fluoridated hydroxyapatite [FHA]). Considering the advantages of the sol–gel method (cf. Section 1.3.1), preliminary studies on fluoridated HA coatings have been successfully produced using the sol–gel method on titanium alloy substrates (Zhang et al. 2006). The incorporation of F^- cannot only reduce the degradation rate of the coating, but also benefit the interfacial adhesion properties of the coating–substrate. Fluoridate HA coatings have since attracted much attention as a promising replacement for pure HA because fluoridated HA demonstrates significant resistance to biodegradation.

On the other hand, it is well known that human bone contains certain trace elements, such as K^+, Na^+, Mg^{2+}, Zn^{2+}, Cl^-, F^-, etc., and these trace elements exert crucial influences on bone metabolism through promoting biocatalytic reactions and/or controlling some related metabolic processes (Hench and Wilson 1993; Aoki 1994). As such, some efforts have been made to incorporate some of these trace elements into the HA structure to improve further related properties of pure HA (to mimic the actual composition of human bones). Besides F^-, Mg^{2+} and Zn^{2+} are the two most promising ions to improve the bioactivity of pure HA coating (Qi et al. 2008; Köseoğlu et al. 2009; Chung et al. 2006). However, those Mg- and Zn-incorporated HA coatings always possess higher solubility than that of pure HA coating. Recalling the feature of an ideal coating, short-term rapid degradation (bioactivity) and long-term dissolution-resistance (stability), codoping of (Mg^{2+}, F^-) or (Zn^{2+}, F^-) are accordingly proposed (Miao et al. 2005). In addition, biphasic coatings of β-TCP/FHA and functional graded multilayered coatings are also possible ways to achieve the combination of bioactivity and stability (Cheng, Zhang, and Weng 2006).

In summary, HA-coated metallic implants are attracting the highest interest for hard tissue repair/replacement, since these kinds of implants can combine the advantages of both materials: the bioactivity of HA and the excellent mechanical properties of metallic substrates. The sol–gel technique is the most preferred method for preparing HA coatings due to its distinguishing characteristics (e.g., ability for tailoring chemical compositions, improved homogeneity at the molecular level, ability to produce uniform coating, low cost, and easy operation). More HA-base high-performance coatings are expected to be produced using the sol–gel method in order to satisfy the requirement of bioimplants.

References

Aebli, N., J. Krebs, D. Schwenke, H. Stich, P. Schawalder, and J. C. Theis. 2003. Degradation of hydroxyapatite coating on a well-functioning femoral component. *Journal of Bone and Joint Surgery-British Volume* 85B (4):499–503.

Agrawal, D. C., and R. Raj. 1989. Measurement of the ultimate shear—strength of a metal ceramic interface. *Acta Metallurgica* 37 (4):1265–1270.

Agrawal, D. C., and R. Raj. 1990. Ultimate shear strengths of copper silica and nickel silica interfaces. *Materials Science and Engineering A Structural Materials Properties Microstructure and Processing* 126:125–131.

Ak Azem, F., and A. Cakir. 2009. Synthesis of HAP coating on galvanostatically treated stainless steel substrates by sol–gel method. *Journal of Sol–Gel Science and Technology* 51 (2):190–197.

Aksakal, B., M. Gavgali, and B. Dikici. 2009. The effect of coating thickness on corrosion resistance of hydroxyapatite coated Ti6Al4V and 316L SS omplants. *Journal of Materials Engineering and Performance* 1–6.

Albrektsson, T. 1998. Hydroxyapatite-coated implants: A case against their use. *Journal of Oral and Maxillofacial Surgery* 56 (11):1312–1326.

Exhibit A-5

Carine Viornery et. al. Surface Modification of Titanium with Phosphonic Acid To Improve Bone Bonding: Characterization by XPS and ToF-SIMS. Langmuir. 2002 18(7): 2582-2589.

Surface Modification of Titanium with Phosphonic Acid To Improve Bone Bonding: Characterization by XPS and ToF-SIMS

Carine Viornery,[†,‡] Yann Chevolot,[‡,§] Didier Léonard,[§,||] Björn-Owe Aronsson,[*,⊥] Péter Péchy,[†] Hans Jörg Mathieu,[§] Pierre Descouts,[⊥] and Michael Grätzel[†]

Laboratory for Photonics and Interfaces, Department of Chemistry, EPF-Lausanne, CH-1015 Lausanne, Switzerland, Laboratory of Metallurgical Chemistry, Department of Materials, EPF-Lausanne, CH-1015 Lausanne, Switzerland, and Group of Applied Physics-Biomedical, University of Geneva, CH-1211 Geneva, Switzerland

Received June 18, 2001. In Final Form: December 12, 2001

Commercially pure titanium (cp Ti) is widely used in dental implantology. However, it is only passively integrated in bone and the resulting fixation in the bone, which is necessary for the function, is mainly mechanical in its nature. With the objective of increasing the chemical interaction between the implant and bone tissue, several phosphonic acids were synthesized and grafted onto titanium disks. The bare polished Ti disks (Ti P) and the grafting of three phosphonic acids (methylenediphosphonic acid (MDP), propane-1,1,3,3-tetraphosphonic acid (PTP), and ethane-1,1,2-triphosphonic acid (ETP)) on these disks were characterized with X-ray photoelectron spectroscopy (XPS) and time-of-flight secondary ion mass spectrometry (ToF-SIMS). These surface analytical techniques provided strong indications of the formation of a chemical link between the Ti implant and the phosphonic acid molecule. The bioactivity of the modified Ti disks was evaluated by incubating these disks in a physiological solution (Hank's balanced salt solution (HBSS)) for 1, 7, and 14 days. Modified surfaces showed only slightly higher calcium levels in the XPS analysis compared to the reference Ti P surface. Among them, the surface modified with ETP (Ti P + ETP) induced the highest calcium phosphate deposition after 14 days incubation.

Introduction

Among metallic biomaterials in implantology, titanium (Ti) is presently the most widely used as dental implant. As pointed out by Steinemann[1] Ti is "the material of choice" for hard tissue replacement due to its high chemical stability in the body caused by the passivating native oxide film of TiO_2, which covers it.[2] It also possesses suitable physical properties.[3] However, even if Ti osseointegrates, it is only passively integrated in bone and, as other metals, cannot directly bind to bone. Several coatings have been proposed to enhance bone growth around the implant. Calcium phosphates form a class of materials that are close to the mineral phase of bone in composition, and among them the most promising is hydroxyapatite (HA). The most commonly used technique for HA coating is plasma spraying, which has been widely studied.[4−7] It has been considered that HA coating reduces the time required for osseointegration. However, the long-term success is dependent upon the maintenance of the adhesion between the metal and the ceramic coating, and recent data suggest that breakdown of this interface may occur.[8,9] The detachment of the coating could lead to bone resorption and finally loosening of the implant.[6] Dissolution of the hydroxyapatite coating[10−12] has also been reported in the literature. Other coating techniques have been developed, such as pulsed laser deposition,[13] sputter coating,[14] sol−gel deposition,[15] electrocrystallization,[16] and surface-induced mineralization from supersaturated salt solutions.[17] The major problem with these coatings remains the mechanical weakness of the metal oxide/calcium phosphate interface.

The aim of the work presented here was to chemically modify a Ti implant with phosphonic acid based molecules and to study the bioactivity in terms of (1) chemical interaction with the bone mineral phase and (2) stimulation of bone growth on its surface. The phosphonic acid

* Corresponding author. Fax: + 41 22 781 0980. E-mail: bjorn-owe.aronsson@physics.unige.ch.

† Department of Chemistry, EPF-Lausanne.

‡ Present address: 19 rue Koenig, FR-29660 Carantec, France.

§ Department of Materials, EPF-Lausanne.

|| Present address: Analytical Technology, General Electric Plastics Europe, 4600 AC Bergen Op Zoom, The Netherlands.

⊥ University of Geneva.

(1) Steinemann, S. G. *Periodontology 2000* **1998**, *17*, 7−21.

(2) Kasemo, B.; Lausmaa, J. Surface science aspects on inorganic biomaterials. In *CRC Critical Reviews in Biocompatibility*; Williams, D. F., Ed.; CRC Press: New York, 1986; Vol. 2, pp 335−380.

(3) Williams, D. F. *J. Med. Eng. Technol.* **1977**, *6*, 195−198, 202−203.

(4) Geesink, R. G. T.; Groot, K. d.; Klein, C. P. A. T. *Clin. Orthop. Relat. Res.* **1987**, *225*, 147−170.

(5) Groot, K. d.; Geesink, R.; Klein, C. P. A. T.; Serekian, P. *J. Biomed. Mater. Res.* **1987**, *21*, 1375−1381.

(6) Ogiso, M.; Yamamura, M.; Kuo, P. T.; Borgese, D.; Matsumoto, T. *J. Biomed. Mater. Res.* **1998**, *39*, 364−372.

(7) Golec, T.; Krauser, J. *Dent. Clin. North Am.* **1992**, *36*, 39−65.

(8) Dhert, W. J. A.; Klein, C. P. A. T.; Wolke, J. G. C.; Velde, E. A. v. d.; Groot, K. d. *J. Biomed. Mater. Res.* **1991**, *25*, 1183−1200.

(9) Combe, E. C.; Burke, F. J. T.; Douglas, W. H. *Dental biomaterials*; Kluwer Academic Publishers: London, 1999.

(10) Radin, S. R.; Ducheyne, P. *J. Mater. Sci.: Mater. Med.* **1992**, *3*, 33−42.

(11) Ducheyne, P.; Radin, S.; King, L. *J. Biomed. Mater. Res.* **1993**, *27*, 25−34.

(12) Klein, C. P. A. T.; Wolke, J. G. C.; Bleich-Hogervorst, J. M. A. d.; Groot, K. d. *J. Biomed. Mater. Res.* **1994**, *28*, 909−917.

(13) Cotell, C. M. *Appl. Surf. Sci.* **1993**, *69*, 140−148.

(14) Dijk, K. v.; Schaeken, H. G.; Wolke, J. C. G.; Marée, C. H. M.; Habraken, F. H. P. M.; Verhoeven, J.; Jansen, J. A. *J. Biomed. Mater. Res.* **1995**, *29*, 269−276.

(15) Piveteau, L. D.; Gasser, B.; Schlapbach, L. *Biomaterials* **2000**, *21*, 2193−2201.

(16) Shirkhanzadeh, M.; Azadegan, M.; Stack, V.; Schreyer, S. *Mater. Lett.* **1994**, *18*, 211−214.

(17) Campbell, A. A.; Fryxell, G. E.; Linehan, J. C.; Graff, G. L. *J. Biomed. Mater. Res.* **1996**, *32*, 111−118.

10.1021/la010908i CCC: $22.00
Published on Web 03/03/2002

group has already been shown to bind strongly to TiO_2 in a large pH range (from pH 1 to pH 9)[18] and to hydroxyapatite.[19]

In our earlier work it was found that, after appropriate cleaning of a bare titanium surface, it is able to nucleate the growth of calcium phosphate layers from a Hank's solution.[20] This nucleation is initiated by the surface adsorption of phosphate ions with subsequent complexing of calcium ions and a slow formation of an apatite-like surface layer is obtained. The necessary conditions for the complexation of Ca ions were found to be relatively pH dependent and strongly dependent on the presence of a minimum concentration of phosphate ions in the solution. Furthermore, a mixture of KH_2PO_4 and Na_2HPO_4 favored the apatite film formation. We also studied the mechanism and nature of the initial phosphate adsorption on titanium oxides. By electron energy loss spectroscopy, evidence was found for a covalent binding of phosphate molecules (from phosphoric acid) on either oxygen vacancies (acidic sites) or in a substitution reaction with surface bound oxygen (basic sites).[21] We also suggested that this is at least a bidentate binding, involving two, or possibly three, of the four oxygen bound to the phosphorus atom, resulting in a very strongly bound molecule. From this study we can suggest that phosphonic acids adsorb in an analogous way on the titanium oxide and may serve as anchoring molecules for the mineral phase of bone (HA).

Three phosphonic acid molecules were synthesized and grafted onto Ti disks. X-ray photoelectron spectroscopy (XPS) and time-of-flight secondary ion mass spectrometry (ToF-SIMS) surface analysis techniques were used to chemically characterize the Ti disks and the grafting of the phosphonic acids on these disks. Then, the adsorption of the mineral components of bone was simulated by incubating the modified and unmodified Ti disks in a physiological solution, Hank's balanced salt solution (HBSS). The precipitation of calcium and phosphates on the different Ti disks was again measured by XPS and ToF-SIMS.

Cell culture studies of the same system are presented elsewhere.[22]

Materials and Methods

Substrates. The mechanically polished titanium disks (commercially pure (cp) titanium, 99.6% grade 2; 14 mm in diameter) were prepared and supplied by Institut Straumann AG (Waldenburg, Switzerland). The samples were sonicated in 2% phosphate free Deconex (15PF, Merck, CH) in bidistilled water for 15 min at 30 °C, rinsed with bidistilled water followed by sonication in bidistilled water (three times) for 10 min, and finally rinsed with pure hexane. The samples were dried and stored under vacuum (1333 Pa, room temperature (RT)) over P_2O_5 before being analyzed with XPS and ToF-SIMS.

Surface Modification. Three phosphonic acid molecules, methylenediphosphonic acid (MDP), propane-1,1,3,3-tetraphosphonic acid (PTP), and ethane-1,1,2-triphosphonic acid (ETP), were prepared according to the described procedures.[23−25] Grafting on the polished Ti (Ti P) disks was obtained by chemical adsorption from solution for 1 h at room temperature at the following conditions: MDP, 1.5×10^{-3} M; PTP, 6.2×10^{-4} M; ETP, 1.2×10^{-3} M (in 10 mL of bidistilled water). After grafting, the disks were rinsed with bidistilled water to remove physisorbed phosphonic acids, dried under vacuum (1333 Pa, RT) over P_2O_5, and analyzed with XPS and ToF-SIMS.

Incubation in Hank's Balanced Salt Solution (HBSS). Next, the modified and unmodified Ti disks were incubated at 37 °C ± 0.5 °C in 50 mL of Hank's balanced salt solution (HBSS) in closed plastic bottles. The solution was always freshly prepared by dissolving reagent-grade chemicals in bidistilled water. Its chemical composition was the following (mM):[26] Na^+, 142.0; K^+, 5.81; Mg^{2+}, 0.811; Ca^{2+}, 1.26; Cl^-, 145.0; HPO_4^{2-}, 0.777; SO_4^{2-}, 0.811; HCO_3^-, 4.17 mM. The pH was 7.4 at 37 °C. After incubation for 1, 7, and 14 days, the samples were rinsed with bidistilled water and dried under vacuum (1333 Pa, RT) over P_2O_5. Three disks per surface were incubated and subsequently analyzed with XPS and ToF-SIMS.

X-ray Photoelectron Spectroscopy (XPS). XPS analyses were performed on an Axis Ultra spectrometer from Kratos (Kratos, Manchester, U.K.) equipped with a concentric hemispherical analyzer and using a monochromatized aluminum anode X-ray source (Al $K\alpha_{1,2}$ 1486.6 eV, full width at half-maximum, fwhm = 0.85 eV, 15 kV, 150 W). The samples were investigated under ultrahigh vacuum conditions: $10^{-8}-10^{-7}$ Pa. Spectra were taken at a 90° takeoff angle with respect to the surface. A sample area of 300×700 μm^2 was analyzed with a pass energy of 80.0 eV for survey scans and 40.0 eV for high energy resolution elemental scans.

The spectrometer was calibrated by using Cu 2p3/2 (932.7 eV) and Au 4f7/2 (84.0 eV) signals. Scofield's[27] surface sensitivity factors used to determine the atomic concentrations were 0.278 for C 1s, 0.780 for O 1s, 2.001 for Ti 2p, 0.486 for P 2p, and 1.833 for Ca 2p. Spectra were referenced to C 1s spectrum of C−H/C−C at 285.0 eV. Spectra were peak fitted after background subtraction by assuming a Gaussian/Lorentzian (90−70/10−30) peak shape except for the asymmetric Ti metallic peak. Mean reproducibility of peak position values obtained from peak fitting are in general not better than ±0.1 eV, and for the complex structures they can even vary with as much as 0.3 eV from sample to sample and depend on other peak fitting parameters.[28]

Time-of-Flight Secondary Ion Mass Spectrometry (ToF-SIMS). ToF-SIMS analyses were performed on a PHI Trift I mass spectrometer (described in detail elsewhere[29]) equipped with a pulsed Ga^+ liquid ion gun operated at 15 kV. Sample surfaces were biased at ±3 kV with respect to the grounded extraction electrode for positive and negative mode SIMS, respectively. The dc ion beam current (2−4 nA) was pulsed at 5 kHz repetition rate, with a measured pulse width of about 8 ns. The analyzed area was approximately 84×84 μm^2. The total ion dose used to acquire each spectrum was about 10^{12} ions/cm^2 ensuring static SIMS conditions.[30] The mass resolution measured on the $Si^{+/-}$ signal of a silicon wafer was $m/\Delta m = 5000$ in the positive mode and $m/\Delta m = 4000$ in the negative mode.

Three areas were analyzed/sample in each mode, and the most representative of them are presented. Calibration of the mass spectra in the positive mass mode was based on hydrocarbon peaks such as CH_3^+ (15.025 atomic mass unit (amu)), $C_2H_5^+$

(18) Péchy, P.; Rotzinger, F. P.; Nazeeruddin, M. K.; Kohle, O.; Zakeeruddin, S. M.; Humphry-Baker, R.; Grätzel, M. *J. Chem. Soc., Chem. Commun.* **1995**, 65−66.

(19) Meyer, J. L.; Nancollas, G. H. *Calc. Tiss. Res.* **1973**, *13*, 295−303.

(20) Frauchiger, L.; Taborelli, M.; Aronsson, B.-O.; Descouts, P. *Appl. Surf. Sci.* **1999**, *143*, 67−77.

(21) Unal, K. Adsorption de phosphates sur l'oxyde de titane étudié par des spectroscopies électroniques [Adsorption of phosphates on titanium oxide studied by electron spectroscopy]. Diploma thesis, University of Geneva: Geneva, Switzerland, 1999.

(22) Viornery, C.; Guenther, H. L.; Aronsson, B.-O.; Péchy, P.; Descouts, P.; Graetzel, M. *J. Biomed. Mater. Res.*, in press.

(23) Quimby, O. T.; Curry, J. D.; Nicholson, D. A.; Prentice, J. B.; Roy, C. H. *J. Organomet. Chem.* **1968**, *13*, 199−207.

(24) Quimby, O. T. Propanepolyphosphonate compounds. U.S. Pat. 3,400,176, 1968.

(25) Haegele, G. Verfahren zur Herstellung von Oligophosphonsäuren beziehungsweise Oligophosphinsäuren, ihren salzen und/oder Estern sowie neue phosphosäure- und phosphinsäurederivative. [Procedure for Production of Oligophosphonic Acid and Oligophosphinic Acid, Their Salts and/or Esters as Well as New Phosphonic and Phosphinic Acid Derivatives] DE 31 11 152 A1, 1982.

(26) Kokubo, T.; Kushitani, H.; Sakka, S.; Kitsugi, T.; Yamamuro, T. *J. Biomed. Mater. Res.* **1990**, *24*, 721−734.

(27) Scofield, J. H. *J. Electron Spectrosc. Relat. Phenom.* **1976**, *8*, 129.

(28) Sabbatini, L.; Zambonin, P. G. *J. Electron Spectrosc. Relat. Phenom.* **1996**, *81*, 285−301.

(29) Franzreb, K.; Mathieu, H. J.; Landolt, D. *Surf. Interface Anal.* **1995**, *23*, 641−651.

(30) Briggs, D. *Static SIMS−Surface analysis of organic materials*; Briggs, D., Seah, M. P., Ed.; J. Wiley & Sons: Chichester, U.K., 1992; pp 367−423.

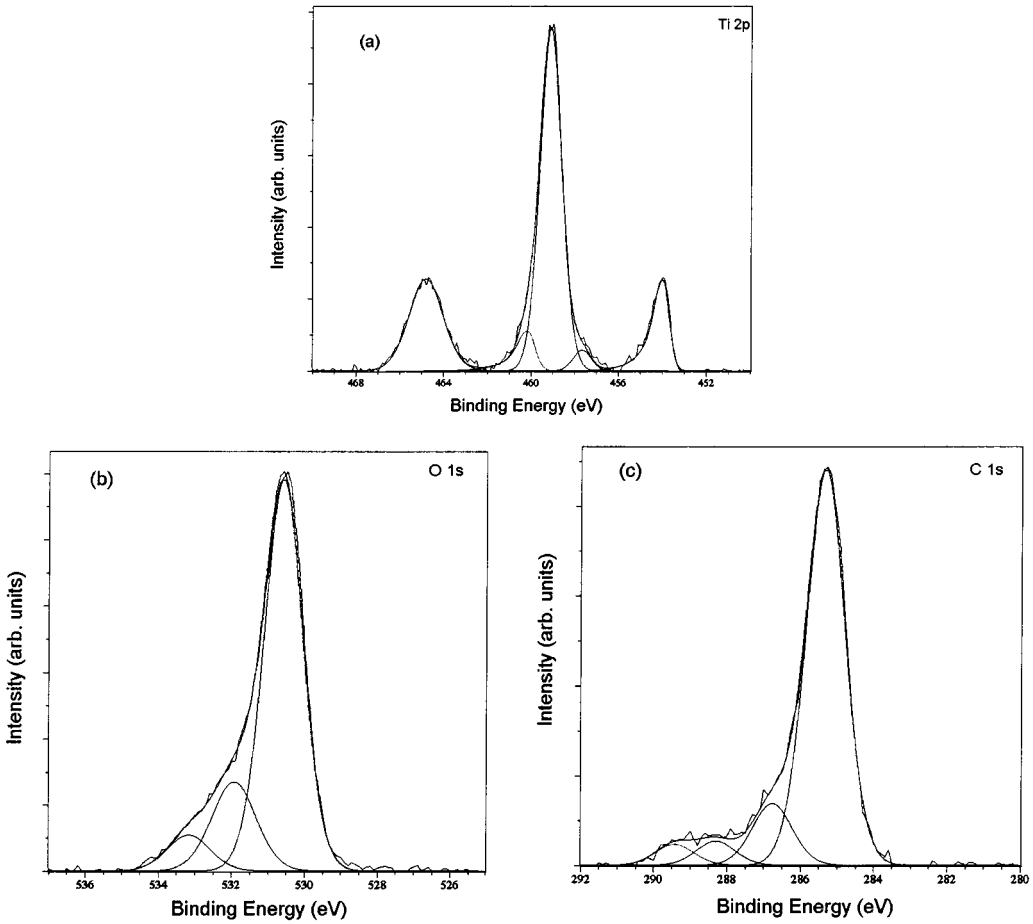

Figure 1. High-resolution XPS spectra of Ti P surface: (a) Ti 2p; (b) O 1s; (c) C 1s.

Table 1. Chemical Composition (at. %) of the Native Ti P Surface

sample	Ti	O	C	P	Ca	N
Ti-P	18.8 ± 1.6	50.9 ± 0.5	28.6 ± 1.3	ND[a]	ND	1.6 ± 0.5

[a] Element not detected.

(29.04 amu), $C_3H_7^+$ (43.05 amu), and $C_4H_9^+$ (57.07 amu) and contaminants such as poly(dimethylsiloxane) (PDMS) peaks, $C_5H_{15}OSi_2^+$ (147.06 amu). In the negative mass mode, the calibration was based on CH^- (13.01 amu), C_2H^- (25.01 amu), C_3H^- (37.01 amu), and C_4H^- (49.01 amu). Relative normalized intensities were determined by dividing each peak of the spectra by the total measured intensity minus hydrogen, sodium, and contaminant peaks intensities.

Results and Discussion

Table 1 shows the chemical surface composition of native polished titanium (Ti-P) samples. Beside the expected elements of the titanium oxide, Ti and O, the contaminants C and N were also observed.

The high-resolution spectrum of the Ti 2p peak (Figure 1a) showed three peaks in the spectrum. After peak fitting, the dominant doublet was assigned to TiO_2, with Ti 2p3/2 at a binding energy (BE) of 458.8 eV and Ti 2p1/2 at BE 464.5 eV.[31,32] The difference of 5.7 eV in BE between those two peaks of TiO_2 corresponds well to the literature values (ΔE from 5.5 to 5.8 eV).[31,33−35] The low-energy peak was assigned to metallic Ti with an observed BE for the 2p 3/2 of 453.7 eV and consequently at 6.1 eV higher BE (459.8 eV) the 2p 1/2 contribution.[31,32] The presence of this peak, believed to come from the underlying bulk metal, indicates that the surface oxide was thinner than the probing depth of the XPS. In addition, a small contribution (2.7%) of Ti^{3+} (Ti 2p3/2 at BE 457.4 eV) from substoichiometric oxide, Ti_2O_3, was present, as also reported in several XPS studies.[31,36−38]

In the O 1s core line (Figure 1b), three O contributions were fitted and assigned according to literature values.[32,39,40] The first, assigned to O atoms in TiO_2, was fitted with a peak of 1.2 eV fwhm at a binding energy of 530.3 eV (literature values range from 529.9 to 530.9 eV[41]). A second peak at 1.3 eV higher BE (ca. 531.6 eV) is attributed to either surface termination oxygen[40,42] or to acidic *O*H (bridging OH groups),[43] as well as to carbonyl groups (O═

(31) Aronsson, B.-O.; Krozer, A.; Lausmaa, J.; Kasemo, B. *Surf. Sci. Spectra* **1996**−**97**, *4*, 42.
(32) Bertóti, I.; Mohai, M.; Sullivan, J. L.; Saied, S. O. *Appl. Surf. Sci.* **1995**, *84*, 357−371.
(33) Ong, J. L.; Prince, C. W.; Lucas, L. C. *J. Biomed. Mater. Res.* **1995**, *29*, 165−172.
(34) Kilpadi, D. V.; Raikar, G. N.; Liu, J.; Lemons, J. E.; Vohra, Y.; Gregory, J. C. *J. Biomed. Mater. Res.* **1998**, *40*, 646−659.
(35) Zhang, F.; Zheng, Z.; Chen, Y.; Liu, X.; Chen, A.; Jiang, Z. *J. Biomed. Mater. Res.* **1998**, *42*, 128−133.
(36) Sodhi, R. N. S.; Weninger, A.; Davies, J. E.; Sreenivas, K. *J. Vac. Sci. Technol.* **1991**, *A9*, 1329−1333.
(37) Olefjord, I.; Hansson, S.; Eng, L. *Int. J. Oral Maxillofac. Impl.* **1993**, *8*, 32−40.
(38) Sittig, C.; Textor, M.; Spencer, N. D.; Wieland, M.; Valloton, P.-H. *J. Mater. Sci.: Mater. Med.* **1999**, *10*, 35−46.
(39) Beamson, G.; Briggs, D. *High-resolution XPS of organic polymers*; *The Scienta ESCA300 Database*; John Wiley & Sons Ltd.: Chichester, U.K., 1992.
(40) Lu, G.; Bernasek, S. L.; Schwartz, J. *Surf. Sci.* **2000**, *458*, 80−90.
(41) Carley, A. F.; Roberts, J. C.; Roberts, M. W. *Surf. Sci.* **1990**, *225*, L39−L41.
(42) Azoulay, A.; Shamir, N.; Fromm, E.; Mintz, M. H. *Surf. Sci.* **1997**, *370*, 1−16.

Table 2. Chemical Composition (at. %) after Grafting of the MDP, PTP, and ETP Phosphonates on the Ti P Surface

	Ti 2p	O 1s	C 1s	P 2p	Ca 2p	N 1s
Ti P + MDP	17.8 ± 0.5	57.3 ± 1.0	22.3 ± 1.2	2.3 ± 0.5	ND[a]	ND
Ti P + PTP	17.3 ± 1.5	52.6 ± 0.5	25.8 ± 0.5	2.8 ± 0.5	ND	1.5 ± 0.5
Ti P + ETP	17.0 ± 0.5	54.4 ± 0.5	24.1 ± 0.5	3.0 ± 0.5	ND	1.5 ± 0.5

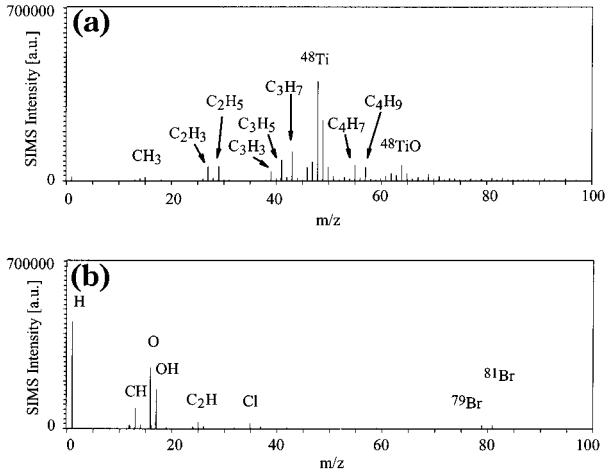

Figure 2. (a) Positive ion ToF-SIMS spectrum of a Ti P disk ($0 < m/z < 100$) and (b) negative ion ToF-SIMS spectrum of a Ti P disk ($0 < m/z < 100$).

C; e.g. in carboxyl molecules).[39] The third oxygen peak at 3.0 eV higher BE (ca 532.9 eV) is attributed to basic hydroxyl groups[43] and chemisorbed water,[40,44] as well as to ether groups (C−O).[1,39,45−47] Their fwhm values were 1.4 and 1.35 eV, respectively. However, in the literature some ambiguities exist in the assignment of these peaks, and the real amount of −OH present on the titanium dioxide surface is disputed.[40]

From the high-resolution spectra of the carbon C 1s signal (Figure 1c), four peaks were fitted and attributed according to the literature.[28,39,48−52] The peaks were accordingly assigned to the following: C_0, *C*−*C* and *C*−H; C_1, *C*-O; C_2, *C*═O; C_3, O−*C*═O (x in C_x is the number of oxygen bonds), respectively. The main peak, C_0, was at 285.0 eV (fwhm 1.2 eV) with the subsequent peaks showing shifts of $C_1 + 1.5$ (fwhm 1.25 eV), $C_2 + 3.0$ (fwhm 1.25 eV), and $C_3 + 4.1$ eV (fwhm 1.25 eV) and with relative intensity ratios C_0:C_1:C_2:C_3 = 78.7:12.8:4.8:3.7 (%).

Nitrogen was also observed at low concentrations (from 1% to 2%) on some samples. The peak was located at 400.6 eV, which corresponds to N atoms involved in, e.g., −C*N*, −*N*H_2, −*N*H_3, −OCO*N*H, and −CO*N*H_2 groups, and is attributed to traces of organic contaminants (the corresponding contributions in the C− and O− peaks are not distinguishable).[43]

Figure 2a shows the positive-ion ToF-SIMS spectrum of the bare Ti where the highest peak observed at m/z = 48 is from $^{48}Ti^+$. Other peaks are easily identified as titanium isotopes (m/z = 46, 47, 49, and 50) and corresponding protonated ions, TiH^+, at m/z = 47, 48, 49, 50, and 51, as well as the corresponding series of TiO^+ peaks (m/z = 62, 63, 64, 65, and 66). They agree well with the literature data.[53−56] Further peaks identified are typical from hydrocarbon contamination such as $(C_nH_{2n+1})^+$ and $(C_nH_{2n-1})^+$ and minor contributions from oxygen-containing species. At higher masses, additional minor contaminants were observed, such as phthalate (m/z = 149, $C_5O_5H_9^+$) (results not shown).

The corresponding negative ion ToF-SIMS spectrum (Figure 2b) is dominated by the O^- ion, at m/z = 16, and OH^-, at m/z = 17, typical for hydroxylated titanium oxide surfaces.[57] Some hydrocarbon peaks were also observed (m/z = 13 and 25, CH^- and C_2H^-, respectively), as well as a few contaminants such as Cl^- (m/z = 35 and 37) and Br^- (m/z = 79 and 81).

Grafting of Phosphonic Acids. After surface analysis, the same Ti disks were modified with the three phosphonic acids (MDP, PTP, and ETP) and again analyzed with XPS and ToF-SIMS. Results of the chemical composition from XPS analyses are given in Table 2. Beside the previously detected elements on the Ti reference substrate, phosphorus was observed, confirming the presence of the phosphonic acids on the modified Ti substrates. The binding energies determined from peak fitting of the main peaks in the high-resolution spectrum (Figure 3) of a phosphonic acid (PTP) grafted on a Ti P disk, as well as their assignments, are summarized in Table 3. The high-resolution spectra of the Ti 2p peak showed the same composition as for the nonmodified surface, and only the Ti^{+IV} 2p3/2 peak is noted in the table for reference purposes.

The P 2p signal (Figure 3c) should theoretically be a nonresolved doublet with 2p1/2 and 2p3/2 components at ΔBE = 0.8 eV (fitted at BE 134.2 and 133.4 eV, respectively) and area ratio of 1:2. Gawalt et al.[58] studied the surface of an alkane phosphonic acid complexed with zirconium which was grafted on the native oxide of a Ti plate (TiO_2) and found a single P 2p peak (not peak fitted) at BE 133.0 eV, while Textor et al.[59] found a variation in the P 2p BE (132.4 to 135.8 eV) as a function of the O environment. Grafted to a tantalum oxide surface, the BE was ca. 134 eV. Nefedov reported a 1.2 eV lowering in the P 2p BE when the P−OH bond (at ca. 134.5 eV) in, e.g., $CH_3P(O)(OH)_2$, is replaced by a P−C bond, as in $Ph_2P(O)OH$ (133.3 eV), and a slight increase when complexed with transition metals.[60] A corresponding shift (1.7 to 2.1

(43) Sham, T. K.; Lazarus, M. S. *Chem. Phys. Lett.* **1979**, *68*, 426−432.
(44) Hanawa, T.; Hiromoto, S.; Asami, K. *Appl. Surf. Sci.* **2001**, *183*, 68−75.
(45) Healy, K. E.; Ducheyne, P. *Biomaterials* **1992**, *13*, 553−561.
(46) Meng, L.-J.; Sà, C. P. M. d.; Santos, M. P. d. *Thin Solid Films* **1994**, *239*, 117−122.
(47) Browne, M.; Gregson, P. J.; West, R. H. *J. Mater. Sci.: Mater. Med.* **1996**, *7*, 323−329.
(48) Favia, P.; Vulpio, M.; Marino, R.; d'Agostino, R.; Mota, R. P.; Catalano, M. *Plasmas Polym.* **2000**, *5*, 1−14.
(49) Johnston, E. E.; Ratner, B. D. *J. Electron Spectrosc. Relat. Phenom.* **1996**, *81*, 303−317.
(50) Ameen, A. P.; Short, R. D.; Johns, R.; Schwach, G. *Clin. Oral. Impl. Res.* **1993**, *4*, 144−150.
(51) Nanci, A.; Wuest, J. D.; Peru, L.; Brunet, P.; Sharma, V.; Zalzal, S.; McKee, M. D. *J. Biomed. Mater. Res.* **1998**, *40*, 324−335.
(52) Ratner, B. D. *Ann. Biomed. Eng.* **1983**, *11*, 313−336.
(53) Ameen, A. P.; Short, R. D.; Douglas, C. W. I.; Johns, R.; Ballet, B. *J. Mater. Sci.: Mater. Med.* **1996**, *7*, 195−199.
(54) Haddow, D. B.; James, P. F.; Noort, R. v. *J. Mater. Sci.: Mater. Med.* **1996**, *7*, 255−260.
(55) Morstein, M.; Karches, M.; Bayer, C.; Casanova, D.; Rohr, P. R. v. *Chem. Vap. Deposition* **2000**, *6*, 16−20.
(56) Weber, M.; Vasella, A.; Textor, M.; Spencer, N. D. *Helv. Chim. Acta* **1998**, *81*, 1359−1372.
(57) Takeda, S.; Fukawa, M.; Hayashi, Y.; Matsumoto, K. *Thin Solid Films* **1999**, *339*, 220−224.
(58) Gawalt, E. S.; Lu, G.; Bernasek, S. L.; Schwartz, J. *Langmuir* **1999**, *15*, 8929−8933.
(59) Textor, M.; Ruiz, L.; Hofer, R.; Rossi, A.; Feldman, K.; Hahner, G.; Spencer, N. D. *Langmuir* **2000**, *16*, 3257−3271.
(60) Nefedov, V. I.; Buslaev, Y. A.; Kuznetso, A. A.; Yankina, L. F. *Zh. Neorg. Khim.* [*Russ. J. Inorg. Chem.*] **1974**, *19*, 1416−1417.

Table 3. XPS Binding Energies, BE (from Peak Fitting), of the Main Elements Observed at the PTP-Grafted Ti P Disk

	core level							
	Ti 2p3/2	O 1s			C 1s		P 2p	
BE (eV)[a]	459.1	530.6	531.8	533.1	285.0	286.4	133.4	134.2
assgnt	*Ti*O_2	TiO_2	OH	P−*O*	CH	*C*−O	P 2p3/2	P 2p1/2
			(P═*O*)	OC		*C*−P	*P*−C	
			(*O*═C)	H_2O			*P*−O	

[a] All BE values are varying from sample to sample with ca. ±0.2 eV.

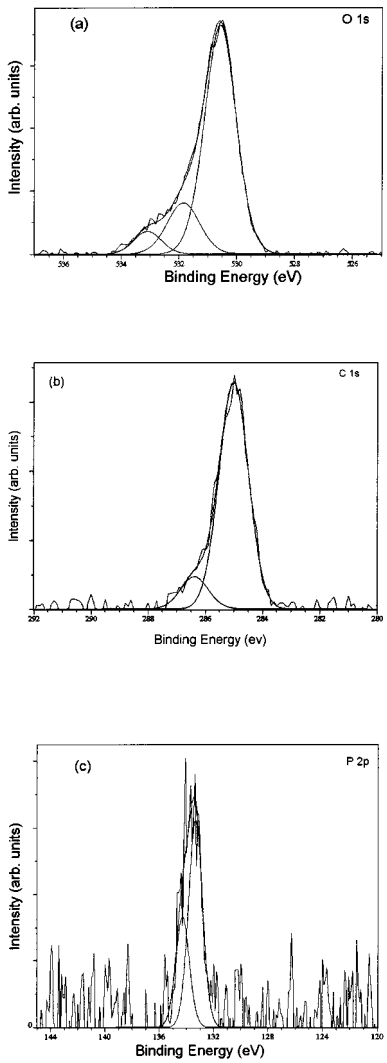

Figure 3. High-resolution XPS spectra of PTP-grafted Ti-P surface: (a) O 1s; (b) C 1s; (c) P 2p.

eV) in the C 1s peak BE (286−286.3 eV for $-PCH_3$ and 287.7−288.4 eV for $-POCH_3$) was recently reported.[61] Accordingly, since the C 1s peak (Figure 3b) could be fitted with only the two components representing C_0 (at 285.0 eV) and C_1 plus P−*C* (at 286.4 eV), it is concluded that most of the surface contaminants containing unsaturated carbons (i.e. carbonyl groups) were either saturated by or exchanged with the adsorbed phosphonate molecules, containing only CC−, CH−, and CP− groups.

In the O 1s spectrum (Figure 3a) peak fitting was again done with three components with the same BE values as before grafting of the phosphonic acids, with the main component assigned to titanium oxide. In addition to the above-mentioned attributions, further peak contributions were also related to the phosphonic acid molecule. Literature values for P═O groups are at BE 534.5−535 eV[61] in phosphonic and phosphoric acids, while BE was reported to be 532.1 eV in octadecylphosphoric acid.[59] This discrepancy in BE might be due to interactions with water (adsorption was done from liquid phase in the former case), stabilizing the P═O group. However, on adsorption from gas phase, the author found only one peak at 533 eV, corresponding to a single bond between P and O.[61] For P−*O* groups a BE of 533−533.6 eV has been published.[59,61] The presence of a peak at ca. 533.1 eV and the absence of the high BE (534.5 eV) peak in our spectra as well as in those from Textor et al.[59] indicate the covalency in the phosphonate−oxide surface interaction with only P−O bonds. The relatively high intensity of a peak at 531.8 eV, together with the absence of a C_2 peak at 288.0 eV, indicates the presence of hydroxyl groups but no carbonyl groups.

Table 4. Negative Secondary Ions Containing P and/or Ti Atoms Observed at the MDP-Modified Ti Surface

secondary ion mass (*m*/*z*) (detected)	possible assgnt	deviation of the detected mass (mamu)[a]	normalized intensity[b]
46.9679	PO	0.7	1.05
59.9661	CH(PO) or CPOH	10.4	1.12
62.9635	PO_2	0	18.53
78.959	PO_3	−0.5	17.61
79.9363	TiO_2	1.4	0.19
96.9404	TiO_2OH	0	0.55
126.9067	$TiOPO_2$	−0.3	0.12
142.901	TiO_2PO_2 or $TiOPO_3$	0.3	0.50
158.8967	TiO_2PO_3	−0.5	0.43
189.8699	$TiO(PO_2)_2$	0.1	0.10
205.8624	$TiO_2(PO_2)_2$	2.5	0.12
219.8805	$TiO_2(PO_2)_2CH_2$	0	0.097
221.8597	$TiO(PO_3)_2$	0	0.12

[a] mamu: milliatomic mass units. [b] Relative normalized intensity (‰) determined by dividing each peak of the spectrum by the total measured intensity minus hydrogen, sodium, and contaminant peak intensities.

After modification of the Ti disks with phosphonic acids, no significant change was noticed in the positive secondary ions ToF-SIMS spectra compared to the unmodified Ti disk.

However, characteristic peaks of the grafting were observed in the negative secondary ion ToF-SIMS spectra. They were identical for all samples with minimal differences in their normalized intensity. As an example, the negative fragments detected on Ti P + MDP associated with either P or Ti are enumerated in Table 4. The ions with $m/z = 47, 63$, and 79 correspond to the fragmentation of the phosphonic acid groups, i.e., PO^-, PO_2^-, and PO_3^-, providing evidence of the presence of the acid on the surface, while the presence of fragments such as $TiOPO_2^-$, $TiO_2PO_2^-$ or $TiOPO_3^-$, $TiO_2PO_3^-$, $TiO(PO_2)_2^-$, $TiO(PO_2)_2CH_2^-$, and $TiO(PO_3)_2^-$ demonstrated the P−O−Ti bonding. Similar fragments were detected on tantalum oxide surfaces modified with self-assembled monolayer of octadecylphosphoric acid (ODP).[59] Some of the typical negative fragments showing the grafting of ODP on tantalum oxide were $TaOPO_3^-$, $TaOPO_4^-$, $TaO_2PO_4H^-$,

(61) Davies, P. R.; Newton, N. G. *Appl. Surf. Sci.* **2001**, *181*, 296−306.

Table 5. Chemical Composition (at. %), Ca:P Ratios, and Ca:Ti Ratios of Modified and Unmodified Ti P Surfaces after Incubation in HBSS for 1, 7, and 14 days

	Ti 2p	O 1s	C 1s	P 2p	Ca 2p	Na 1s	N 1s	Mg 2p	Zn 2p	Ca:P	Ca:Ti
					HBSS 1d						
Ti P	18.5	48.8	27.5	0.8	0.7	1.1	1.8	ND[a]	0.5	0.86	0.04
Ti P + MDP	19.4	51.8	22.7	0.9	0.8	2.4	1.1	0.4	ND	0.90	0.04
Ti P + PTP	18.7	48.3	26.8	1.3	1.1	2.0	1.0	ND	ND	0.86	0.06
Ti P + ETP	18.4	48.2	27.6	1.4	1.0	1.3	1.4	ND	0.5	0.71	0.05
					HBSS 7d						
Ti P	21.7	50.8	19.8	0.9	0.8	2.4	0.7	2.4	0.4	0.86	0.04
Ti P + MDP	21.5	51.4	19.9	1.2	0.8	1.8	0.6	2.1	0.4	0.90	0.04
Ti P + PTP	19.8	50.3	21.0	2.0	1.2	2.2	0.7	2.5	ND	0.86	0.06
Ti P + ETP	20.6	50.4	21.4	1.4	1.0	1.5	0.7	2.4	ND	0.71	0.05
					HBSS 14d						
Ti P	18.3	49.5	24.1	1.3	1.4	1.1	0.5	2.9	0.8	1.05	0.08
Ti P + MDP	17.3	48.8	26.4	1.3	1.5	1.2	0.4	2.6	0.4	1.19	0.09
Ti P + PTP	18.2	50.8	24.0	1.9	1.5	1.2	0.5	3.0	0.4	0.79	0.08
Ti P + ETP	15.2	48.3	27.7	1.6	1.7	1.3	0.6	2.9	0.6	1.07	0.11

and $TaO(PO_4)(PO_4H)^-$. Taking these results together with the XPS results, these authors concluded that a strong P−O−Ta bonding was formed.

Langmuir isotherms were also performed on TiO_2 anatase powder modified with MDP. An equilibrium constant of 2.09×10^4 l/mol with bidistilled water as solvent was found.[62] All these results indicate the formation of a strong P−O−Ti bonding.

Incubation in HBSS. After grafting of the phosphonic acids, the modified and unmodified Ti substrates were incubated in HBSS for 1, 7, and 14 days and once again analyzed with XPS and ToF-SIMS. Table 5 gives the chemical composition determined from XPS. All values for Ti, O, and C had variations on the order of ca. ±2 at. %, while for the other elements the variations were on the order of ±0.3 at. %. After 1 day of incubation, a deposition from the solution can be observed. Calcium, sodium, and on the MDP modified surface also magnesium were detected. It could also be noticed that Ti was detected at unaltered concentrations, which indicates that the thickness of the deposition does not exceed a few molecular monolayers.

As an example, the binding energies of O, C, P, and Ca of Ti P + PTP + HBSS 14d (14 days) are given hereafter. In the O 1s core line, three O peaks were fitted. The lowest, at a BE of 530.4 eV (67.3%), was again attributed to TiO_2. At BE 531.7 eV (23.2%), the reported value for oxygen in carbonyl groups is also the BE associated with the phosphate group (PO_4^{3-}) and hydroxyls in calcium phosphates. Beside being the binding energy for oxygen in the phosphonate group, the peak at 532.9 eV (9.5%) is characteristic of oxygen in the hydrogenophosphate group (HPO_4^{2-}), (intercrystalline) water,[63−65] and ether groups. The fwhm values for the last two peaks were 1.4 and 1.35 eV, respectively. As for the unmodified sample surface, Ti-P, four peaks were used to fit the C 1s spectrum. The concentration ratios observed for C_0:C_1:C_2:C_3 were 78.9: 13.8:4.6:2.8 (%). The binding energies of the fitted P 2p peak (Figure 4c) were again 134.1 and 133.3 eV and were attributed to P 2p1/2 (33.5%) and to P 2p3/2 (66.5%), respectively ($\Delta E = 0.8$ eV), from P bound to O and C in both the phosphonic acids[59,60] and the phosphates from the HBSS.[66−70] In addition to the above-mentioned peaks, a doublet from Ca is detected in the spectrum after incubation in HBSS. The binding energies of the two Ca 2p peaks were 347.4 eV, for Ca 2p3/2, and 350.9 eV, for Ca 2p1/2, respectively (Figure 4d).

The Ca/P ratios on all Ti P surfaces are summarized in Table 5. From these data an attempt to characterize the calcium phosphate growth in both quantitative and qualitative manners was done. However, due to the presence of phosphonic acid, the Ca:Ti ratio (and not the usual Ca:P ratio) was used to quantify the growth, while the Ca:P ratio of the reference Ti P disk was used to suggest the nature of the calcium phosphate. An increase in the Ca:Ti ratio with increased incubation time is observed both in the XPS (Table 5) and ToF-SIMS (Table 6) data for all surfaces. However not statistically significant, the amount of Ca was after 1 and 7 days of incubation higher on the PTP-modified surface than on the other surfaces, while after 14 days the ETP-modified surface showed the highest Ca concentration.

On the other hand, after 14 days of incubation in HBSS, the Ca:P ratio reached 1 for the Ti P + HBSS and the Ti P + ETP + HBSS surfaces and even 1.2 for the Ti P + MDP + HBSS surface, while it remained low for the Ti P + PTP + HBSS surface. These Ca:P ratios are nevertheless still lower than for stoichiometric hydroxyapatite (1.67), and variations between samples were relatively large (±0.2). The calcium phosphate coating on the Ti disks was probably similar to monetite ($CaHPO_4$, Ca:P = 1) or brushite ($CaHPO_4 \cdot H_2O$, Ca:P = 1). Magnesium, which was also present in the calcium phosphate coating, as detected by XPS and ToF-SIMS, probably substituted the Ca^{2+} and contributes to lower the Ca:P ratio, as also found recently by Li et al.[71] and Wen et al.[72]

Beside the detected peaks in the positive ion ToF-SIMS spectra of the grafted surface, some cations present in HBSS were observed on the topmost part of the different Ti surfaces (Figure 5). They appeared at $m/z = 23$, 24, 39, and 40 and were attributed to Na^+, Mg^+, K^+, and Ca^+, respectively. Peaks related to calcium were also found at

(62) Viornery, C. *Surface functionalization of titanium with phosphonated ligands to improve bone bonding*; EPFL: Lausanne, Switzerland, 2000.
(63) Amrah-Bouali, S.; Rey, C.; Lebugle, A.; Bernache, D. *Biomaterials* **1994**, *15*, 269−272.
(64) Midy, V.; Rey, C.; Bres, E.; Dard, M. *J. Biomed. Mater. Res.* **1998**, *41*, 405−411.
(65) Soten, I.; Ozin, G. A. *J. Mater. Chem.* **1999**, *9*, 703−710.
(66) Hanawa, T. *Titanium and its oxide film: a substrate for formation of apatite*; Davies, J. E., Ed.; University Toronto Press: Toronto, Canada, 1991; pp 49−61.
(67) Hanawa, T.; Ota, M. *Biomaterials* **1991**, *12*, 767−774.
(68) Landis, W. J.; Martin, J. R. *J. Vac. Sci. Technol., A* **1984**, *2*, 1108−1111.
(69) Ong, J. L.; Lucas, L. C.; Raikar, G. N.; Connatser, R.; Gregory, J. C. *J. Mater. Sci.: Mater. Med.* **1995**, *6*, 113−119.
(70) Ferraz, M. P.; Monteiro, F. J.; Santos, J. D. *J. Biomed. Mater. Res.* **1999**, *45*, 376−383.
(71) Li, P.; Ducheyne, P. *J. Biomed. Mater. Res.* **1998**, *41*, 341−348.
(72) Wen, H. B.; Wijn, J. R. d.; Cui, F. Z.; Groot, K. d. *J. Biomed. Mater. Res.* **1998**, *41*, 227−236.

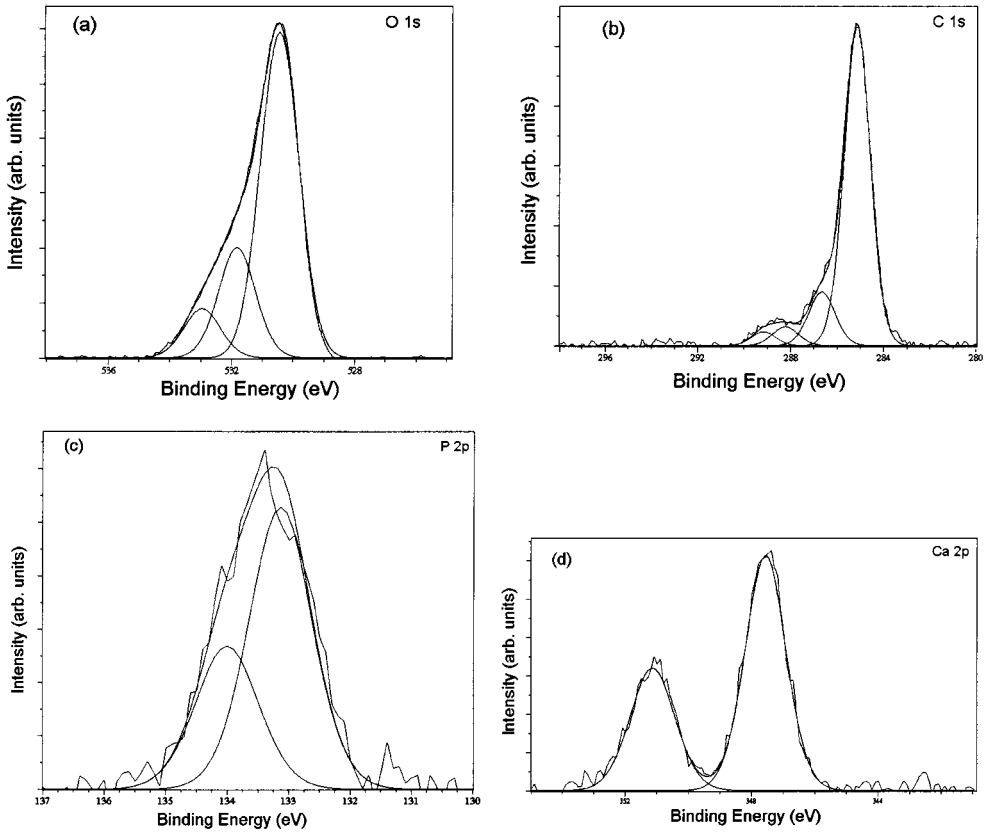

Figure 4. High-resolution XPS spectra of PTP-grafted Ti-P surface after 14 days incubation in HBSS solution: (a) O 1s; (b) C 1s; (c) P 2p; (d) Ca 2p.

Table 6. Ca:Ti Ratio from ToF-SIMS Analyses of Modified and Unmodified Ti P Surfaces after Incubation in HBSS for 7 and 14 days

	Ca:Ti	
	HBSS 7d	HBSS 14d
Ti P	0.50	0.86
Ti P + MDP	0.60	0.72
Ti P + PTP	0.73	1.01
Ti P + ETP	0.62	1.03

$m/z = 41$, 56, and 57 and were attributed to CaH^+, CaO^+, and $CaOH^+$, respectively. These peaks are characteristic of calcium phosphate adsorption.[73−75]

Table 6 reports the Ca:Ti ratio (from ToF-SIMS data) after 7 and 14 days of incubation in HBSS. The Ca:Ti ratio increased with the incubation time, and two modified Ti surfaces exhibited higher calcium level compared to the reference Ti P surface, which is in agreement with the XPS results. The discrepancies in the absolute values between the Ca/Ti ratios measured by XPS in Table 5 and those measured by ToF-SIMS are mainly due to the difference in measuring techniques. While the former is sensible to a volume of the sample with the depth of around 5 nm, the latter is only sensitive the outermost surface layers (<1 nm). Furthermore, the chemical environment has great influence on the intensities from ToF-SIMS (the so-called matrix effect), which makes it almost impossible today to make any quantitative estimations from the secondary ion spectra.

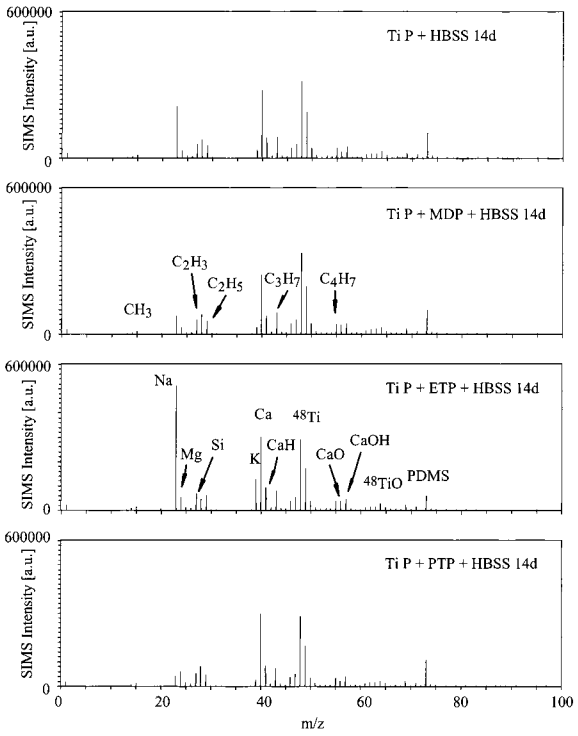

Figure 5. Positive ion ToF-SIMS spectra ($0 < m/z < 100$) of a Ti P and modified Ti P surfaces (Ti P + MDP, Ti P + ETP, and Ti P + PTP) after incubation in HBSS for 14 days.

On the other hand, the longer the incubation time was, the more contaminated the Ti surfaces were. Among the contaminants, signatures related to PDMS (such as $m/z = 28$ and 73 in Figure 5) were indeed observed. However, due to its lower surface sensitivity, the silicon contaminant

(73) Leadley, S. R.; Davies, M. C.; Ribeiro, C. C.; Barbosa, M. A.; Paul, A. J.; Watts, J. F. *Biomaterials* **1997**, *18*, 311−316.
(74) Chusuei, C. C.; Goodman, D. W.; Stipdonk, M. J. v.; Justes, D. R.; Schweikert, E. A. *Anal. Chem.* **1999**, *71*, 149−153.
(75) Lu, H. B.; Campbell, C. T.; Graham, D. J.; Ratner, B. D. *Anal. Chem.* **2000**, *72*, 2886−2894.

was not detected with XPS. PDMS is often detected with the ToF-SIMS technique on surfaces that are not cleaned in situ, and since it can only be speculated about its origin, we leave that discussion to another forum.

No significant change was noticed in the negative spectra after incubation in HBSS compared to the Ti disks after grafting of the phosphonic acids. The peaks characteristic of calcium phosphate adsorption were also PO_2^- and PO_3^-.[73−75]

Conclusions

The grafting of three phosphonic acids (MDP, PTP, and ETP) on polished Ti disks was studied with XPS and ToF-SIMS. Analyses results and Langmuir isotherms showed that a Ti−O−P bond was formed. The bioactivity ability of the modified Ti disks was tested by incubating these disks in HBSS, and the surface adsorption was studied as a function of time. While remaining small, the adsorption rate of calcium was higher on the modified surfaces compared to the reference (Ti P), and as a consequence, they induced better calcium phosphate growth. Among them, the Ti P + ETP surface seems to be the most favorable. These results indicate that the modification of Ti with phosphonic acids might be promising for various implant applications.

Acknowledgment. The authors want to thank Mr. N. Xanthopoulous for his skillful technical assistance. We also acknowledge the Institute Straumann AG (Waldenburg, Switzerland) for providing the Ti disks. This work has been financially supported by the Swiss National Science Foundation.

LA010908I

Exhibit A-6

NBMolecules®. Determination of SurfLink® Surface Treatment Thickness on Sterile SurfLink® Dental Implants by X-ray Photoelectron Spectroscopy (XPS). 2012.

Test report # 18f

Determination of SurfLink® surface treatment thickness on sterile SurfLink® Dental Implants by X-ray photoelectron spectroscopy (XPS)

NBM-P-402

Determination of SurfLink® surface treatment thickness on sterile SurfLink® Dental Implants by X-ray photoelectron spectroscopy (XPS)

NBMolecules® personnel: Sabrina Buchini and Richard Curno

XPS Analysis (June 2012): Roman Heuberger (RMS Foundation)

Objectives: By using X-ray photoelectron spectroscopy (XPS) the thickness of the SurfLink® layer on sterile SurfLink® Dental Implants will be determined.
Conclusions: The thickness of the SurfLink® layer on sterile SurfLink® Dental Implants is less than 1 nm.

Signed Sabrina Buchini Date 26 Jun 2012

Research Chemist

Signed [signature] Date 26/Jun/2012

Chief Technical Officer

Signed [signature] Date 2012-06-21

Chief Chemist

Table of Contents

Objectives

By using X-ray photoelectron spectroscopy (XPS) the thickness of the SurfLink® layer on sterile SurfLink® Dental Implants will be determined.

Materials and Methods

Sterile SurfLink® Dental Implants were manufactured according to NBMolecules® surface treatment protocol (see Appendix 1, P.2.3.5.D1 Lot File Release Form, LN 000,000,208).
Depth profiling by XPS involves combining sequences of ion gun sputtering cycles with XPS measurements. An ion gun is used to etch the material for a defined period of time before being turned off. XPS spectra are then acquired. Each sputtering cycle exposes a new surface, whose elemental composition can be analysed by XPS.
The depth profiles were performed using a Kratos AXIS Nova high resolution spectrometer. An Al-standard source was used for the measurement. Depth profile sputtering was performed by scanning a 3.8 keV Ar^+ beam at 100 µA extractor current over an area of 4 mm×4 mm. The sputter rate of Ta_2O_5 standards measured under these conditions (6 nm/min) was used to convert sputter time in approximate sputter depth. Please refer to Table 1 for sputtering conditions used in this experiment. Depth profiles were measured on 3 implants (see Appendix 2).

XPS raw data were analysed using CasaXPS version 2.3.1.4 and 'Relative Sensitivity Factors (RSF)' for the RMS-Kratos equipment. The spectra were manually integrated using pre-defined parameters and templates.

Results/Discussion

See Appendix 3 and 4 for details on XPS analysis.

The analyses of the depth profiles of the 3 implants were carried out separately due to the different sputtering times used for the 3 samples. The final results for the 3 implants were compared.

<u>Survey spectra</u>

Survey spectra were only measured before sputtering and after the final sputtering cycle.

The expected elements ('O', 'C', 'Ti' and 'P') were observed in the survey spectra before sputtering. Furthermore the surveys were inspected for other elements contaminations and their contribution was determined to be ≤ 1.2% ('N').

After the final sputtering cycle only 'O', 'C' and 'Ti' were detected on the implant surfaces.

High resolution spectra

High resolution spectra of 'O', 'C', 'Ti' and 'P' were measured at defined sputtering times (Table 1).

Table 1: *Sputtering conditions (x= XPS analysis point performed).*

sec	**0**	**5**	**10**	**15**	**20**	**30**	**40**	**60**	**105**
nm	**0.0**	**0.5**	**1.0**	**1.5**	**2.0**	**3.0**	**4.0**	**6.0**	**10.5**
Implant 1	×	×		×		×		×	×
Implant 2	×		×		×		×		
Implant 3	×	×		×		×			

Due to the limitation of the experimental method, the XPS depth profile analyses were carried out on the implants tip where a flat area of ca 4 mm×4 mm is found.

The results show that 'P' binds to the outermost surface of the implant and the peak disappears within 10 seconds of sputtering. As shown in 'NBM-P-402: Chemical characterization of the sterile SurfLink® Dental Implant surface by X-ray photoelectron spectroscopy (XPS)' report, 'P' detected on the implant surface indicates the presence of the SurfLink® molecule. The results from the depth profile of all of the 3 implants indicated that the thickness of the SurfLink® layer is consistently less than 1nm.

'O' is still present after 105 seconds of sputtering, suggesting a titanium oxide layer with a thickness greater than 10.5 nm.

Following several sputtering cycles, 'Ti' is mostly present as titanium metal, as confirmed by a shift in the position of the main peak (from 459 to 454 eV).

'C' is mostly removed from the implant surface within 10 seconds of sputtering. The traces left-over after the last sputtering cycle are consistent with titanium carbide (chemical shift: 282 eV). If not initially present, as it is the case for the 3 analysed samples, titanium carbide is most likely formed during the analysis. The titanium metal exposed after ion bombardment readily reacts with hydrocarbons present in the machine.

High resolution spectra – components

The components were assigned according to Mani *et al.* (Langmuir, **2008**, *24*, 6774-6784) and Viornery *et al.* (Langmuir, **2002**, *18*, 2582-2589):

O1: metal oxides; O2: Metal-OH, C=O, P=O, Metal-O-P; O3: H_2O, C-OH, P-OH.
C1: C-C, C-H; C2: C-O, H_3C-P; C3: C=O, H_3C-O-P; C4: O-C=O; C5: C-metal.
Ti1: TiO_2; Ti2: Ti metal; Ti3: Ti_2O_3; Ti4: TiO.

From the components analysis, the following observations can be drawn:

- an increase of the metal 'Ti' component (i.e. Ti2) is observed.
- an increase of the metal carbide component (C5) is observed

These observations are in agreement with the high resolution results.

Conclusions

The thickness of the SurfLink® layer on sterile SurfLink® Dental Implants is less than 1 nm.

Appendix 1: Lot File LN 000,000,208

See Appendix 1 of 'NBM-P-402: Chemical characterization of the sterile SurfLink® Dental Implant surface by X-ray photoelectron spectroscopy (XPS)'

Appendix 2: Laboratory notes (LBN-006 p.96)

TITLE XPS depth profile - Thickness **PROJECT** NBM-P-402

Continued From Page Start

07 May 2012

The following samples were sent to RMS for XPS depth profiling (P0120548).

3 x PN 100, 397, LN 000, 000, 208 (Steele)

1 analysis point / implant.

Results compiled in XFRN 0,062.

NBM

Implants returned to ~~NMB~~(A) on 07 June 2012.

Implants stored in 'used RAD storage cupboard'

SBrC

08 June 2012

CERTIFIED COPY

Signed: SBrC

Date: 20 Jun 2012

From: LBN-006 p-96
NBM-P-402

To: THICKNESS REPORT

Continued To Page Finish

SIGNATURE	DATE	PROPRIETARY AND CONFIDENTIAL INFORMATION
Stephanie Brocq	07 May 2012	
DISCLOSED TO AND UNDERSTOOD BY	DATE	
	12 Jan 2012	

(A) Ellen - SBrC - 07 June 2012

Appendix 3: XFRN 0,062

Appendix 3 of NBM-P-402 'Determination of SurfLink® surface treatment thickness on sterile SurfLink® Dental Implants by X-ray photoelectron spectroscopy (XPS)' is stored at NBMolecules® premises and available for viewing on site.

Appendix 4: Summary of XPS results

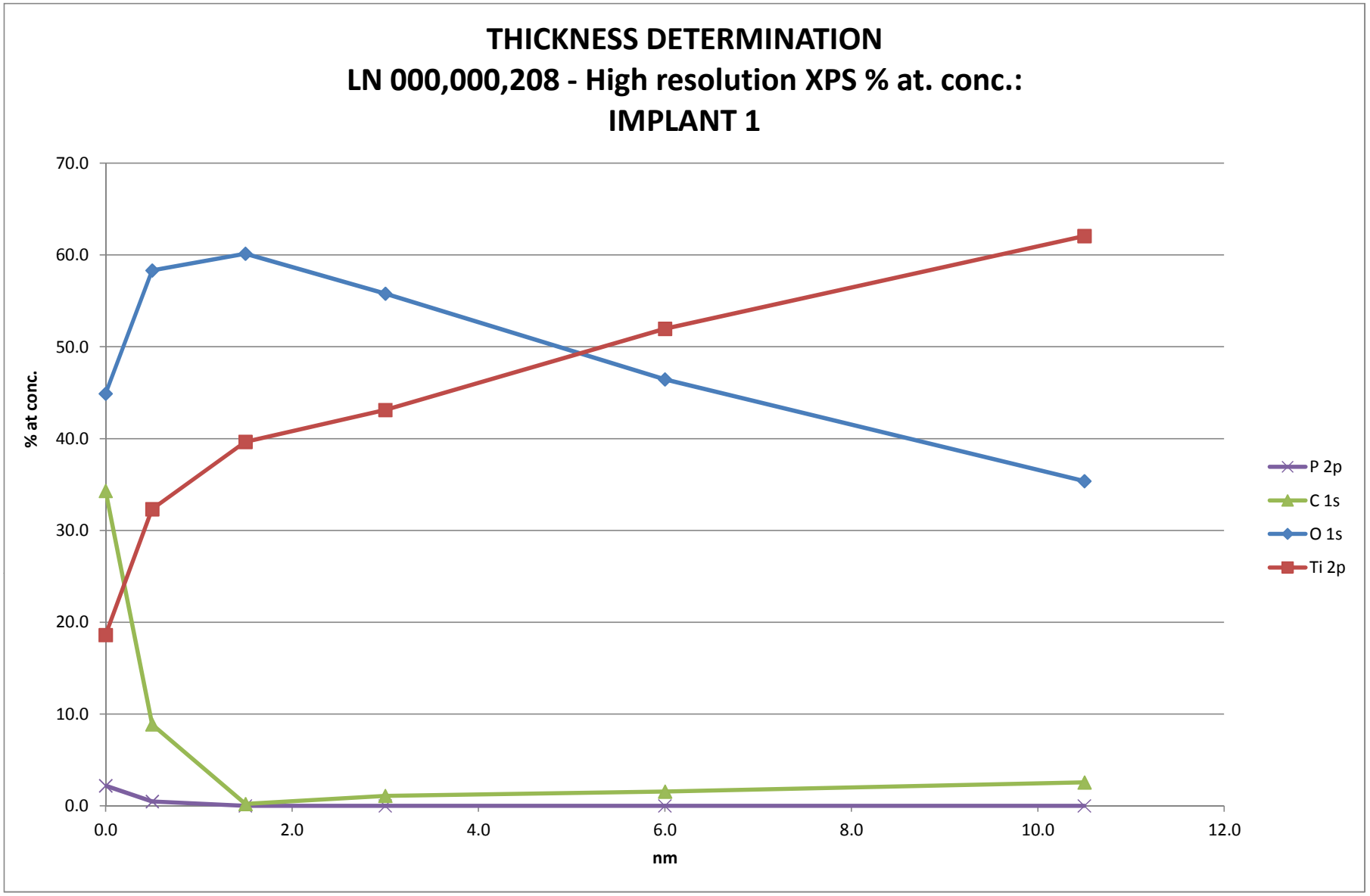
THICKNESS DETERMINATION
LN 000,000,208 - High resolution XPS % at. conc.:
IMPLANT 1
% at conc.
70.0
60.0
50.0
40.0
30.0
20.0
10.0
0.0
0.0
2.0
4.0
6.0
8.0
10.0
12.0
nm
P 2p
C 1s
O 1s
Ti 2p

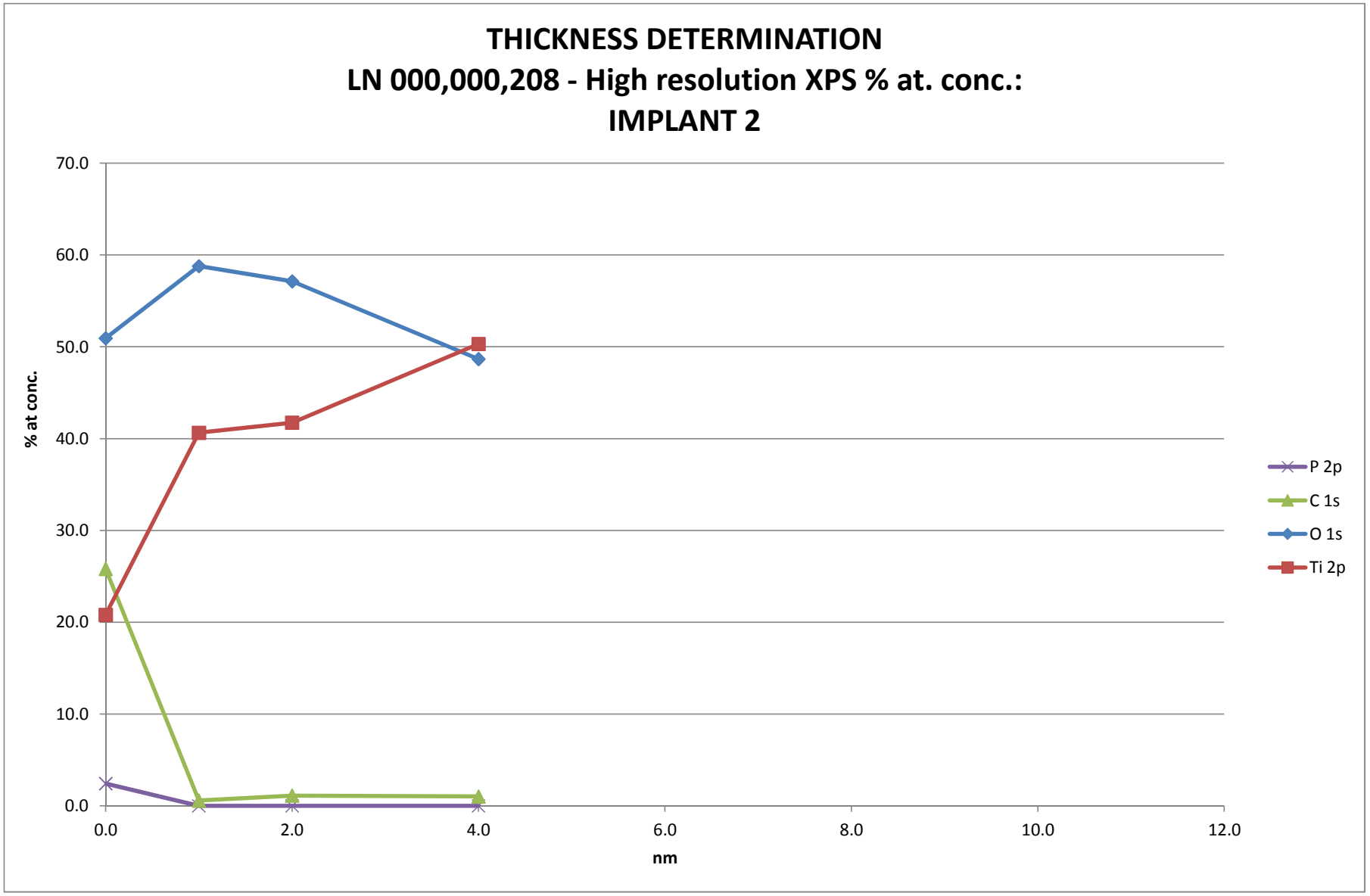
THICKNESS DETERMINATION
LN 000,000,208 - High resolution XPS % at. conc.:
IMPLANT 2
% at conc.
70.0
60.0
50.0
40.0
30.0
20.0
10.0
0.0
0.0
2.0
4.0
6.0
8.0
10.0
12.0
nm
P 2p
C 1s
O 1s
Ti 2p

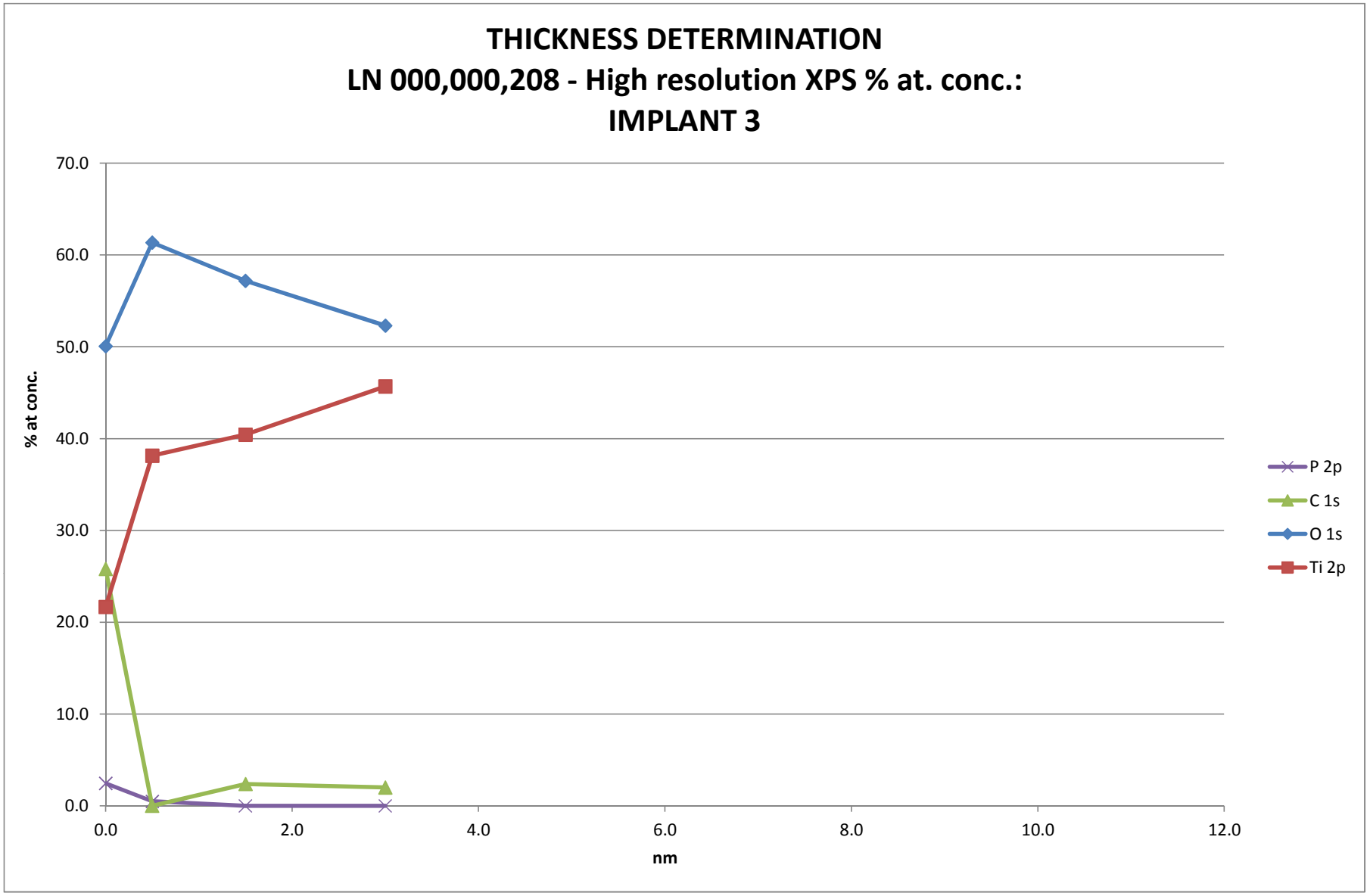
THICKNESS DETERMINATION
LN 000,000,208 - High resolution XPS % at. conc.:
IMPLANT 3
% at conc.
70.0
60.0
50.0
40.0
30.0
20.0
10.0
0.0
0.0
2.0
4.0
6.0
8.0
10.0
12.0
nm
P 2p
C 1s
O 1s
Ti 2p

Survey

	PN 100,397 LN 000,000,208					
	Implant 1		Implant 2		Implant 3	
	0s	105s	0s	40s	0s	30s
O 1s	45.3	35.1	51.3	50.8	50.9	55.1
C 1s	32.3	5.0	24.4	3.3	24.7	0.0
N 1s	1.2	0.0	1.1	0.0	1.1	0.0
Ti 2p	18.9	59.9	21.0	45.9	21.2	44.9
S 2p	0.0	0.0	0.0	0.0	0.0	0.0
P 2p	2.3	0.0	2.2	0.0	2.2	0.0
Ca 2p	0.0	0.0	0.0	0.0	0.0	0.0
Cl 2p	0.0	0.0	0.0	0.0	0.0	0.0
Na 1s	0.0	0.0	0.0	0.0	0.0	0.0
Si 2p	0.0	0.0	0.0	0.0	0.0	0.0
V2p	0.0	0.0	0.0	0.0	0.0	0.0
Al2s	0.0	0.0	0.0	0.0	0.0	0.0
K2p	0.0	0.0	0.0	0.0	0.0	0.0
Zn 2p3/2	0.0	0.0	0.0	0.0	0.0	0.0
Cu 2p 3/2	0.0	0.0	0.0	0.0	0.0	0.0
Pb 4f	0.0	0.0	0.0	0.0	0.0	0.0
Ni 2p 3/2	0.0	0.0	0.0	0.0	0.0	0.0
Co2p	0.0	0.0	0.0	0.0	0.0	0.0
Cr 2p	0.0	0.0	0.0	0.0	0.0	0.0
Fe2p3/2	0.0	0.0	0.0	0.0	0.0	0.0
Mo3d	0.0	0.0	0.0	0.0	0.0	0.0
Other elements SUM	1.2	0.0	1.1	0.0	1.1	0.0

SUM= N1s, S2p, Ca2p, Cl2p, Na1s, Si2p, F1s, K2p, V2p, Al2s, Zn2p, Cu2p,Pb4f, Ni2p, Co2p, Cr2p. Fe2p, Mo3d

High resolution - regions

	PN 100,397 LN 000,000,208													
	Implant 1						Implant 2				Implant 3			
sec	0.0	5.0	15.0	30.0	60.0	105.0	0.0	10.0	20.0	40.0	0.0	5.0	15.0	30.0
nm	0.0	0.5	1.5	3.0	6.0	10.5	0.0	1.0	2.0	4.0	0.0	0.5	1.5	3.0
O 1s	44.9	58.3	60.1	55.8	46.5	35.4	50.9	58.8	57.1	48.7	50.1	61.4	57.2	52.3
Ti 2p	18.6	32.3	39.7	43.1	52.0	62.1	20.8	40.6	41.7	50.3	21.7	38.1	40.4	45.7
C 1s	34.3	8.9	0.2	1.1	1.6	2.6	25.8	0.6	1.1	1.0	25.8	0.0	2.4	2.0
P 2p	2.2	0.5	0.0	0.0	0.0	0.0	2.4	0.0	0.0	0.0	2.5	0.5	0.0	0.0
P/Ti	0.12	0.02	0.00	0.00	0.00	0.00	0.12	0.00	0.00	0.00	0.11	0.01	0.00	0.00

N.B. Sputter rate 6 nm/min

High resolution - components

	PN 100,397 LN 000,000,208																			
	IMPLANT 1												IMPLANT 2							
sec	0		5		15		30		60		105		0		10		20		40	
nm	0		0.5		1.5		3		6		10.5		0		1		2		4	
Comp	A/(RSF*T*MFP)	Ratio	A/(RSF*T*MFP)	Ratio	A/(RSF*T*MFP)	Ratio	A/(RSF*T*MFP)	Ratio	A/(RSF*T*MFP)	Ratio	A/(RSF*T*MFP)	Ratio	A/(RSF*T*MFP)	Ratio	A/(RSF*T*MFP)	Ratio	A/(RSF*T*MFP)	Ratio	A/(RSF*T*MFP)	Ratio
O1	3848.33	0.52	4604.52	0.56	2896.96	0.38	2588.92	0.40	1685.09	0.40	1075.26	0.40	4295.89	0.45	3003.56	0.35	3656.79	0.46	3056.53	0.53
O2	2820.79	0.38	3121.14	0.38	3744.07	0.49	2973.84	0.46	2017.93	0.47	1163.34	0.43	4232.48	0.44	4597.13	0.53	3391.90	0.42	2030.39	0.35
O3	704.61	0.10	538.25	0.07	922.92	0.12	960.72	0.15	545.98	0.13	460.89	0.17	1090.21	0.11	1000.53	0.12	949.38	0.12	655.33	0.11
Ti 1	1394.46	0.69	911.27	0.29	773.51	0.23	774.10	0.23	285.19	0.09	107.81	0.03	1934.87	0.74	831.55	0.21	606.03	0.15	332.42	0.08
Ti 2p 1/2 1	698.45	n/a	456.43	n/a	387.43	n/a	387.72	n/a	142.85	n/a	54.00	n/a	969.12	n/a	416.50	n/a	303.54	n/a	166.50	n/a
Ti 2	148.49	0.07	120.81	0.04	462.87	0.14	833.73	0.24	1280.71	0.40	1814.27	0.56	186.08	0.07	425.72	0.11	745.45	0.19	1310.19	0.33
Ti 2p 1/2 met	74.38	n/a	60.52	n/a	231.87	n/a	417.64	n/a	641.55	n/a	908.83	n/a	93.21	n/a	213.26	n/a	373.42	n/a	656.32	n/a
Ti 3	293.52	0.14	1237.87	0.40	854.25	0.25	564.12	0.16	473.47	0.15	230.47	0.07	261.48	0.10	1207.77	0.30	854.12	0.22	631.65	0.16
Ti 2p 1/2 2	147.01	n/a	619.98	n/a	427.84	n/a	282.54	n/a	237.14	n/a	115.43	n/a	130.96	n/a	604.90	n/a	427.78	n/a	316.36	n/a
Ti 4	188.18	0.09	841.63	0.27	1291.08	0.38	1256.89	0.37	1202.27	0.37	1070.77	0.33	249.76	0.09	1556.24	0.39	1766.01	0.44	1725.02	0.43
Ti 2p 1/2 3	94.25	n/a	421.52	n/a	646.63	n/a	629.50	n/a	602.14	n/a	536.29	n/a	125.09	n/a	779.43	n/a	884.49	n/a	863.96	n/a
C1	3980.82	0.71	670.25	0.58	83.23	0.37	21.31	0.11	0.00	0.00	0.19	0.00	2858.63	0.59	49.98	0.35	28.80	0.15	24.84	0.13
C2	933.86	0.17	115.29	0.10	0.04	0.00	0.00	0.00	1.52	0.01	0.02	0.00	1121.84	0.23	0.02	0.00	3.80	0.02	10.72	0.06
C3	6.80	0.00	6.89	0.01	0.03	0.00	1.95	0.01	0.38	0.00	1.16	0.00	0.00	0.00	0.00	0.00	2.88	0.02	0.01	0.00
C4	657.25	0.12	140.89	0.12	0.06	0.00	0.12	0.00	0.43	0.00	0.34	0.00	877.46	0.18	3.06	0.02	0.29	0.00	0.79	0.00
C5	0.08	0.00	224.73	0.19	139.64	0.63	173.90	0.88	157.16	0.99	231.67	0.99	20.42	0.00	91.53	0.63	150.40	0.81	152.93	0.81

High resolution - components

	PN 100,397 LN 000,000,208 IMPLANT 3							
sec	0		5		15		30	
nm	0		0.5		1.5		3	
Comp	A/(RSF*T*MFP)	Ratio	A/(RSF*T*MFP)	Ratio	A/(RSF*T*MFP)	Ratio	A/(RSF*T*MFP)	Ratio
O1	3017.11	0.50	3681.67	0.57	3126.67	0.55	2466.94	0.51
O2	2704.06	0.45	2051.46	0.32	1872.89	0.33	1805.02	0.37
O3	347.09	0.06	733.96	0.11	719.40	0.13	589.45	0.12
Ti 1	1314.65	0.75	826.90	0.31	609.54	0.22	416.26	0.15
Ti 2p 1/2 1	658.47	n/a	414.17	n/a	305.30	n/a	208.49	n/a
Ti 2	152.31	0.09	191.53	0.07	525.63	0.19	805.04	0.28
Ti 2p 1/2 met	76.30	n/a	95.94	n/a	263.31	n/a	403.27	n/a
Ti 3	114.33	0.07	853.75	0.32	581.41	0.21	455.44	0.16
Ti 2p 1/2 2	57.26	n/a	427.59	n/a	291.19	n/a	228.10	n/a
Ti 4	162.68	0.09	835.04	0.31	1039.47	0.38	1179.37	0.41
Ti 2p 1/2 3	81.48	n/a	418.22	n/a	520.61	n/a	590.67	n/a
C1	1931.88	0.61	83.35	0.61	50.22	0.21	0.03	0.00
C2	538.42	0.17	0.00	0.00	0.07	0.00	0.63	0.00
C3	252.42	0.08	0.03	0.00	11.18	0.05	0.02	0.00
C4	420.36	0.13	0.03	0.00	0.44	0.00	0.03	0.00
C5	0.07	0.00	52.26	0.39	174.98	0.74	192.02	1.00

	IMPLANT 1						IMPLANT 2				IMPLANT 3			
sec	0.00	5.00	15.00	30.00	60.00	105.00	0.00	10.00	20.00	40.00	0.00	5.00	15.00	30.00
nm	0.00	0.50	1.50	3.00	6.00	10.50	0.00	1.00	2.00	4.00	0.00	0.50	1.50	3.00
O1	0.52	0.56	0.38	0.40	0.40	0.40	0.45	0.35	0.46	0.53	0.50	0.57	0.55	0.51
O2	0.38	0.38	0.49	0.46	0.47	0.43	0.44	0.53	0.42	0.35	0.45	0.32	0.33	0.37
O3	0.10	0.07	0.12	0.15	0.13	0.17	0.11	0.12	0.12	0.11	0.06	0.11	0.13	0.12
Ti 1	0.69	0.29	0.23	0.23	0.09	0.03	0.74	0.21	0.15	0.08	0.75	0.31	0.22	0.15
Ti 2p 1/2 1	n/a	n/a	n/a	n/a	n/a	n/a	n/a	n/a	n/a	n/a	n/a	n/a	n/a	n/a
Ti 2	0.07	0.04	0.14	0.24	0.40	0.56	0.07	0.11	0.19	0.33	0.09	0.07	0.19	0.28
Ti 2p 1/2 met	n/a	n/a	n/a	n/a	n/a	n/a	n/a	n/a	n/a	n/a	n/a	n/a	n/a	n/a
Ti 3	0.14	0.40	0.25	0.16	0.15	0.07	0.10	0.30	0.22	0.16	0.07	0.32	0.21	0.16
Ti 2p 1/2 2	n/a	n/a	n/a	n/a	n/a	n/a	n/a	n/a	n/a	n/a	n/a	n/a	n/a	n/a
Ti 4	0.09	0.27	0.38	0.37	0.37	0.33	0.09	0.39	0.44	0.43	0.09	0.31	0.38	0.41
Ti 2p 1/2 3	n/a	n/a	n/a	n/a	n/a	n/a	n/a	n/a	n/a	n/a	n/a	n/a	n/a	n/a
C1	0.71	0.58	0.37	0.11	0.00	0.00	0.59	0.35	0.15	0.13	0.61	0.61	0.21	0.00
C2	0.17	0.10	0.00	0.00	0.01	0.00	0.23	0.00	0.02	0.06	0.17	0.00	0.00	0.00
C3	0.00	0.01	0.00	0.01	0.00	0.00	0.00	0.00	0.02	0.00	0.08	0.00	0.05	0.00
C4	0.12	0.12	0.00	0.00	0.00	0.00	0.18	0.02	0.00	0.00	0.13	0.00	0.00	0.00
C5	0.00	0.19	0.63	0.88	0.99	0.99	0.00	0.63	0.81	0.81	0.00	0.39	0.74	1.00

Exhibit A-7

NBMolecules®. Optimization of the Surflink® Surface Treatment Process for MIS Implants. 2015.

Optimization of the SurfLink® surface treatment process for MIS implants

XPS Analysis: Roman Heuberger (RMS Foundation, Bettlach Switzerland)

Objectives:

Testing shall be carried out to optimize the SurfLink® surface treatment process for MIS implants, so that the maximum SurfLink® surface coverage is attained for the roughness and material characteristics of the MIS implant.

Conclusions:

Pre-treating MIS implants with a Deconex® solution at 60°C, followed by SurfLink® Surface Treatment with SurfLink® solution at 60°C, showed increased coverage of the implant surface with the SurfLink® molecule.

Other testing showed that the SurfLink® solution concentration can be varied from 0.7-7.0mM, without affecting the application of the SurfLink® molecule onto the implant surface. Furthermore, the dipping exhaustion experiments show that the same SurfLink® solution can be used for the treatment of multiple implants. This will allow a large degree of flexibility during manufacturing, and permit multiply racks of implants to be treated with the same bath of SurfLink® solution, reducing downtime incurred through the replenishment of SurfLink® treatment baths.

This optimized protocol for the treatment of MIS implants with SurfLink® should be validated on implants produced and SurfLink® treated at MIS manufacturing facilities.

Signed _____ Date 17 Apr 2015

Technical Manager

Signed _____ Date 17 Apr 2015

R&D Manager

Signed _____ Date 17 Apr 2015

Chief Technical Officer

Table of Contents

Objective

Testing shall be carried out to optimize the SurfLink® surface treatment process for MIS implants, so that the maximum SurfLink® surface coverage is attained for the roughness and material characteristics of the MIS implant.

Materials and Methods

Optimization of the SurfLink® surface treatment for MIS implants

The first round of optimization tested if there would be an advantage to using Deconex® 15PF to prepare the MIS implant surface prior to SurfLink® surface treatment. Deconex® 15PF is a commercially available phosphate free, potassium hydroxide based standard cleaning solution. In addition to potassium hydroxide it also contains a surfactant and a chelating agent. Deconex® has been used by NBMolecules® to clean and prepare implants used for all its in-vitro, pre-clinical, and clinical studies.

After this, optimization work was done to determine how much of the SurfLink® molecule is used up during the treatment of MIS implants. Minimum and maximum allowable concentrations and quantity of the SurfLink® solution were tested. The minimum concentration and volume conditions from the previous experiments were taken, and implants consecutively dipped one after each other in the SurfLink® solution to determine how many implants can be treated in a bath of SurfLink® before the SurfLink® molecules are used up and the bath has to be changed.

Finally the optimized protocol was carried out by a second operator to verify the process.

Summary of parameters tested

Process steps	Conditions/ variation tested
Deconex® pre-treatment	• XPS and SEM analysis of incoming implant • No pre-cleaning with Deconex®, followed by SurfLink® treatment using standard conditions (0.7mM, 25°C, sonication) • Pre-treatment with deconex at 60°C + sonication, followed by SurfLink® treatment using standard conditions
SurfLink® solution	• SurfLink® treatment at 25°C or 60°C with sonication • SurfLink® treatment with half required volume at standard concentration (0.7mM) • SurfLink® treatment with half required volume at concentrations 0.7, 2.0, 3.5, 5.0, 7.0 mM
Dipping exhaustion	• 10 consecutive implant treatments in the same SurfLink® solution, using the best conditions from the previous testing, using conditions with the lowest amount of SurfLink® molecules. • Test conditions: – Deconex® pre-treatment 60°C with sonication – SurfLink® solution, 60°C, 5mL, 0.7mM with sonication

All implants from the parameters tested were dried by vacuum and then analysed by XPS.

XPS analysis

In total 30 implants were received from MIS carrying the identification ref MF7-11375, Lot W15000784. Implants used in the optimization were sent for analysis by XPS. During initial testing one point of analysis was made (point B, as shown below). During verification testing 2 analysis points per implant were observed (point A,C, as shown below.

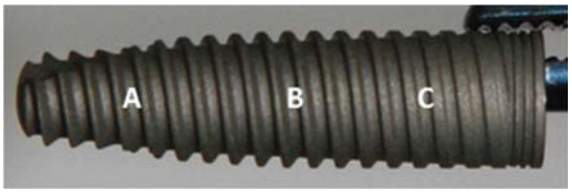

The following settings were used for the XPS measurements:

Instrument:	Kratos Axis Nova instrument (Kratos Analytical, Manchester, UK)
X-ray source:	Monochromatic Al $K\alpha_{1,2}$ irradiation (1486.7 eV), 225 W, angle of incidence 54.6°
Electron neutralizer:	On
Area of analysis:	700 µm x 700 µm
Analysis depth:	3-10 nm
Acquisition time:	30-91 sec (element dependant) high resolution spectra 10 min survey spectra
Analyser:	Hemispherical, perpendicular to the sample surface, 80 eV pass energy and 0.5 eV step size applying the constant analyser energy mode (fwhm of Ag3d5/2: 0.9eV)
Vacuum	$\leq 10^{-9}$ mbar
Angle	90° take-off
Calibration:	$Cu2p_{3/2}$ (932.6 eV), $Au4f_{7/2}$ (84.0 eV) and $Ag3d_{5/2}$ (368.2 eV) signals
Survey spectra:	0-1100 eV binding energy, all elements except H
Analysis:	CasaXPS version 2.3.14 (Gaussian/ Lorentzian (70%/ 30%) peak shape)
Relative Sensitivity Factors	Relative to the Kratos equipment

It should be considered that any elemental concentration below 0.3 atomic % is below the detection limit and such peaks are considered as noise.

Results and discussion

Deconex® pre-treatment

SEM imagery of the incoming implants showed a surface free from particle contamination.

The effects of pre-treating the implants with Deconex® before SurfLink® treatment were tested. Other than pre-treatment with Deconex®, the samples were treated with the same concentration of SurfLink®, however the Deconex® pre-treated implants were treated with SurfLink® solution at 60°C and at half the volume normally used (5mL, instead of 10mL equivalent per implant, as was used for the SurfLink® treatment, 06 Jan 2015 at MIS).

Following pre-treatment with Deconex® XPS survey spectra showed the expected elements ('Ti', 'Al', 'V', 'O', 'C', 'P') (see Table 1). The % atomic concentration of carbon was lower than had been observed for the implants that had not been pre-treated with

Deconex®. The % atomic concentration of phosphorus was also increased on the implants pre-treated with Deconex®. Phosphorus levels are an indication of the coverage of SurfLink® on the implant surface. In general the higher the % atomic concentration of phosphorus the more binding sites on the implant surface are occupied by the SurfLink® molecule.

The ratio of the % atomic concentration of phosphorus in relation to metal (titanium + aluminium + vanadium) is also elevated for the Deconex® pre-treated implants, as reported in Table 1. The 'SUM' of other elements is within acceptable limits for all lots tested.

Table 1 *– Summary of elemental composition from XPS Survey data (meaned data of 5 implants from each Lot for Lots C1 xxxxx, meaned data of 2 implants for MF7-11375).*

	Without Deconex® pre-treatment, implants treated 06Jan2015 at MIS			**With Deconex® pre-treatment**
Element	**C1 10330**	**C1 10375**	**C1 16420**	**MF7-11375**
Ti 2p	17.0	16.5	16.9	18.5
Al 2s	1.9	2.2	2.4	2.3
V 2p	0.3	0.3	0.5	0.4
O 1s	51.4	51.5	50.5	54.4
C 1s	24.7	24.7	23.7	19.5
P 2p	2.3	2.1	2.2	4.0
N 1s	0.8	0.9	0.9	0.6
S 2p	0.2	0.1	0.4	0
Ca 2p	0.3	0.4	0.5	0
Cl 2p	0.1	0.1	0.2	0
Na 1s	0.0	0.0	0.4	0
Si 2p	0.0	0.0	0.0	0.3
K 2p	0.0	0.0	0.3	0
Zn 2p	0.0	0.0	0.1	0
Cu 2p	0.0	0.0	0.0	0
Pb 4f	0.0	0.0	0.0	0
Ni 2p	0.0	0.0	0.0	0
Co 2p	0.0	0.0	0.0	0
Cr 2p	0.0	0.0	0.0	0
Fe 2p	0.0	0.0	0.0	0
Mo 3d	0.0	0.0	0.0	0
Mg 2p	1.0	1.0	1.0	0
F 1s	0.0	0.0	0.0	0
SUM*	2.4	2.6	3.8	0.9
P:Met**	**0.12**	**0.11**	**0.11**	**0.19**

*SUM = N1s, S2p, Ca2p, Cl2p, Na1s, Si2p, K2p, Zn2p, Cu2p, Pb4f, Ni2p, Co2p, Cr2p, Fe2p, Mo3d, Mg2p, F1s

**Met = [Ti2p + Al2s +V2p] % atomic concentration

SurfLink® solution – minimum/maximum concentration

Implants were first pre-treated with Deconex® at 60°C with sonication and then treated with varying concentrations of the SurfLink® solution at 60°C, with sonication, at a volume of 5mL per implant.

XPS survey spectra showed the expected elements ('Ti', 'Al', 'V', 'O', 'C', 'P') for all concentrations tested (see Table 2). The % atomic concentration of phosphorus and amount of phosphorus in relation to metal (titanium + aluminum + vanadium) remained constant at each concentration of SurfLink® solution tested. This indicates that in a solution of increased concentrations of the SurfLink® molecule, there is no increase in occupation of implant surface binding sites by SurfLink®, nor is it the case that SurfLink® forms bonds with itself on the implant surface to form multi SurfLink® layers instead of the desired monolayer.

Table 2 *– Summary of elemental composition from XPS Survey data for various concentrations used for the SurfLink® treatment of MIS implants MF7-11375 (meaned data of 2 implants for all concentrations).*

	SurfLink® concentration (mM)				
Element	**0.7**	**2.0**	**3.5**	**5.0**	**7.0**
Ti 2p	18.5	18.6	19.0	19.2	19.2
Al 2s	2.3	2.5	2.8	2.5	2.5
V 2p	0.4	0.5	0.5	0.5	0.5
O 1s	54.4	54.1	56.7	56.7	56.2
C 1s	19.5	19.9	16.7	16.2	16.6
P 2p	4.0	3.8	3.7	4.0	4.0
N 1s	0.6	0.7	0.7	0.6	0.7
S 2p	0	0.0	0.0	0.0	0.0
Ca 2p	0	0.0	0.0	0.0	0.0
Cl 2p	0	0.0	0.0	0.0	0.0
Na 1s	0	0.0	0.0	0.0	0.0
Si 2p	0.3	0.0	0.0	0.3	0.3
K 2p	0	0.0	0.0	0.0	0.0
Zn 2p	0	0.0	0.0	0.0	0.0
Cu 2p	0	0.0	0.0	0.0	0.0
Pb 4f	0	0.0	0.0	0.0	0.0
Ni 2p	0	0.0	0.0	0.0	0.0
Co 2p	0	0.0	0.0	0.0	0.0
Cr 2p	0	0.0	0.0	0.0	0.0
Fe 2p	0	0.0	0.0	0.0	0.0
Mo 3d	0	0.0	0.0	0.0	0.0
Mg 2p	0	0.0	0.0	0.0	0.0
F 1s	0	0.0	0.0	0.0	0.0
SUM*	0.9	0.7	0.7	0.9	1.0
P:Met**	**0.19**	**0.18**	**0.17**	**0.18**	**0.18**

*SUM = N1s, S2p, Ca2p, Cl2p, Na1s, Si2p, K2p, Zn2p, Cu2p, Pb4f, Ni2p, Co2p, Cr2p, Fe2p, Mo3d, Mg2p, F1s

**Met = [Ti2p + Al2s +V2p] % atomic concentration

Dipping exhaustion testing

Ten implants were first pre-treated with Deconex® at 60°C with sonication and then dipped consecutively in the same SurfLink® solution one after each other. The implants were dipped into a 0.7mM SurfLink® solution, at 60°C, with sonication, at a volume of 5mL.

XPS survey spectra showed the expected elements ('Ti', 'Al', 'V', 'O', 'C', 'P') for all implants treated, with the exception of the 9th and 10th implant to be dipped (see Table 3). The % atomic concentration of phosphorus and amount of phosphorus in relation to metal (titanium + aluminum + vanadium) remained constant for each implant until the 9th implant dipped in the series. This indicates that after treating the 8th implant there were insufficient SurfLink® molecules remaining in the SurfLink® treatment solution to engage all available binding sites for the implant surface of the 9th and particularly the 10th implant. It is also worth noting that there was no increase of contamination on the implant surface following the consecutive dipping of implants in the same SurfLink® solution.

Final protocol verification

The final optimized protocol was carried out by a second operator to verify the process. Three implants were first pre-treated with Deconex® at 60°C with sonication and then dipped consecutively in the same SurfLink® one after each other. Implants were dipped into a 0.7mM SurfLink® solution at 60°C with sonication, at a volume of 5mL per implant.

XPS survey spectra of the implants treated by the 2nd operator (31Mar2015) showed the expected elements ('Ti', 'Al', 'V', 'O', 'C', 'P') at levels similar to those observed in previous tests (operator 1 – 18Mar2015) (see Table 4). The % atomic concentration of phosphorus and amount of phosphorus in relation to metal (titanium + aluminum + vanadium) was also comparable to previous results (see Table 4). This confirms previous results and shows good method robustness between operators.

Table 3 *– Summary of elemental composition from XPS Survey data for implants consecutively dipped in the same SurfLink® treatment solution until exhaustion (data from 1 analysis point on 1 implant for each consecutive dipping).*

	Consecutive dipping									
Element	**1**	**2**	**3**	**4**	**5**	**6**	**7**	**8**	**9**	**10**
Ti 2p	18.3	18.3	18.5	17.8	18.4	18.1	17.8	17.7	19.1	18.3
Al 2s	3.5	2.7	2.3	2.4	2.3	3.6	2.8	1.8	2.0	3.1
V 2p	0.5	0.3	0.3	0.4	0.3	0.1	0.4	0.4	0.3	0.5
O 1s	54.4	54.3	54.7	54.5	55.8	54.5	54.8	55.3	55.4	55.6
C 1s	18.2	19.8	18.9	19.9	18.2	18.7	18.5	19.3	18.0	18.0
P 2p	3.8	3.5	3.8	3.4	3.6	3.7	3.9	3.7	3.5	3.3
N 1s	0.9	0.6	0.8	1.0	0.7	0.9	1.0	1.0	0.8	0.6
S 2p	0.0	0.0	0.0	0.0	0.0	0.0	0.0	0.0	0.0	0.0
Ca 2p	0.1	0.2	0.0	0.0	0.0	0.0	0.0	0.0	0.0	0.0
Cl 2p	0.0	0.0	0.0	0.0	0.0	0.0	0.0	0.0	0.0	0.0
Na 1s	0.0	0.0	0.0	0.0	0.0	0.0	0.0	0.0	0.0	0.0
Si 2p	0.4	0.4	0.7	0.6	0.7	0.6	0.8	0.8	0.8	0.7
K 2p	0.0	0.0	0.0	0.0	0.0	0.0	0.0	0.0	0.0	0.0
Zn 2p	0.0	0.0	0.0	0.0	0.0	0.0	0.0	0.0	0.0	0.0
Cu 2p	0.0	0.0	0.0	0.0	0.0	0.0	0.0	0.0	0.0	0.0
Pb 4f	0.0	0.0	0.0	0.0	0.0	0.0	0.0	0.0	0.0	0.0
Ni 2p	0.0	0.0	0.0	0.0	0.0	0.0	0.0	0.0	0.0	0.0
Co 2p	0.0	0.0	0.0	0.0	0.0	0.0	0.0	0.0	0.1	0.0
Cr 2p	0.0	0.0	0.0	0.0	0.0	0.0	0.0	0.0	0.0	0.0
Fe 2p	0.0	0.0	0.0	0.0	0.0	0.0	0.0	0.0	0.0	0.0
Mo 3d	0.0	0.0	0.0	0.0	0.0	0.0	0.0	0.0	0.0	0.0
Mg 2p	0.0	0.0	0.0	0.0	0.0	0.0	0.0	0.0	0.0	0.0
F 1s	0.0	0.0	0.0	0.0	0.0	0.0	0.0	0.0	0.0	0.0
SUM*	1.4	1.3	1.5	1.6	1.5	1.5	1.8	1.8	1.7	1.2
P:Met**	**0.17**	**0.16**	**0.18**	**0.17**	**0.17**	**0.17**	**0.19**	**0.18**	**0.16**	**0.15**

*SUM = N1s, S2p, Ca2p, Cl2p, Na1s, Si2p, K2p, Zn2p, Cu2p, Pb4f, Ni2p, Co2p, Cr2p, Fe2p, Mo3d, Mg2p, F1s

**Met = [Ti2p + Al2s +V2p] % atomic concentration

Table 4 *– Summary of elemental composition from XPS Survey data of the SurfLink® treatment of MIS implants MF7-11375 by different NBM operators (meaned data of 2 implants for operator 1, and of 2 analysis points per implant for operator 2).*

	Operator 1 18 Mar 2015	**Operator 2 31 Mar 2015**		
Element	**1**	**1**	**2**	**3**
Ti 2p	18.5	18.3	18.4	18.9
Al 2s	2.3	1.9	2.5	2.0
V 2p	0.4	0.4	0.4	0.4
O 1s	54.4	55.1	55.5	55.6
C 1s	19.5	19.2	17.9	17.6
P 2p	4.0	4.0	3.8	4.1
N 1s	0.6	0.6	0.8	0.8
S 2p	0	0.0	0.0	0.0
Ca 2p	0	0.2	0.3	0.2
Cl 2p	0	0.0	0.0	0.0
Na 1s	0	0.0	0.0	0.0
Si 2p	0.3	0.3	0.4	0.5
K 2p	0	0.0	0.0	0.0
Zn 2p	0	0.0	0.0	0.0
Cu 2p	0	0.0	0.0	0.0
Pb 4f	0	0.0	0.0	0.0
Ni 2p	0	0.0	0.0	0.0
Co 2p	0	0.0	0.0	0.0
Cr 2p	0	0.0	0.0	0.0
Fe 2p	0	0.0	0.0	0.0
Mo 3d	0	0.0	0.0	0.0
Mg 2p	0	0.0	0.0	0.0
F 1s	0	0.0	0.0	0.0
SUM*	0.9	1.1	1.4	1.5
P:Met**	**0.19**	**0.19**	**0.18**	**0.19**

*SUM = N1s, S2p, Ca2p, Cl2p, Na1s, Si2p, K2p, Zn2p, Cu2p, Pb4f, Ni2p, Co2p, Cr2p, Fe2p, Mo3d, Mg2p, F1s

**Met = [Ti2p + Al2s +V2p] % atomic concentration

Conclusion

Pre-treating MIS implants with a Deconex® solution at 60°C, followed by SurfLink® Surface Treatment with SurfLink® solution at 60°C, showed increased coverage of the implant surface with the SurfLink® molecule.

Other testing showed that the SurfLink® solution concentration can be varied from 0.7-7.0mM, without affecting the application of the SurfLink® molecule onto the implant surface. Furthermore, the dipping exhaustion experiments show that the same SurfLink® solution can be used for the treatment of multiple implants. This will allow a large degree of flexibility during manufacturing, and permit multiply racks of implants to be treated with the same bath of SurfLink® solution, reducing downtime incurred through the replenishment of SurfLink® treatment baths.

This optimized protocol for the treatment of MIS implants with SurfLink® should be validated on implants produced and SurfLink® treated in MIS manufacturing facilities.

Appendix 1 - Example of survey spectrum from protocol verification experiment

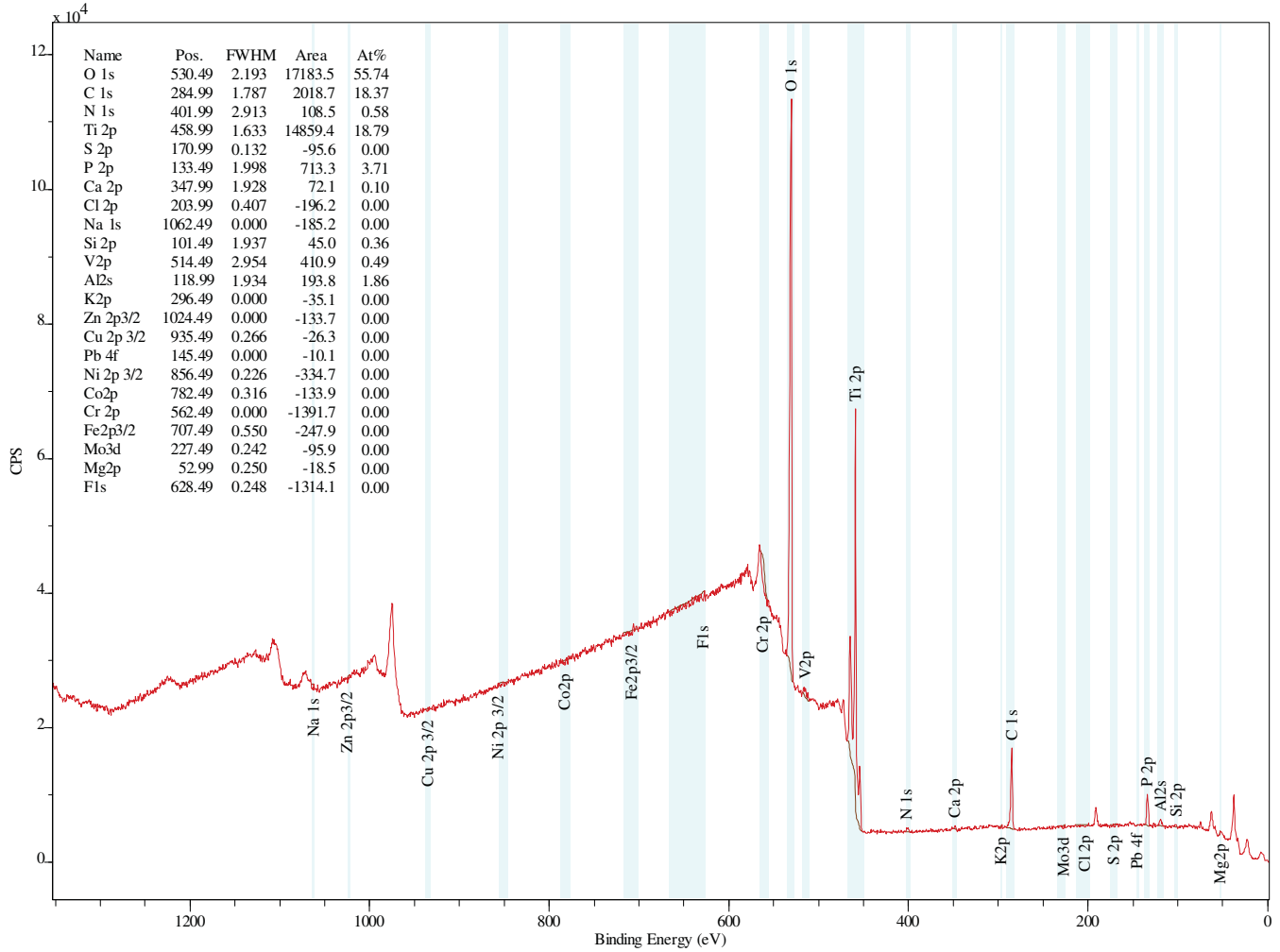

Appendix 2 - Example of survey spectrum from protocol verification experiment – Zoom of area of interest 0 – 300eV

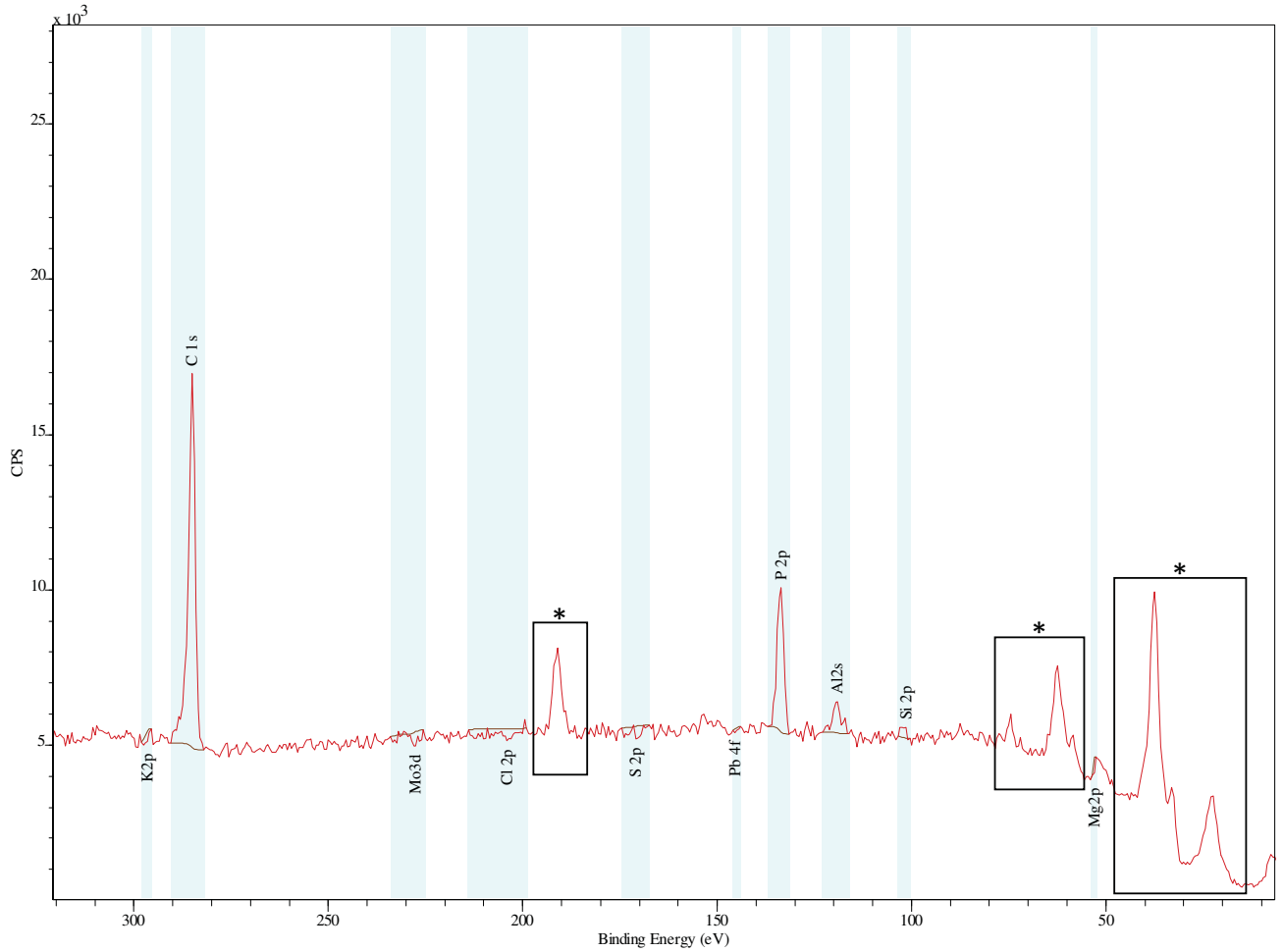

*Non assigned peaks are secondary peaks of element already accounted for by their main peak.